SIMULATED RADIANCE FOR MIE ABSORBING FINITE CLOUDS

By

John T. Klehr
Thomas B. McKee

Atmospheric Science
PAPER NO.
285

ATM 76-80568

DEPARTMENT OF ATMOSPHERIC SCIENCE
COLORADO STATE UNIVERSITY
FORT COLLINS, COLORADO

SIMULATED RADIANCE PATTERNS FOR MIE ABSORBING FINITE CLOUD

By

John T. Klehr
Thomas B. McKee

The research reported here has been supported
by the Global Atmospheric Research Program,
National Science Foundation, and the
GATE Project Office, National Oceanic and
Atmospheric Administration under Grant No. ATM76-80568.

Department of Atmospheric Science
Colorado State University
Fort Collins, Colorado

March 1978

Atmospheric Science Paper No. 285

ABSTRACT

Calculations were made of the scattering of sunlight from finite and infinite clouds composed of particles which were capable of both scattering and absorption. Results of Mie absorption upon shortwave irradiance values and radiance patterns of finite (cubic) and infinite (layer) clouds are presented over a range of single scattering albedoes ($\bar{\omega}_0$) from 1.0 to 0.9 and solar zenith angles of 0°, 30°, and 60°. A finite cloud is shown to absorb a smaller fraction of incident light than an infinite cloud at all sun angles and values of single scattering albedo. Both cloud types show a maximum fraction of absorption with the sun vertical. In an infinite cloud as the solar zenith angle is increased the absorption decreases in the lower layers of the cloud, while in the finite cloud the lower layers increase in absorption as the solar zenith angle is increase.

Radiance patterns are shown to be primarily determined by cloud and solar geometries with absorption tending to reduce the radiance values and only slightly flatten the radiance patterns. If the optical depth is increased from 20 to 60 with the sun vertical the finite cloud shows a larger increase in fractional absorption than the infinite, but even at large optical depths (60) and large absorption values ($\bar{\omega}_0 = 0.9$) the finite cloud still allows a significant fraction of light to escape downward from its sides.

ACKNOWLEDGEMENTS

The authors wish to thank Dr. Stephen K. Cox and Dr. Lawrence N. Hadley for their aid and guidance.

This research has been supported by the Global Atmospheric Research Program, National Science Foundation, and the GATE Project Office, National Oceanic and Atmospheric Administration under Grant No. ATM 76-80568. Computer time was provided by the National Center for Atmospheric Research which is supported by the National Science Foundation.

TABLE OF CONTENTS

LIST OF TABLES

LIST OF FIGURES

LIST OF FIGURES Continued

LIST OF FIGURES Continued

LIST OF SYMBOLS

g	asymmetry factor
N	photon encounter number
n	droplet number density
$P(\alpha)$	probability density function
$PP(\alpha)$	cumulative probability function
PR	probability
r	droplet radius
RN	random number
s	distance
X	x axis
x	cloud face perpendicular to x axis
xc	half width of cloud
Y	y axis
y	cloud face perpendicular to y axis
yc	half width of cloud
Z	z axis
α	scattering angle
β	volume scattering coefficient
γ	second scattering angle
θ	zenith angle
θ_o	solar zenith angle
λ	wave length
μ	cosine of scattering angle
τ	optical thickness

ϕ	azimuth angle
ω	solid angle
$\bar{\omega}_o$	single scattering albedo

I. Introduction

A. Previous Work in the Literature

Finite clouds play an important but inconspicuous role in the radiative and thermodynamic budgets of the atmosphere. With improved resolution in satellite imagery their numbers are becoming apparent and their radiative effects must now be considered more closely. McKee and Cox (1974, 1976) and Busygin et al. (1973) have shown finite clouds to be quite different from infinite horizontally homogeneous clouds in both irradiance and radiance for conservative scattering. Danielson et al. (1969) have studied the absorption of visible light vertically incident upon a semi-infinite horizontal cloud. Twomey (1972, 1976) has used a matrix method to calculate absorption in infinite cloud layers over a range of wavelengths.

The purpose of this contribution is to outline the methods and results of Mie absorption upon shortwave radiance patterns of finite clouds in contrast to those of infinite clouds for a range of absorption and for a range of solar zenith angles.

B. Monte Carlo computation

Cashwell and Everett (1959) have described the Monte Carlo method in detail. Kattawar and Plass (1971) and Danielson et al. (1969), among others, have used the Monte Carlo method in semi-infinite cloud layer scattering computations. Busygin et al. (1973) and McKee and Cox (1974, 1976) have used the Monte Carlo method for finite-shaped clouds with conservative scattering. The following description is based upon McKee and Cox (1974, 1976).

The Monte Carlo technique is uniquely suited for the direct simulation of the transfer of radiation in a 3 dimensionally bounded medium. The method, in essence, directly simulates the physical radiative processes within the cloud. A set of boundaries is defined for the limits of these processes. Photons are introduced into the cloud travelling in a specified direction. The distance to an interaction location is determined and the type of interaction, scattering or absorption, is determined. If scattering is selected, a new direction of travel is selected from the phase function. These steps are repeated until the photon is absorbed or escapes through a boundary.

Random noise in Monte Carlo calculations decreases with the increasing numbers of photons processed. When large optical depths are used, computer time increases proportionately and may become prohibitive in cost. A method of photon weighting has been devised in which photons are assigned a weight which can be allowed to escape in fractions of the actual photon energy. Photons are then forced to have collisions until their entire energy has escaped. The same answer is obtained as though direct simulation had been pursued.

In the non-weighting mode the simulated photons scatter until escape, absorption, or maximum number of allowed encounters is reached. Photons retain their initial weight of one unit until they are terminated. In the weighting (forced collision) mode photons begin with a unit weight but at each scattering encounter the weight is decreased by a fraction proportional to the amount of energy that would be transmitted to the boundary of the cloud in the original direction before the scatter. This fraction traverses the cloud and is counted as it exits the cloud. The remaining fraction of weight is allowed to

scatter in a new direction and forced to have another encounter. Hence, in the weighting mode, the only light exiting the cloud is composed of those fractions allowed to escape before each scatter. This fraction which escapes varies in an inverse manner with the distance from the scattering encounter to the boundary in the original direction of travel. In the weighting mode, the photon weight decreases with each encounter and the photon is terminated when a minimum allowed weight is reached.

Photons travelling horizontally are dropped if the distance to the next collision is greater than a preset distance, corresponding to a preset probability. This horizontal-termination mechanism functions in both the weighting and non-weighting modes.

One of the unique features of the Monte Carlo method is its ability to conserve energy. Every photon and every photon weight may be accounted for either by escape, absorption, or by being terminated for exceeding allowed limits. In most cases the amount of weight due to termination is less than 1%. In each Monte Carlo computer run 20,000 simulated photons are usually entered into the cloud, in groups of 2,000. Statistical analyses based upon these 10 groups gives some indication of the amount of random noise in any single run of 20,000 photons. The weighting mode produces about a 1/3 smaller maximum standard deviation than a non-weighting run (Table 1). However the weighting mode runs about twice as long as the non-weighting mode.

The present simulation is for an isolated cloud with no surrounding atmosphere and a ground surface with an albedo of zero. The volume scattering coefficient and phase function have been obtained from Deirmendjian (1969) for a water cloud C.1 and a wavelength of

Table 1. Intercomparison of Monte Carlo modes for $\bar{\omega}_0 = 1.0$ and $\bar{\omega}_0 = 0.99$ for a $\tau = 20$, $\theta_0 = 0$ infinite cloud.

Mode	$\bar{\omega}_0$	Directional Reflectance	% Absorbed	Maximum Standard Deviation	CDC 7600 CPU
Weighting	1.0	.63221	0	.09	263 s
No weighting	1.0	.63360	0	.29	135 s
No weighting selective	.99	.45383	32.6	.30	102 s
Weighting selective	.99	.45331	32.1	.12	187 s
Weighting partitive	.99	.45173	32.7	.09	251 s
No weighting partitive	.99	.45279	32.4	.23	138 s

0.70 μm. The cloud was composed of water droplets with a size distribution given by

$$n = 2.373\ r^6 \exp(-1.5r) ,$$

which is a model for a cumulus cloud where n represents the number of droplets cm^{-3} for a given radius r (figure 1). This results in a volume scattering coefficient of 16.73 km^{-1} and a liquid content of 0.063 g m^{-3} for 100 particles per cubic centimeter. Geometric depth and optical depth are related linearly by the liquid water content (figure 2). A 1.5 km deep cloud with a $\tau = 20$, has a liquid water content of 0.05 g m^{-3}.

The distance travelled between collisions is directly simulated. The fraction of radiation transmitted through a given distance is also the probability of a photon travelling the same distance, i.e.

$$PR = e^{-\tau} = \exp(-\int_0^s \beta ds) , \qquad (1)$$

relates the probability PR to the optical depth τ, with the volume scattering coefficient β, and distance s. The method of simulation is to choose a random number RN for PR and to calculate the optical depth to a collision by determining the upper limit of integration of

$$\int_0^s \beta ds = \tau = - \ln(1 - RN) . \qquad (2)$$

The single-scattering phase function $P(\alpha)$ defines the angular distribution of the radiation following a scattering event. The scattering angle α is measured from the direction of propagation before the collision to the direction after the collision. The phase function used (Deirmendjian (1969), C1, $\lambda = 0.70$ μm) is characterized

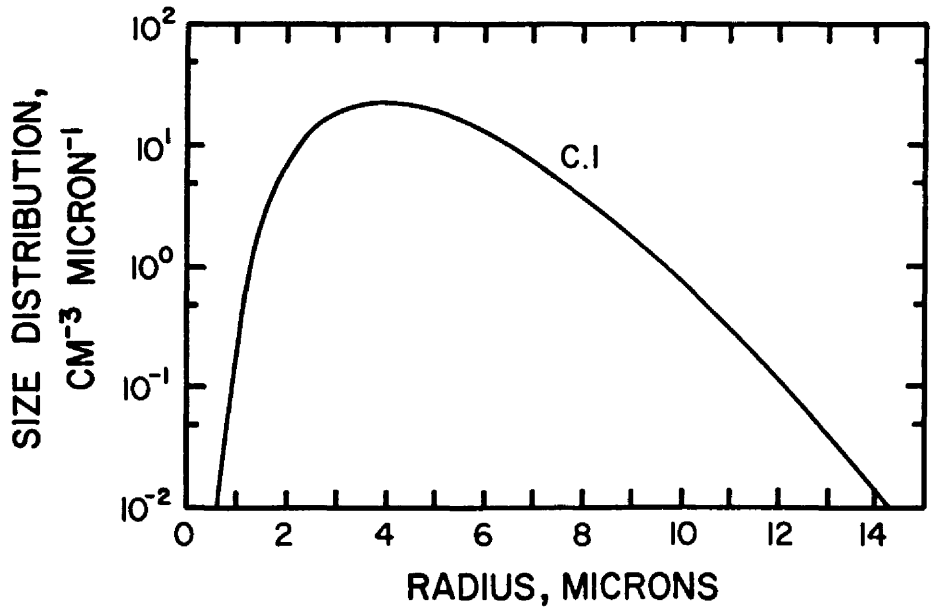

Figure 1. Droplet size distribution for C.1. model (after Deirmendjian, 1969).

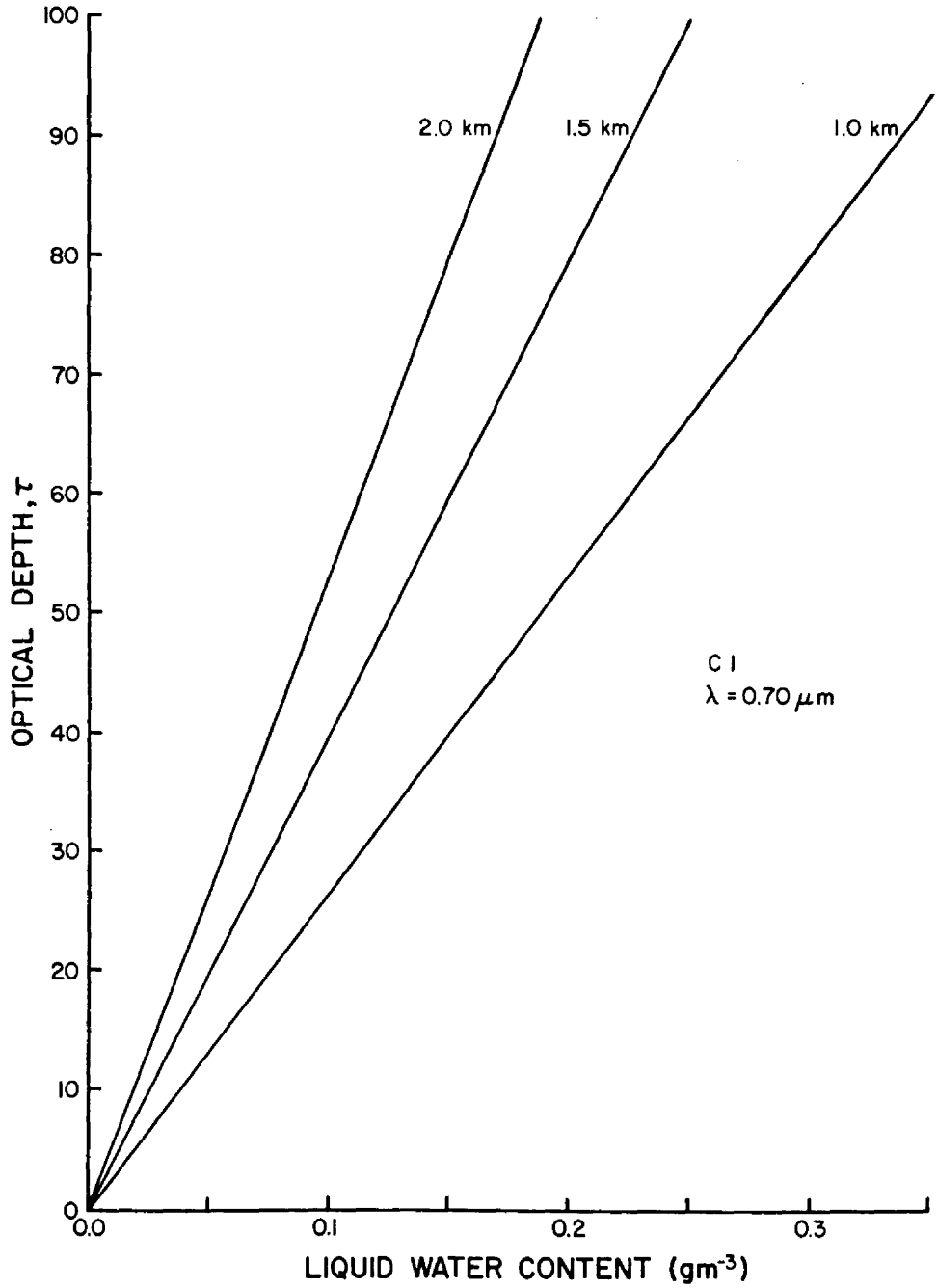

Figure 2. Liquid water content versus optical depth for C.1. model at λ = 0.70 μm.

by a very strong forward scattering peak (figure 3). The normalized phase function, integrated over solid angle, ω ,

$$\int p(\alpha)d\omega = 1 ,$$

is independent of the second angle needed to define the direction of propagation after a collision. The second angle γ is a rotation about the direction of propagation prior to the collision. The angle γ is picked randomly between 0 and 2π.

The probability of a photon being scattered between 0 and α is given by

$$PP(\alpha) = 2\pi \int_0^{\alpha} P(\alpha)d(\cos\alpha) . \qquad (3)$$

A random number is chosen for $PP(\alpha)$ and Eq. (3) is solved for the upper limit of integration, yielding the scattering angle α. The probability of scattering between 0 and α is shown in figure 4. Fifty percent of the radiation is contained within the first 10° of the forward direction.

Two different cloud geometries are used in the computations, a cubic cloud and a semi infinite slab cloud. Figure 5 shows a sketch of a cubic cloud with the coordinate system used. Incident sunlight is always in the (Y,Z) plane which restricts direct sunlight to the top and +y face of the cube. The incident solar beam is assumed to be a plane parallel beam, and photons are randomly entered along the top surface and side surface in proportion to the incident solar angle. The cube is 1.5 km along an edge. The semi-infinite slab is 500 km by 500 km by 1.5 km deep.

The two angles used to specify exiting radiation are the zenith angle θ measured from the Z axis and an azimuth angle ϕ measured

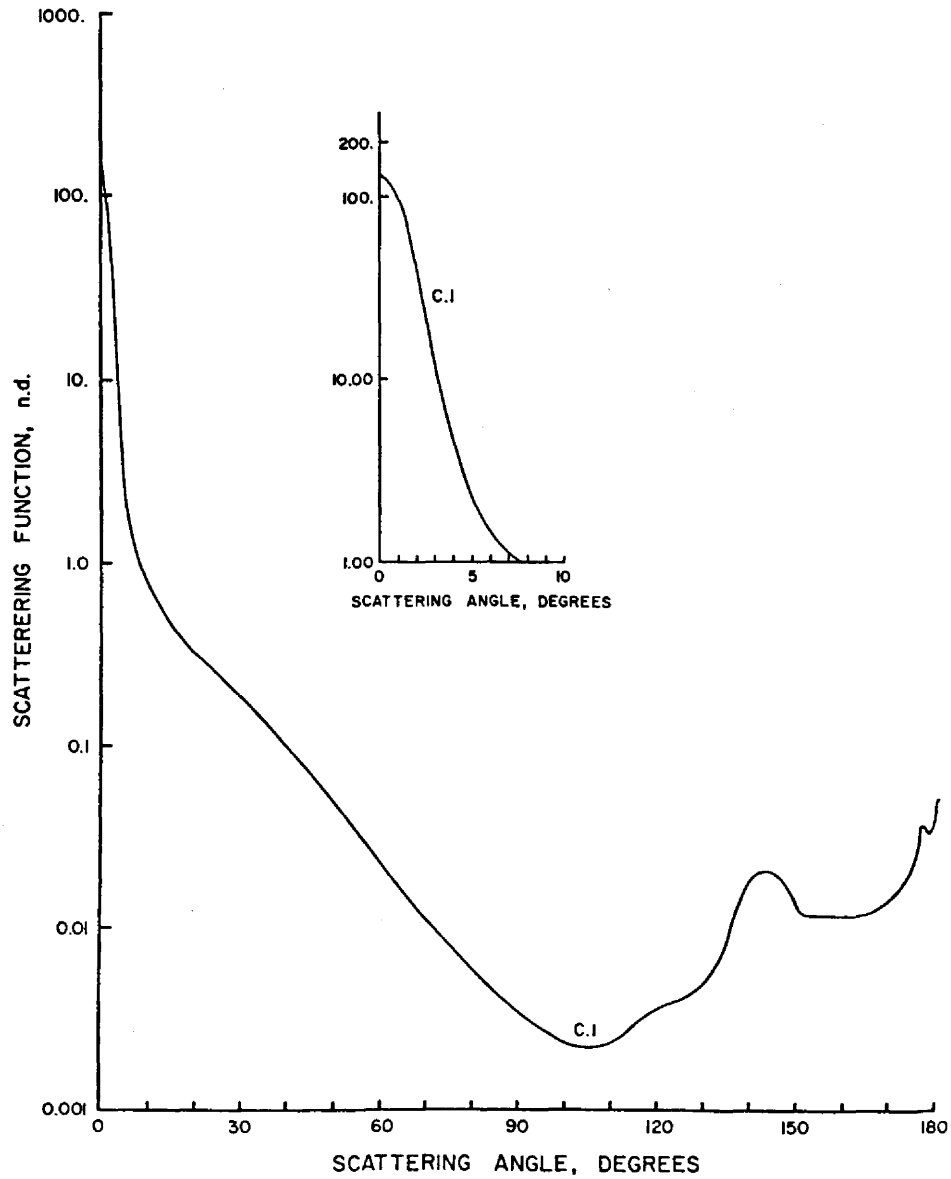

Figure 3. Scattering phase function for C.1. cloud model at $\lambda = 0.7$ μm.

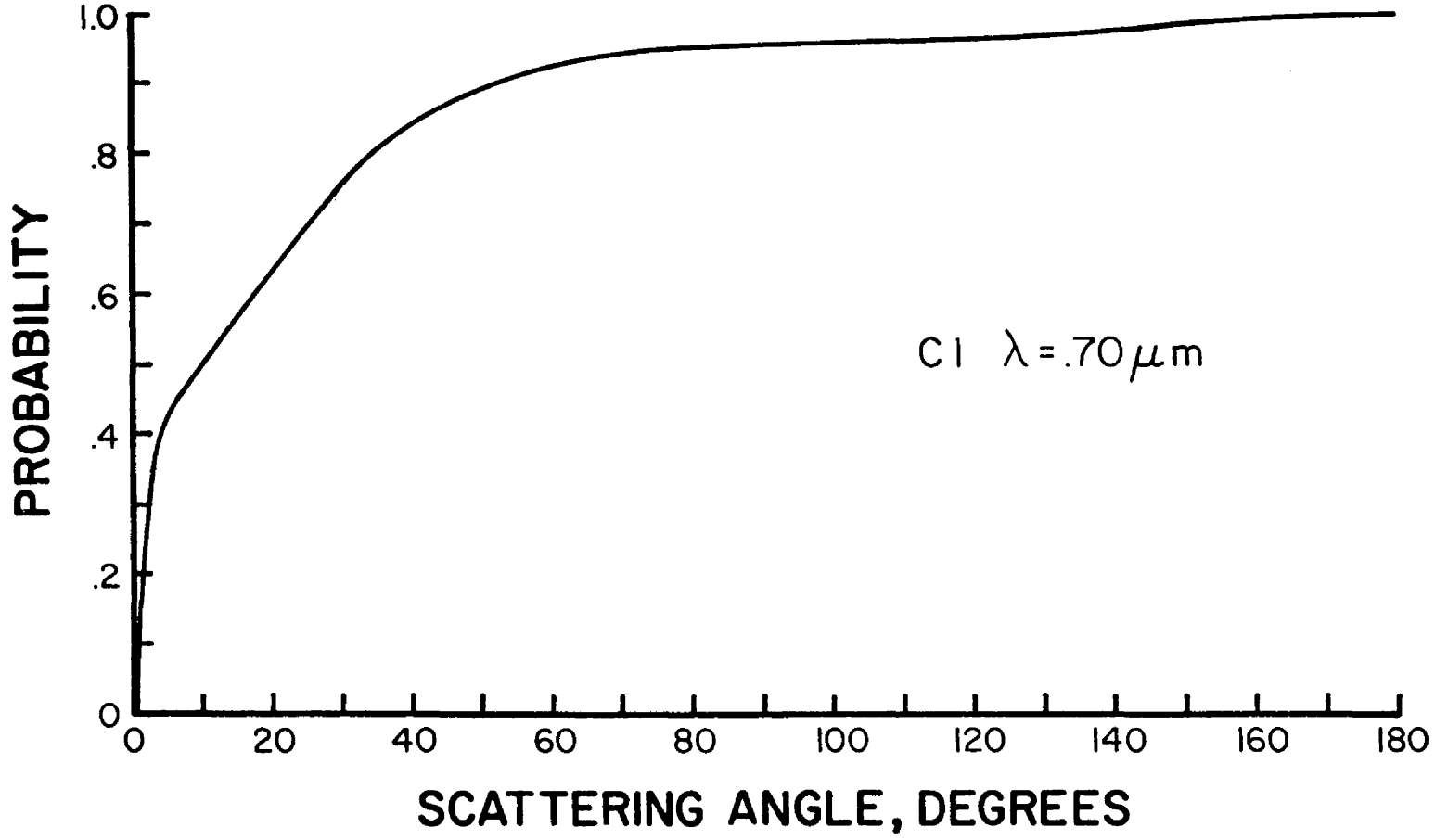

Figure 4. Cumulative probability density function for C.1. model at λ = 0.7μm.

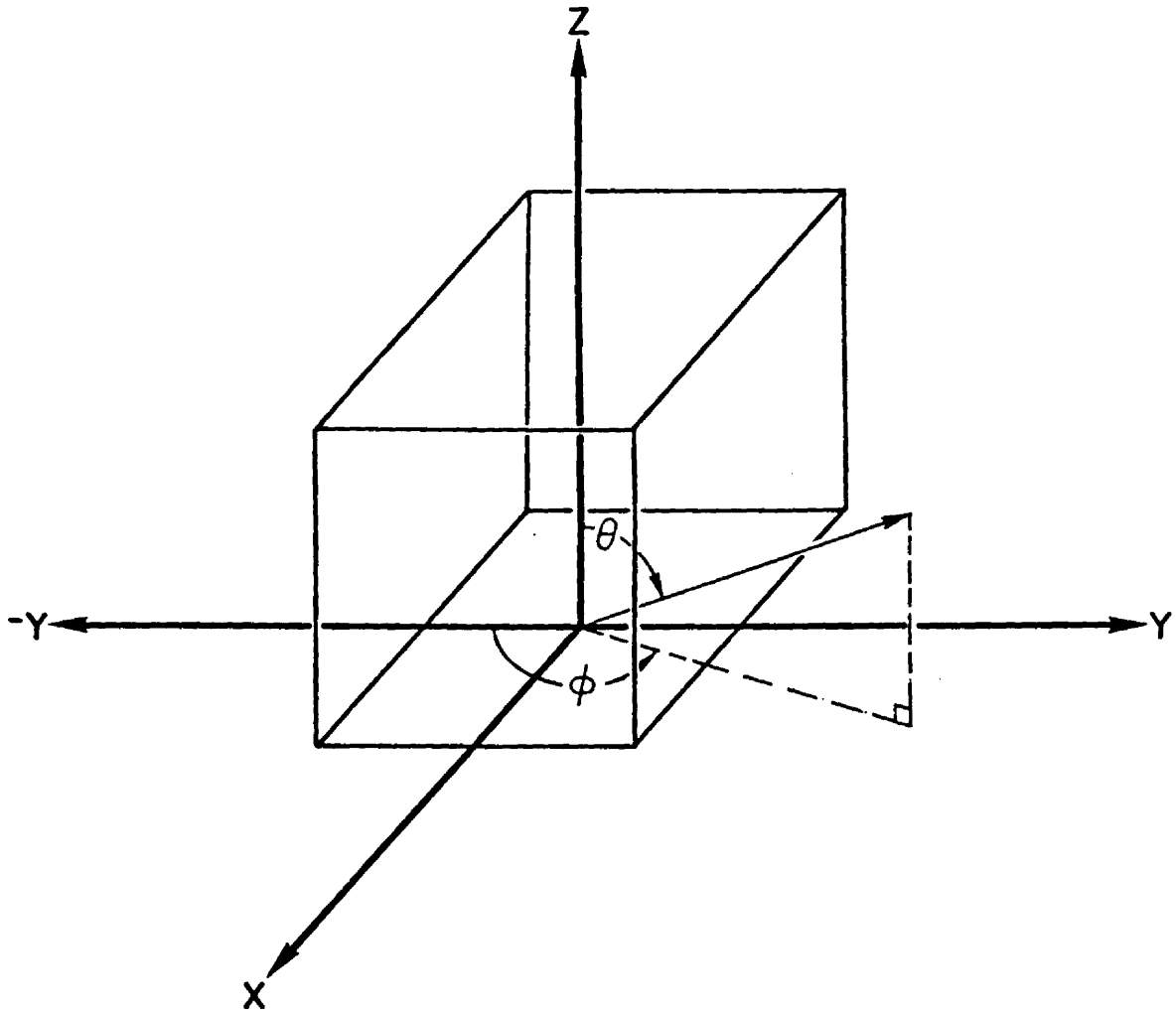

Figure 5. Cubic cloud with coordinate system.

from the -Y axis. A ϕ value of zero is opposite from the sun and a ϕ value of π is towards the sun. Subsequent graphs will show relative radiance values averaged over a finite solid angle $\Delta\omega$, where

$$\Delta\omega = \Delta \cos\theta \, \Delta\phi ,$$

for $\Delta \cos\theta = 0.1$ and $\Delta\phi = 15°$. All radiances are relative to a solar irradiance of π. A relative radiance of unity in all directions would be radiated by a perfectly diffuse reflecting surface so illuminated.

Two examples of equal solid angle are shown in figure 6. The solid angle shown near the zenith has a much larger span of zenith angle than the solid angle shown near the horizontal. The radiances to be presented represent averaging over a complete face of the cloud and over a finite solid angle, to allow direct addition of radiances from the top and sides.

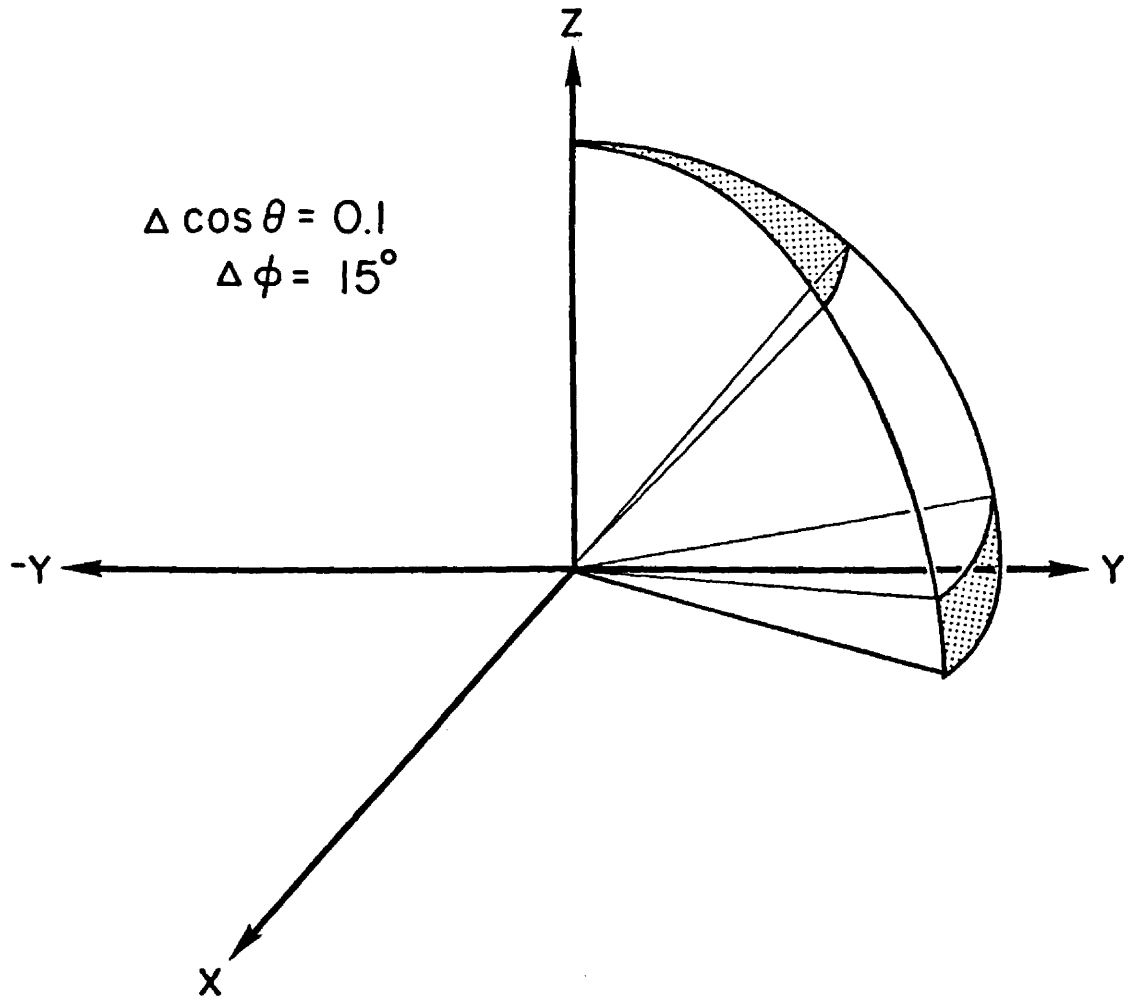

Figure 6. Example of equal solid angles.

II. Method

A. Absorptive modes in Monte Carlo computations

Mie absorption may be directly simulated using the single scattering albedo $\bar{\omega}_0$, which is the fraction of the incoming energy that is scattered at each encounter. Hence the probability of an absorption event is $1 - \bar{\omega}_0$. In the selection mode a random number between 0 and 1.0 is called and compared to $1 - \bar{\omega}_0$ to determine if scattering or absorption occurs. In the partitive mode a constant fraction equal to $1 - \bar{\omega}_0$ times the existing weight of the photon is absorbed at the position of the encounter and the remaining weight is allowed to scatter. The partitive mode decreases the weight of each photon by a constant fraction at each encounter. The selective mode does not decrease the weight at each encounter, the entire weight is either absorbed or scattered.

Figure 7 illustrates the effects of the two modes upon the mean weight of all the photons at each encounter. The selective and partitive modes for $\bar{\omega}_0 = 0.9$ ($\theta_0 = 0^0$, $\tau = 20$) are shown with the conservative case ($\bar{\omega}_0 = 1.0$) shown for reference. The effect of the forced collision-weighting mode is shown by the conservative case. The selective mode is identical to the conservative case until the random selection of absorptive events is a large fraction of the photons existing at an encounter. At that point the selective mode begins to wander randomly about the pure weighting case ($\bar{\omega}_0 = 1.0$). The partitive mode reduces the mean weight more rapidly than the selective mode. The mean weight is reduced until the minimum weight allowed (.01) is reached. The entire photon is killed and its remaining weight is counted. The

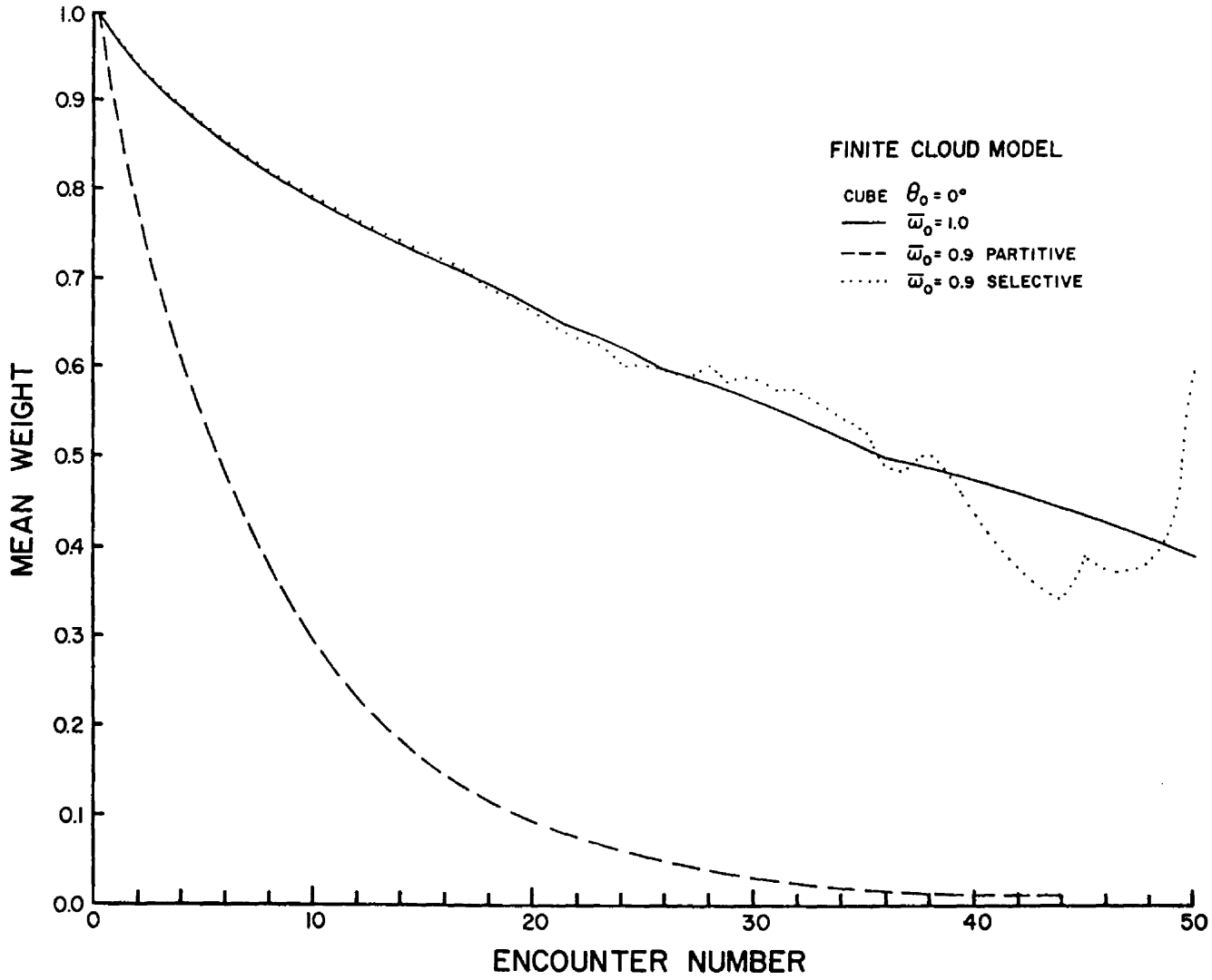

Figure 7. Mean weight of photons versus encounter number.

partitive mode will reduce the weight in an exponential manner so that the encounter at which the minimum weight is reached may be estimated by:

$$.01 > (\bar{\omega}_0)^N \qquad \text{where N is the encounter number}$$

$$\text{or for } \bar{\omega}_0 = 0.9 \qquad N \tilde{=} 44 \ .$$

Figure 8 shows the number of photons existing at each encounter number for the conservative case and for $\bar{\omega}_0 = 0.9$ for the selective and partitive modes.

Figures 9 and 10 show the relative radiance from all ϕ boxes versus cosine θ for the infinite cloud model and the finite cloud model respectively. The infinite cloud model was modified to function with or without weighting in either the selective or partitive mode. Figure 9 shows the infinite cloud model for $\tau = 20$, $\theta_0 = 0°$, $\bar{\omega}_0 = 1.0$, for the weighting and non-weighting modes, and at $\bar{\omega}_0 = .99$ for the selective and partitive modes in both the weighting and non-weighting modes. Few photons exit at small values of cosine theta resulting in a higher random noise problem. Figure 9 illustrates that that weighting and non-weighting modes are quite similar as are the 4 modes of absorption.

The finite cloud model was modified to function in the weighting mode with either the selective or partitive mode in use. Figure 10 shows results from the finite cloud model for $\tau = 20$, $\theta_0 = 0°$, $\bar{\omega}_0 = 0.99$ for the selective and partitive modes. The results are identical within the noise level of the Monte Carlo methods.

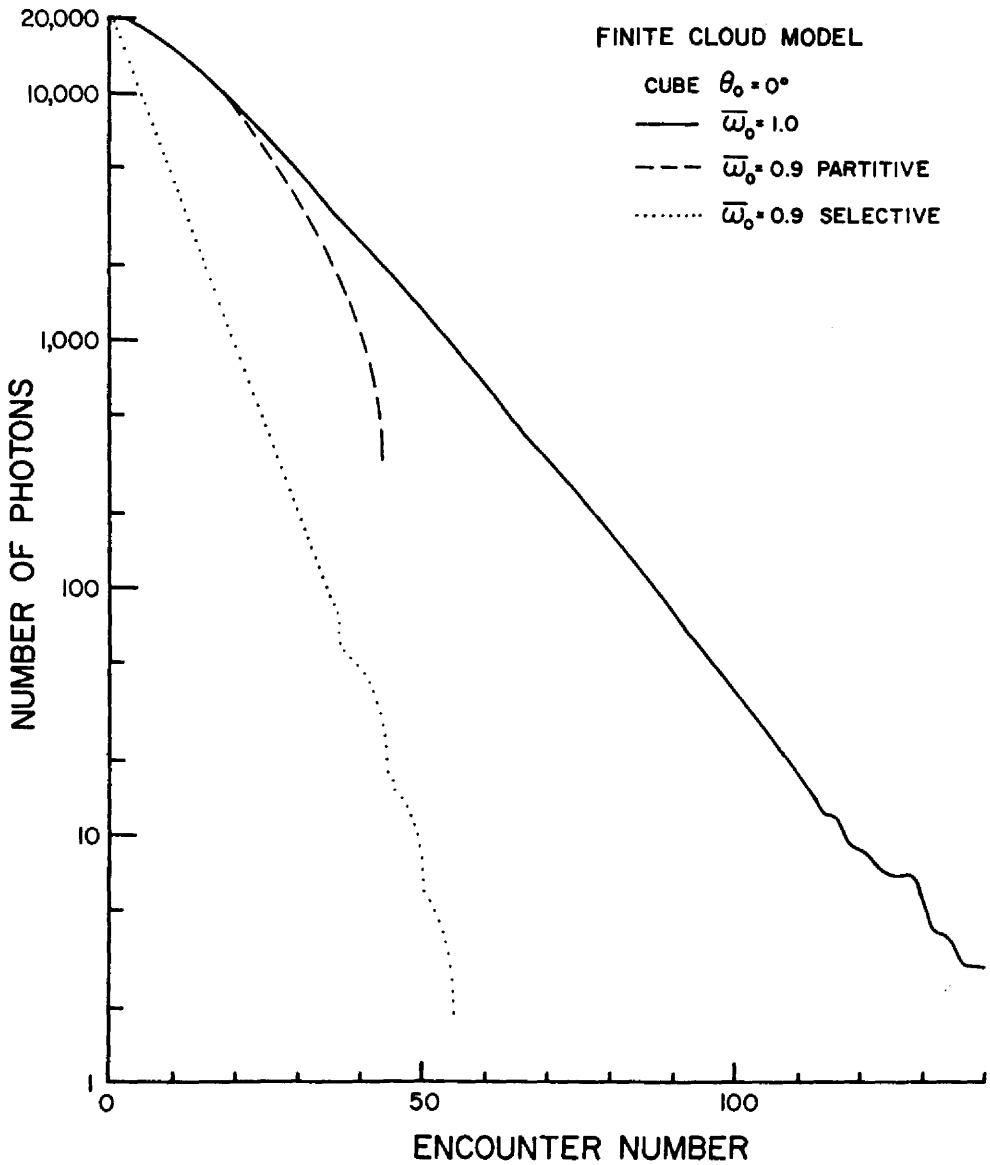

Figure 8. Number of photons versus encounter number.

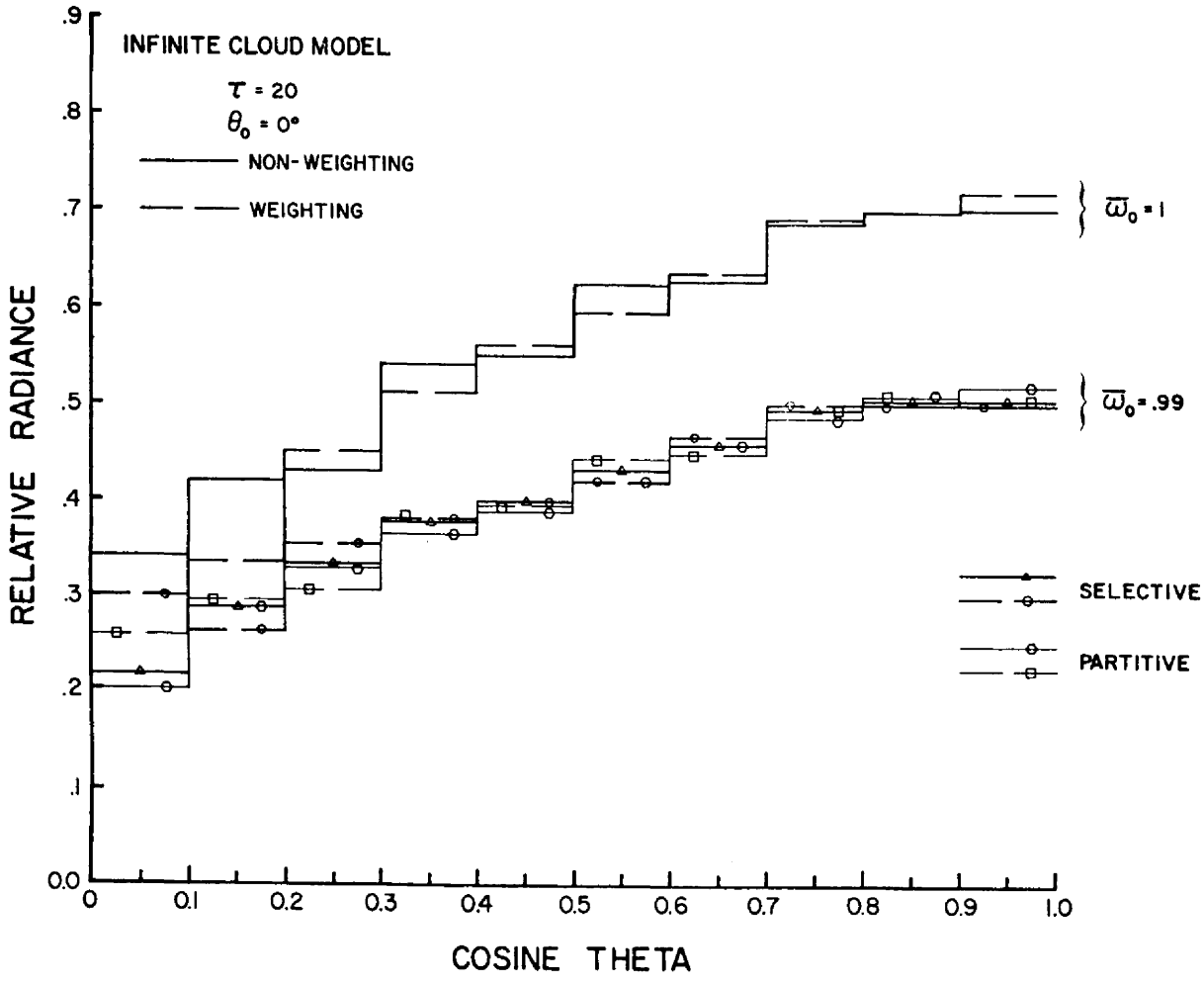

Figure 9. Relative radiance versus cosine θ for the various modes in an infinite cloud model.

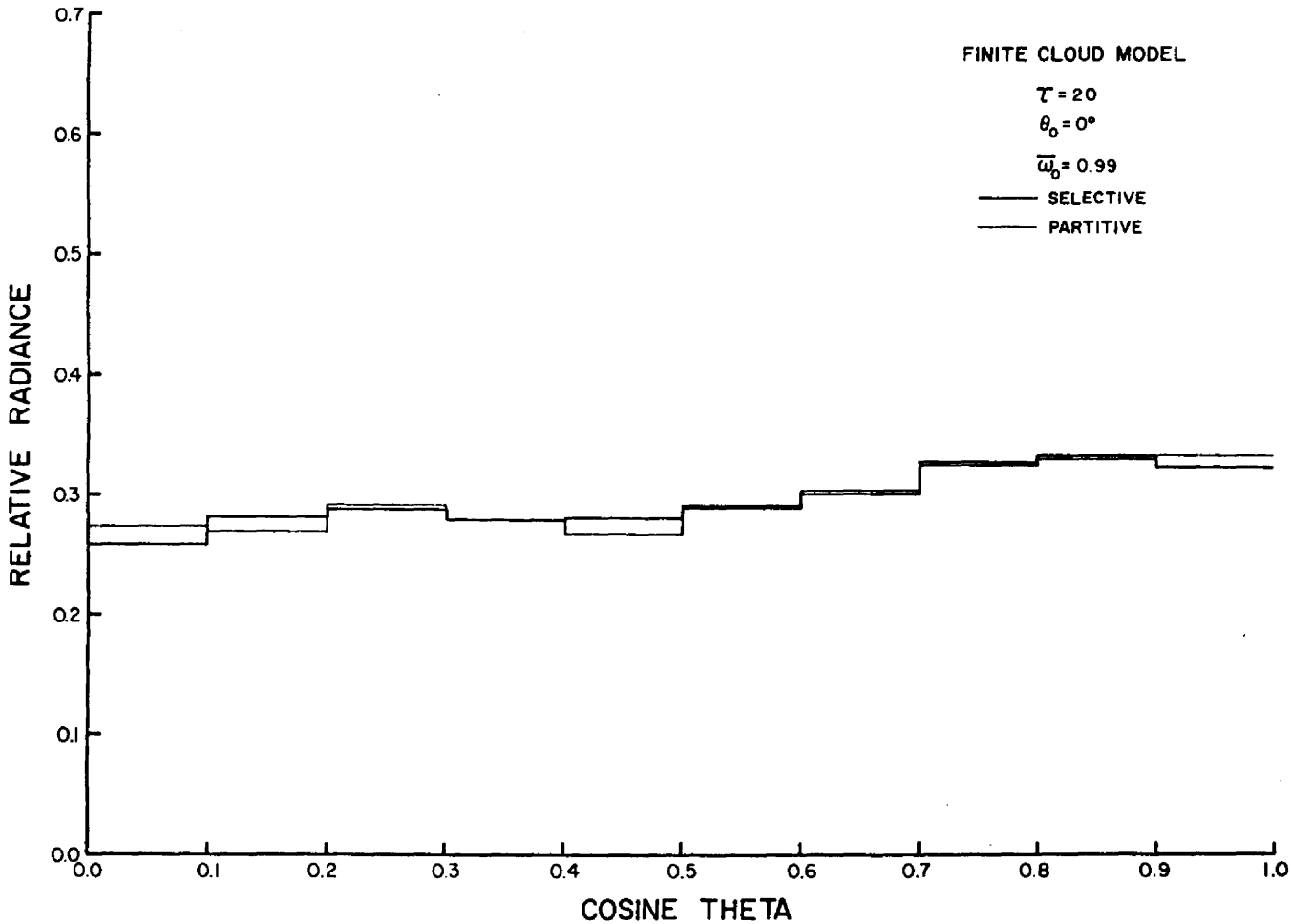

Figure 10. Relative radiance versus cosine θ for the finite cloud model in the selective and partitive modes.

B. Verification of Monte Carlo absorption modes

1. I.U.G.G.

Comparisons of the absorptive infinite cloud model were made to the Spherical Harmonics method (Dr. Devaus) and the Asymptotic Method (Drs. Germogenova and Konovalov) in the Standard Procedures to Compute Atmospheric Radiative Transfer in a Scattering Atmosphere--Numerical Comparisons of the Methods, July 1976 and December 1976, by the International Association of Meteorology and Atmospheric Physics (I.U.G.G.), Radiation Commission. Table 2 shows the results of the 5 cases studied. In all cases the Monte Carlo method is within 2% of the upward flux calculated by the Spherical Harmonic. The results from the Asymptotic Method are quite similar to the Spherical Harmonic. The comparisons in percentage absorbed are equally good. Figure 11 shows the relative radiances (intensities) in the upward direction for cases 4 and 5. The agreement in the conservative case is extremely good but in case 5 ($\bar{\omega}_0$ = 0.9) there are some discrepencies. It is interesting to note that if one integrates the Monte Carlo radiances with respect to cosine theta to obtain an upward irradiance, that value agrees with the stated upward flux. If the same approach is taken with the Sperical Harmonic radiances, the calculated irradiance is not in agreement with its stated upward flux.

2. Others

Danielson, et al. (1969) used a Monte Carlo method to calculate absorption in semi-infinite layer clouds, with a 0.1 reflecting ground surface. They used a Henyey-Greenstein phase function of g = 0.875, which is quite smooth compared to Deirmendjian's cloud C.1. Cloud model C.1. contains a much sharper forward peak and also more back

Table 2. Comparison between Spherical Harmonic method and Monte Carlo, flux relative relative to π irradiance.

Case	Phase Function	Optical Depth	$\bar{\omega}_o$	θ_o	Spherical Harmonic		Monte Carlo	
					Upward Flux	% Absorption	Upward Flux	% Absorption
1	HAZE L	1	1.0	0°	.1736	0%	.1704	0%
2	HAZE L	1	0.9	0°	.1236	47.8%	.1261	47.9%
3	HAZE L	1	0.9	60°	.2255	67.3%	.2226	67.3%
4	CLOUD C1	64	1.0	0°	2.6587	0%	2.6725	0%
5	CLOUD C1	64	0.9	0°	.3733	88.1%	.3693	87.5%

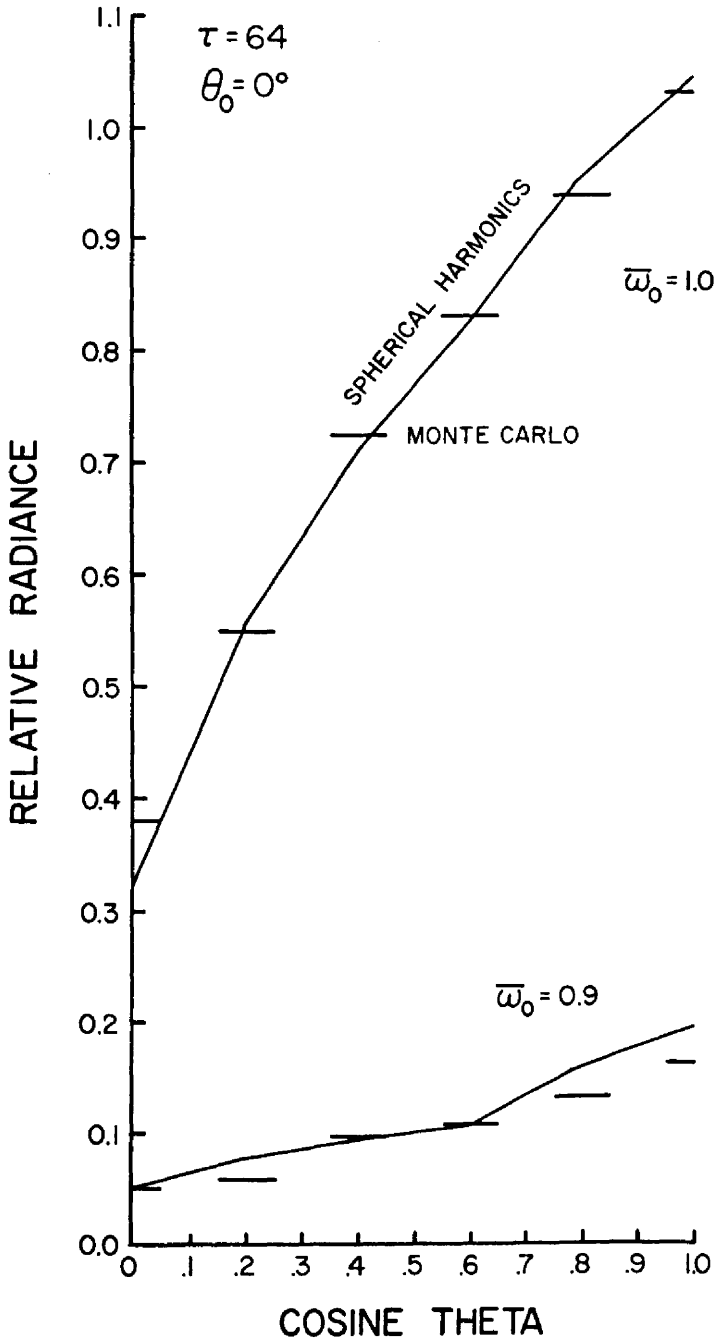

Figure 11. Relative radiance versus cosine θ for the Spherical Harmonics and Monte Carlo methods.

scatter than the Henyey-Greenstein phase function (figure 12). Table 3 contains values estimated from figure 8 of Danielson et al. (1969) and results from the present Monte Carlo method. The present Monte Carlo method seems to consistently have a higher percentage reflected. This can in part be explained by a larger backscatter component in the cloud C.1. phase function than in the Henyey-Greenstein function. Figure 13 compares values estimated from figure 5 of Danielson et al. (1969) to the finite cloud model extended to form a semi-infinite slab cloud for $\lambda = 20$, $\theta_0 = 0^0$, $\bar{\omega}_0 = 0.999$.

Other investigators have calculated absorption in infinite layers over broad spectral regions making direct comparisons difficult.

C. Comparison of finite cloud model to infinite cloud model

The absorbing finite cloud model was expanded to provide an infinite slab cloud (xc = 250 km, a horizontal optical width of 6667) and run at $\tau = 20$, $\theta_0 = 0^0$, $\bar{\omega}_0 = 0.9$ in the partitive weighting mode. Figure 14 shows the relative radiance in all ϕ boxes versus cosine θ for the finite cloud model slab cloud and the infinite cloud model infinite cloud. The results indicate that the two methods are quite similar and hence the finite cloud model functions correctly with absorption. The results to be shown in Section III are all for the finite cloud model in the partitive weighting mode to eliminate inter-modal or inter-model differences.

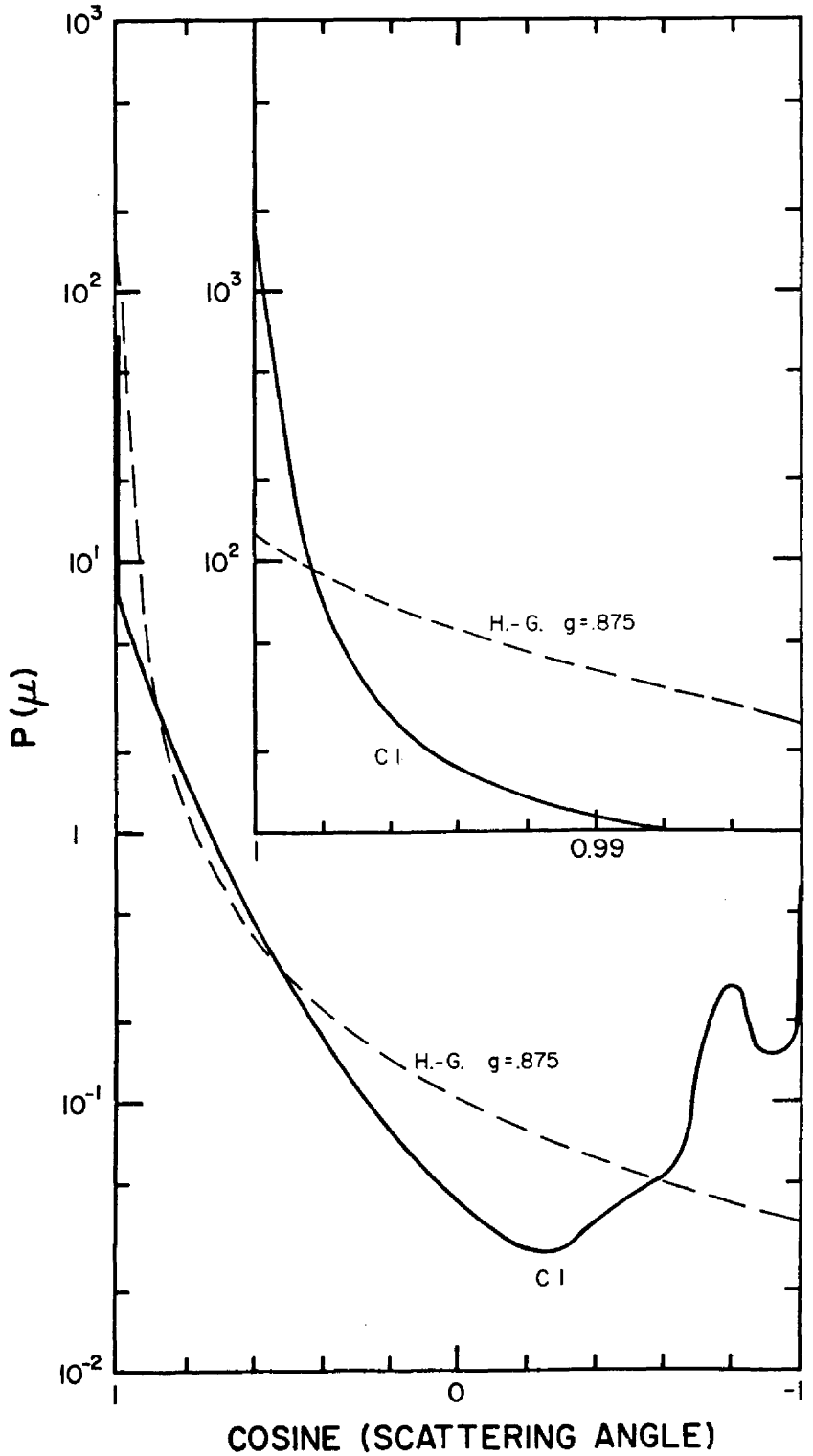

Figure 12. Scattering phase function for C.1. at λ = 0.7 μm and a Henyey-Greenstein function (g = 0.875).

Table 3. Comparison of infinite cloud model to Danielson, et al., for $\bar{\omega}_0 = 0.99$, $\theta_0 = 0$.

	Danielson, et al.	PHATINP
$\tau = 20$		
Absorbed	33.%	33.%
Reflected	38.%	45.%
Transmitted	29.%	22.%
$\tau = 50$		
Absorbed	53.%	48.%
Reflected	44.%	50.%
Transmitted	3.%	2.%

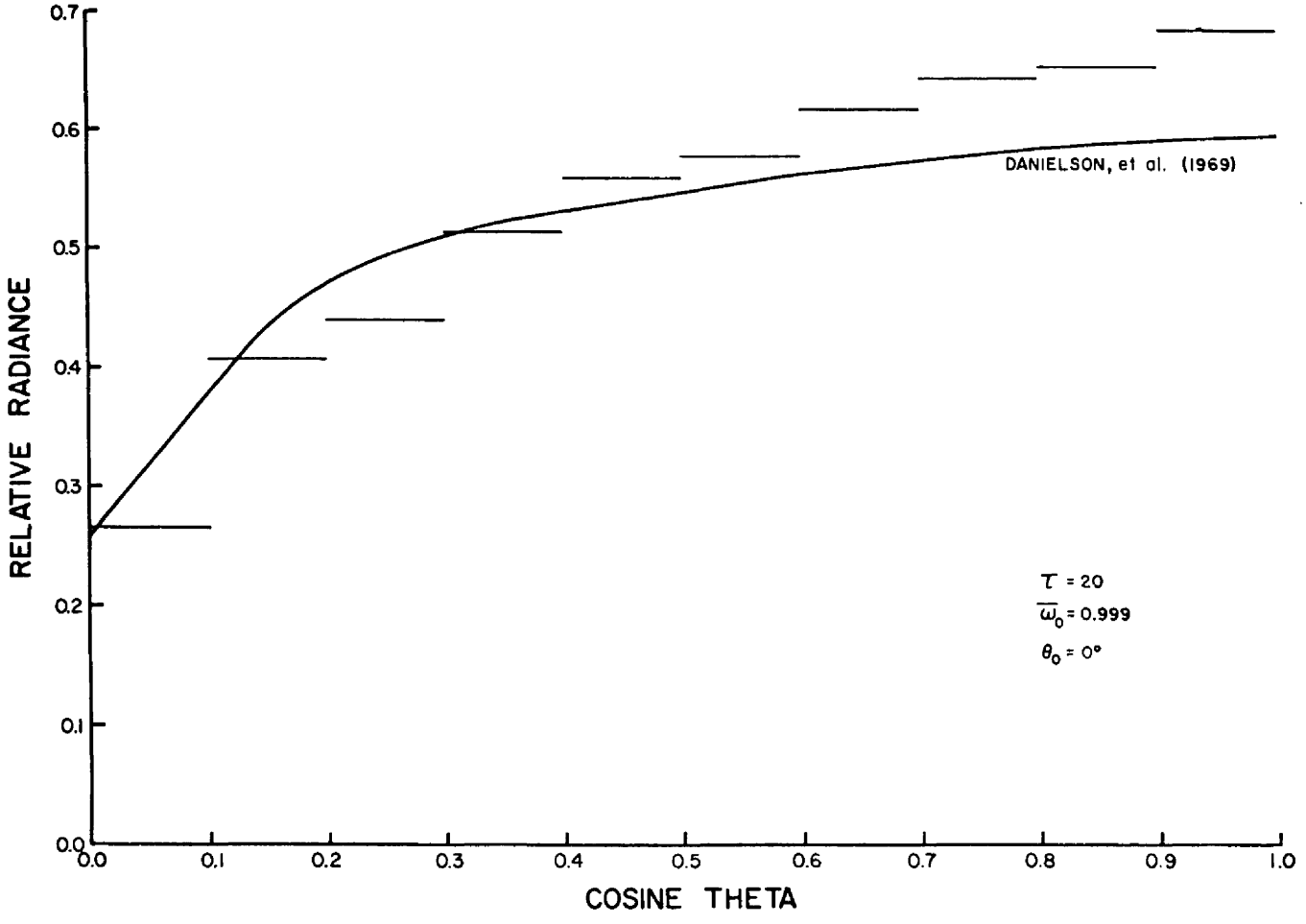

Figure 13. Relative radiance versus cosine θ for Danielson et al. (1969) and the Monte Carlo method PHATINP.

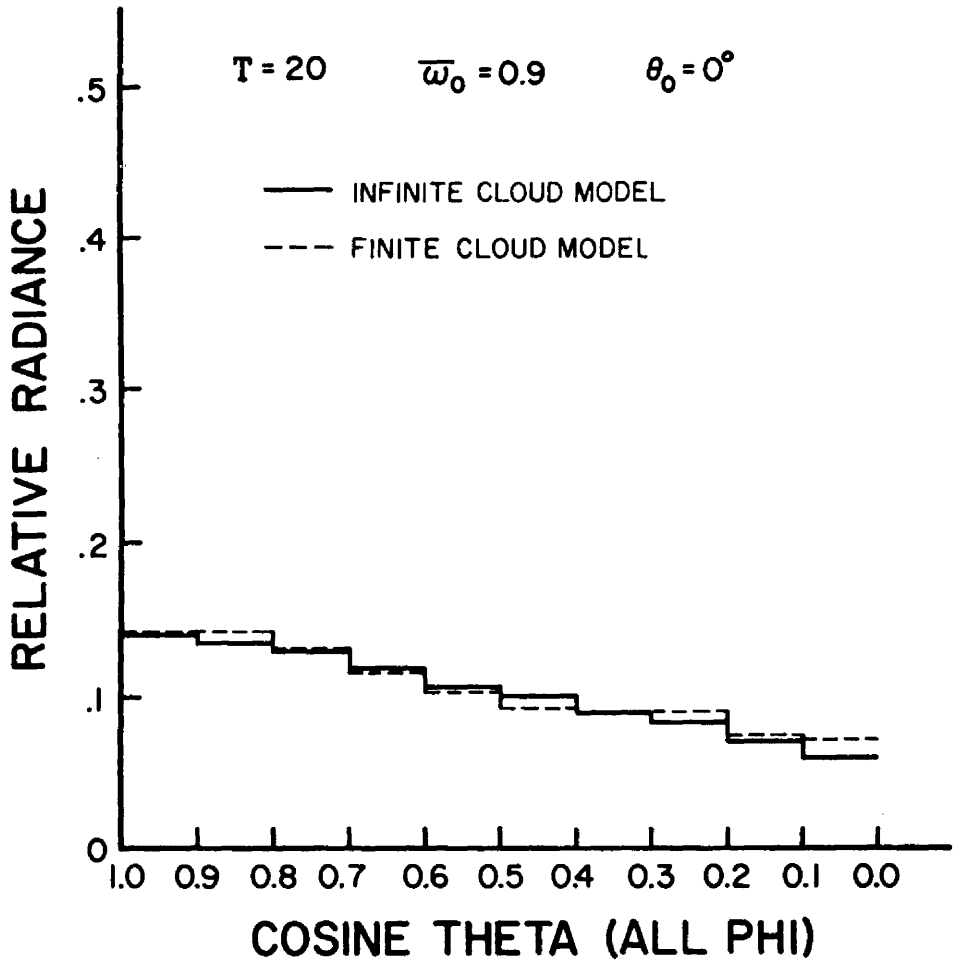

Figure 14. Comparison of radiance results for the infinite cloud model and an infinite slab cloud of horizontal optical width 6667 created from a finite cloud model.

III. Results

Results are shown for the infinite slab cloud ($\tau_{\text{horizontal}} = 6667$) and the finite cubic cloud ($\tau_{\text{horizontal}} = 20$) for solar zenith angle (θ_0) of 0^0, 30^0, and 60^0 for an optical thickness (τ) of 20. Three degrees of absorption and the conservative case were modelled by setting the single scattering albedo ($\bar{\omega}_0$) to 0.9, 0.99, 0.999 and 1.0 respectively. A few select cases at $\tau = 60$, $\theta_0 = 0^0$ were also run.

A. Irradiance results

Figures 15 to 19 illustrate the effects of varying amounts of absorption upon directional reflectance, downward irradiance, fractional absorption and the fraction of the absorption occuring in each of the three cloud layers. For these figures a probability scale was chosen along the abscissa to provide the necessary spacing in $\bar{\omega}_0$. Points were plotted at $\bar{\omega}_0 = 0.9$, $\bar{\omega}_0 = 0.99$, $\bar{\omega}_0 = 0.999$ and freehand curves were drawn to fit the data. Tables 4 and 5 contain the original data.

Figure 15 compares the directional reflectance of the finite cloud to the infinite cloud values for the three amounts of absorption and the three solar zenith angles. The finite cloud is shown to have a lower directional reflectance at moderate to small absorption values and at all solar zenith angles. Photons that enter a finite cloud top near an edge have a much greater probability of escape by exiting the cloud sides heading downward, than by exiting the top, or sides, upward. This edge effect helps to produce the drastic changes from infinite to finite clouds. In figure 15 the infinite cloud shows a steady increase in directional reflectance with decreasing amounts of absorption, while

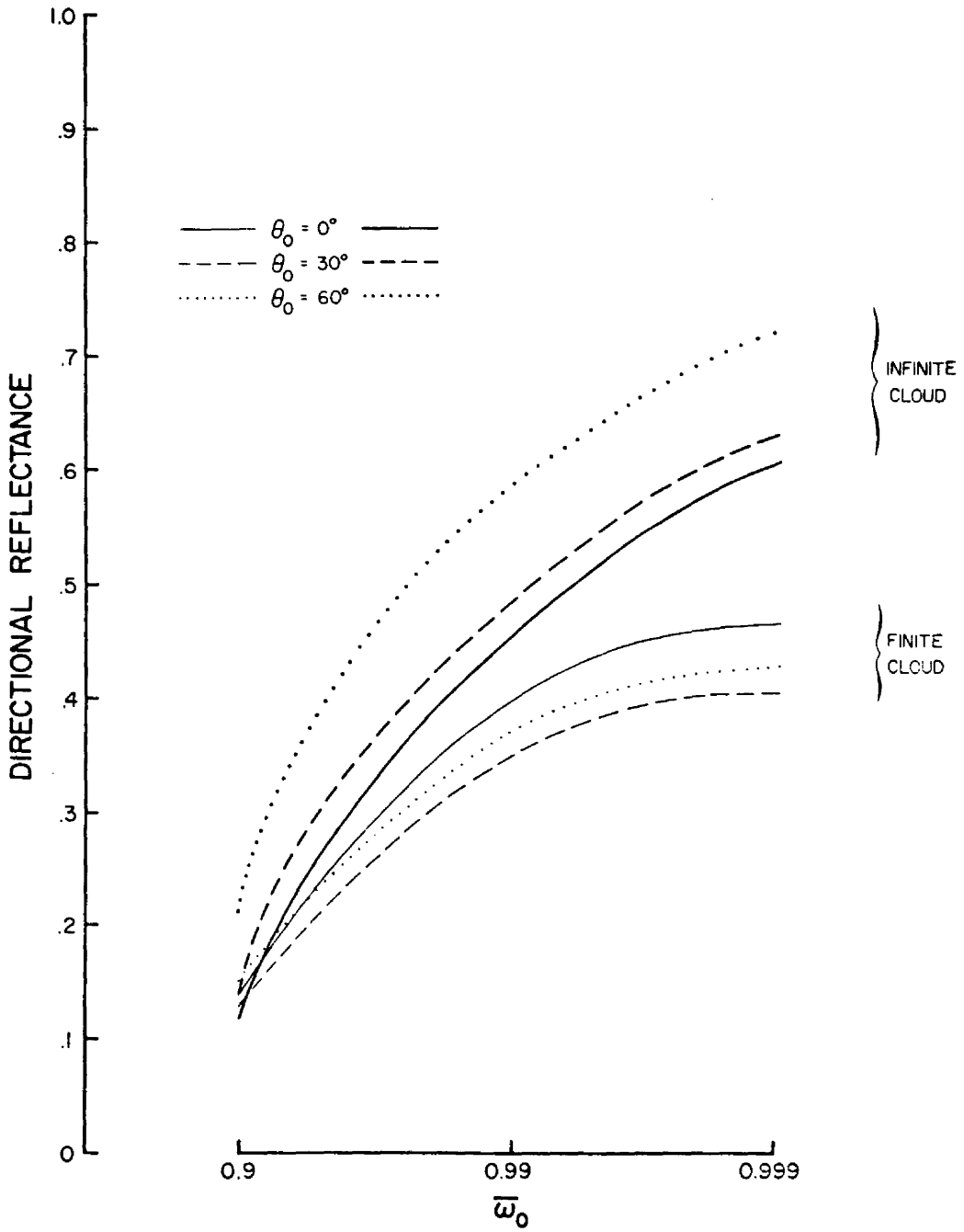

Figure 15. Directional reflectance versus $\bar{\omega}_0$, finite and infinite clouds, τ = 20.

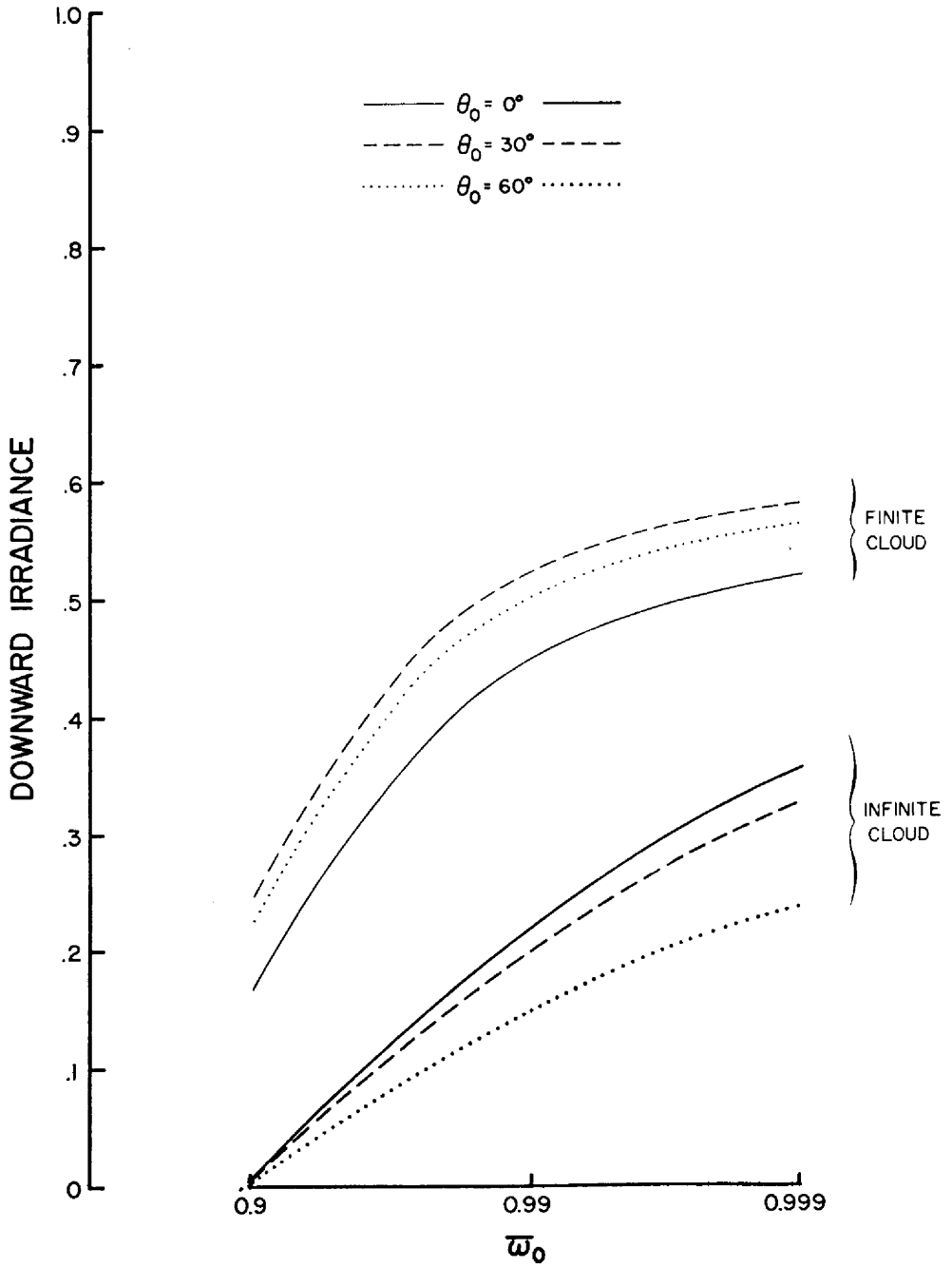

Figure 16. Downward irradiance versus $\bar{\omega}_0$, finite and infinite clouds, $\tau = 20$.

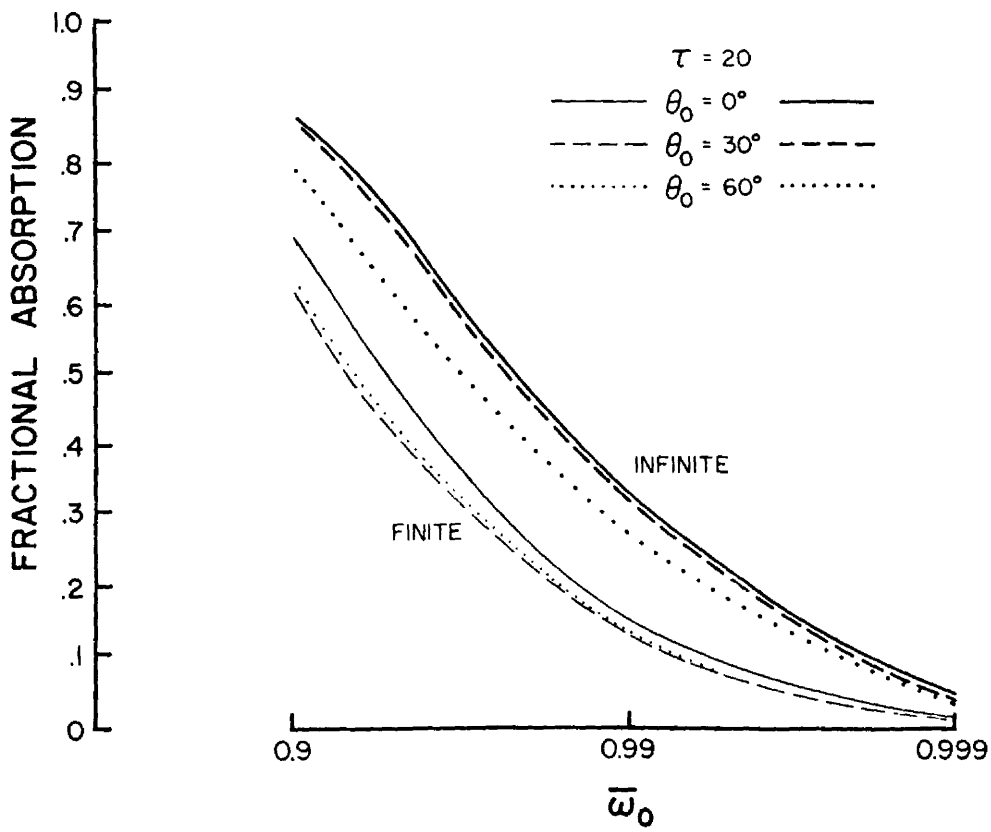

Figure 17. Fractional absorption versus $\bar{\omega}_0$, finite and infinite clouds, $\tau = 20$.

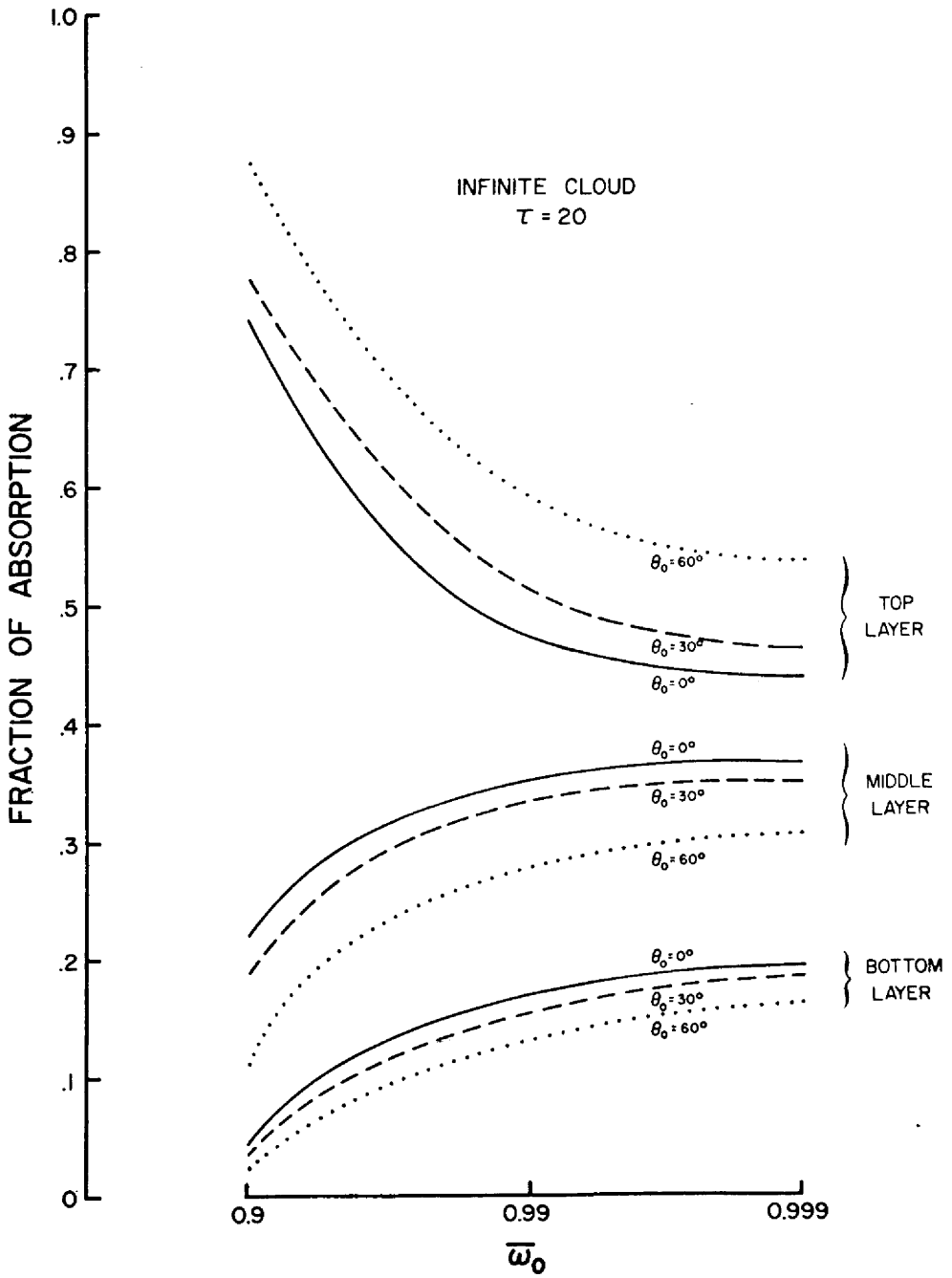

Figure 18. Fraction of absorption versus $\bar{\omega}_0$, for the infinite cloud by layers, $\tau = 20$.

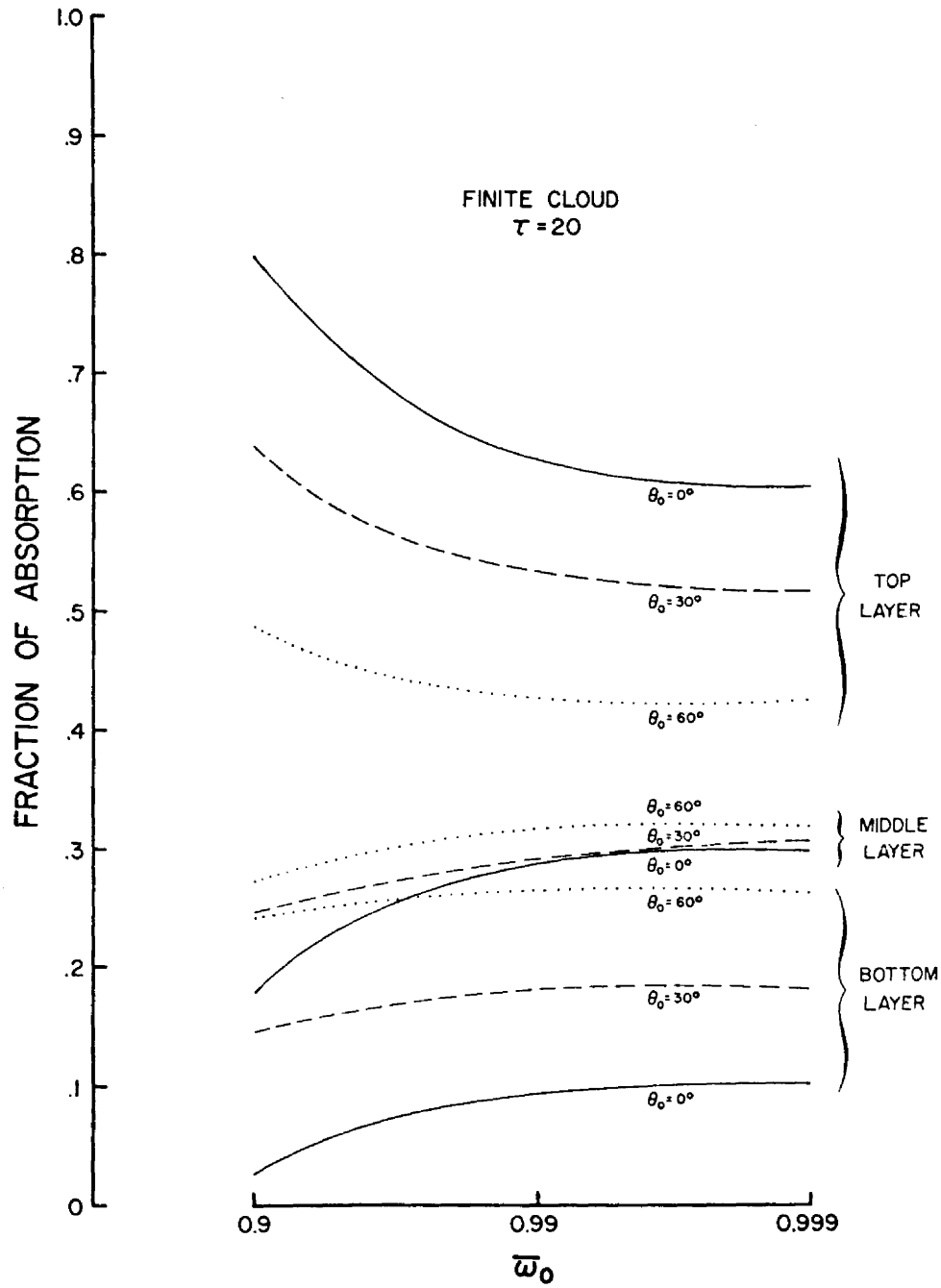

Figure 19. Fraction of absorption versus $\bar{\omega}_0$, for the infinite cloud by layers, $\tau = 20$.

Table 4. Irradiance results infinite cloud, $\tau = 20$.

Case	Directional Reflectance	Downward Irradiance	Fractional Absorption (%)	Fraction Absorbed (%) in Layer 1	2	3
$\theta_0 = 0°$						
$\bar{\omega}_0 = 1.0$	.621	.379	0	0	0	0
$\bar{\omega}_0 = 0.999$	.603	.354	4.3	43.8	36.7	19.5
$\bar{\omega}_0 = 0.99$	.453	.224	32.4	47.6	35.3	17.2
$\bar{\omega}_0 = 0.9$	.119	.012	86.8	73.6	21.9	4.5
$\theta_0 = 30°$						
$\bar{\omega}_0 = 1.0$	.657	.343	0	0	0	0
$\bar{\omega}_0 = 0.999$	.626	.331	4.3	46.0	35.3	18.6
$\bar{\omega}_0 = 0.99$	.485	.200	31.4	51.2	33.2	15.6
$\bar{\omega}_0 = 0.9$	.134	.010	85.6	77.6	18.8	3.7
$\theta_0 = 60°$						
$\bar{\omega}_0 = 1.0$	.747	.253	0	0	0	0
$\bar{\omega}_0 = 0.999$	.719	.244	3.7	53.2	30.7	16.1
$\bar{\omega}_0 = 0.99$	.585	.145	27.0	59.1	27.9	13.1
$\bar{\omega}_0 = 0.9$	.214	.006	78.0	87.1	10.9	2.1

Table 5. Irradiance results finite cloud, $\tau = 20$.

Case	Directional Reflectance Total	Directional Reflectance Top	Downward Irradiance Total	Downward Irradiance Bottom	Fractional Absorption (%)	Fraction Absorbed (%) in Layer 1	2	3
$\theta_0 = 0$								
$\bar{\omega}_0 = 1.0$	.468	.239	.532	.066	0	0	0	0
$\bar{\omega}_0 = 0.999$	.461	.237	.522	.064	1.7	60.3	29.6	10.1
$\bar{\omega}_0 = 0.99$	.397	.211	.456	.051	14.7	62.5	28.3	9.2
$\bar{\omega}_0 = 0.9$	.138	.091	.172	.005	69.0	79.4	17.9	2.7
$\theta_0 = 30°$								
$\bar{\omega}_0 = 1.0$	.408	.177	.592	.162	0	0	0	0
$\bar{\omega}_0 = 0.999$	.403	.177	.583	.159	1.4	51.4	30.4	18.2
$\bar{\omega}_0 = 0.99$	.349	.157	.526	.143	12.5	53.0	28.9	18.1
$\bar{\omega}_0 = 0.9$	.129	.068	.253	.072	61.8	63.6	22.0	14.5
$\theta_0 = 60°$								
$\bar{\omega}_0 = 1.0$	.430	.178	.570	.194	0	0	0	0
$\bar{\omega}_0 = 0.999$	.421	.176	.565	.190	1.4	42.2	31.7	26.1
$\bar{\omega}_0 = 0.99$	.368	.156	.506	.175	12.6	42.4	31.4	26.2
$\bar{\omega}_0 = 0.9$	.149	.068	.232	.083	62.0	48.6	27.2	24.3

the finite cloud levels off with decreasing absorptions. The edge effect in the finite cloud reduces the effects of small absorption since the photons may escape before being absorbed. The infinite cloud shows higher directional reflectances with increasing solar zenith angle (θ_0) as photons enter in an increasingly tangential manner and are able to escape in an upward direction. The finite cloud shows a maximum directional reflectance when the sun is vertical and a minimum at a larger solar zenith angle. Once the sun is tipped off the vertical photons enter the +y face and the edges between the +y and the x faces allow light to exit the x faces after travelling only a short distance within the cloud. At $\theta_0 = 60^0$ photons entering the top or +y face need only be scattered upward by greater than 30° to contribute to the directional reflectance from either the top or the sides. Table 5 shows the influence of the sides upon directional reflectance and downward irradiance by subtracting the total value by either the top value or the bottom value respectively.

The downward irradiances for these cases are shown in figure 16. At $\bar{\omega}_0 = 0.9$ almost no light is going downward from the infinite cloud while the finite cloud is allowing approximately 20% of the incident light to escape downward. The infinite cloud shows decreasing downward irradiance with increasing solar zenith angle. The finite cloud shows a minimum downward irradiance at $\theta_0 = 0^0$, and a maximum at a larger θ_0. The reasoning is analogous to that given above.

The probability of a photon being totally absorbed increases as the photon remains within the cloud. Tangential entry and multiple edge effects decrease abosrption in clouds. Figure 17 shows the fraction of the incident light absorbed versus $\bar{\omega}_0$ for the three sun

angles for the finite and infinite clouds. The finite cloud shows less absorption in each case than the infinite cloud. The infinite cloud shows the greatest amounts of absorption when the sun is vertical and the least when the solar zenith angle is 60°. The finite cloud also shows a maximum at $\theta_0 = 0^0$ but slightly less absorption at $\theta_0 = 30°$ than at $\theta_0 = 60°$.

The cloud model was divided into three 0.5 km thick layers and the number of photons absorbed in each layer were counted. Figure 18 shows the fraction of the total absorption in each layer for the infinite cloud cases, figure 19 shows the same for the finite cloud cases. The infinite cloud shows the expected decrease in the fraction of absorption with depth as fewer and fewer photons survive to greater depths. With stronger absorption amounts the middle and bottom layers decrease rapidly in importance. With increasing solar angle a larger fraction is absorbed in the top layer with a corresponding decrease in the lower two layers, with the middle layer showing the greatest decrease.

The finite cloud (figure 19) shows a more complicated situation as photons are able to enter the middle and bottom layer directly along the +Y face as the sun is tipped off the vertical. The greatest fraction of the absorption occurs in the top layer with the bottom layer usually showing the smallest fraction of absorption at all $\bar{\omega}_0$ and all sun angles. As the sun is tipped off the top layer decreases in importance as the bottom and middle layers show corresponding increases with the bottom layer showing the greater increase. At $\theta_0 = 0^0$ the bottom layer accounts for less than 11% of the absorption while at $\theta_0 = 60^0$ about 25% is absorbed in the bottom layer.

It should be noted that in the previous discussion absorption has been taken to mean the fractional absorption, i.e. the fraction of the incident photons that are absorbed. A finite cloud however presents a larger cross section to an inclined solar beam than an equal volume of an infinite cloud. Hence a finite cloud receives $1 + \tan \theta_0$ times the amount received by an equal horizontal area element of infinite cloud. The total absorption is then $1 + \tan \theta_0$ times the stated fractional absorption for the finite cloud. Such calculations indicate that the finite cloud absorbs more at a solar zenith angle of 30° when $\bar{\omega}_0 = 0.9$ and also at $\theta_0 = 60^0$ when $\bar{\omega}_0 = 0.99$ and $\bar{\omega}_0 = 0.9$. The single scattering albedo for natural clouds is usually assumed to be of order 0.999 in the visible region of the spectrum. In such a case the finite cloud would absorb about the same amount as an equal volume of an infinite cloud at $\theta_0 = 60^0$, but less at $\theta_0 = 0^0$ and 30^0.

Figures 20 to 24 illustrate the effects of increasing the optical depth from 20 to 60 for a vertical sun. As the computer running time increases with increasing optical depth, only one sun angle was run at all four amounts of absorption. Table 6 contains the results which were plotted in the same manner as graphs presented earlier. Figure 20 illustrates the increase in directional reflectance versus $\bar{\omega}_0$ as the optical depth increases from 20 to 60 in both the finite and infinite cases. The effect of increased optical depth is most evident at lower absoption abounts and the finite cloud as before seems to be leveling off at $\bar{\omega}_0 = 0.999$ while the infinite cloud is still getting brighter with decreasing absorption. Increasing the optical depth threefold seems to bring about only a 20-30% increase in directional reflectance in both cases.

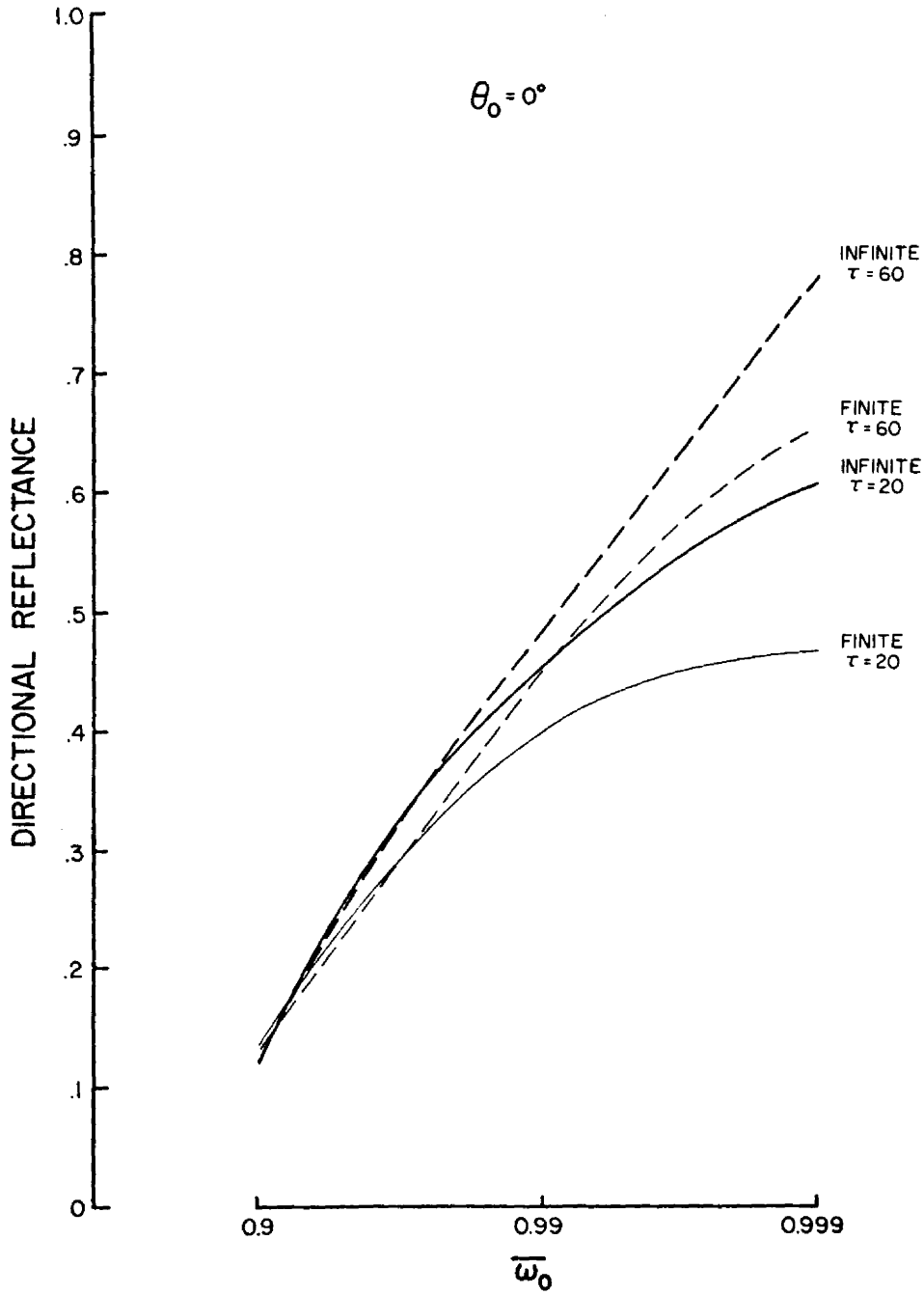

Figure 20. Directional reflectance versus $\bar{\omega}_0$, for the finite and infinite clouds, $\tau = 20$ and $\tau = 60$, $\theta_0 = 0°$.

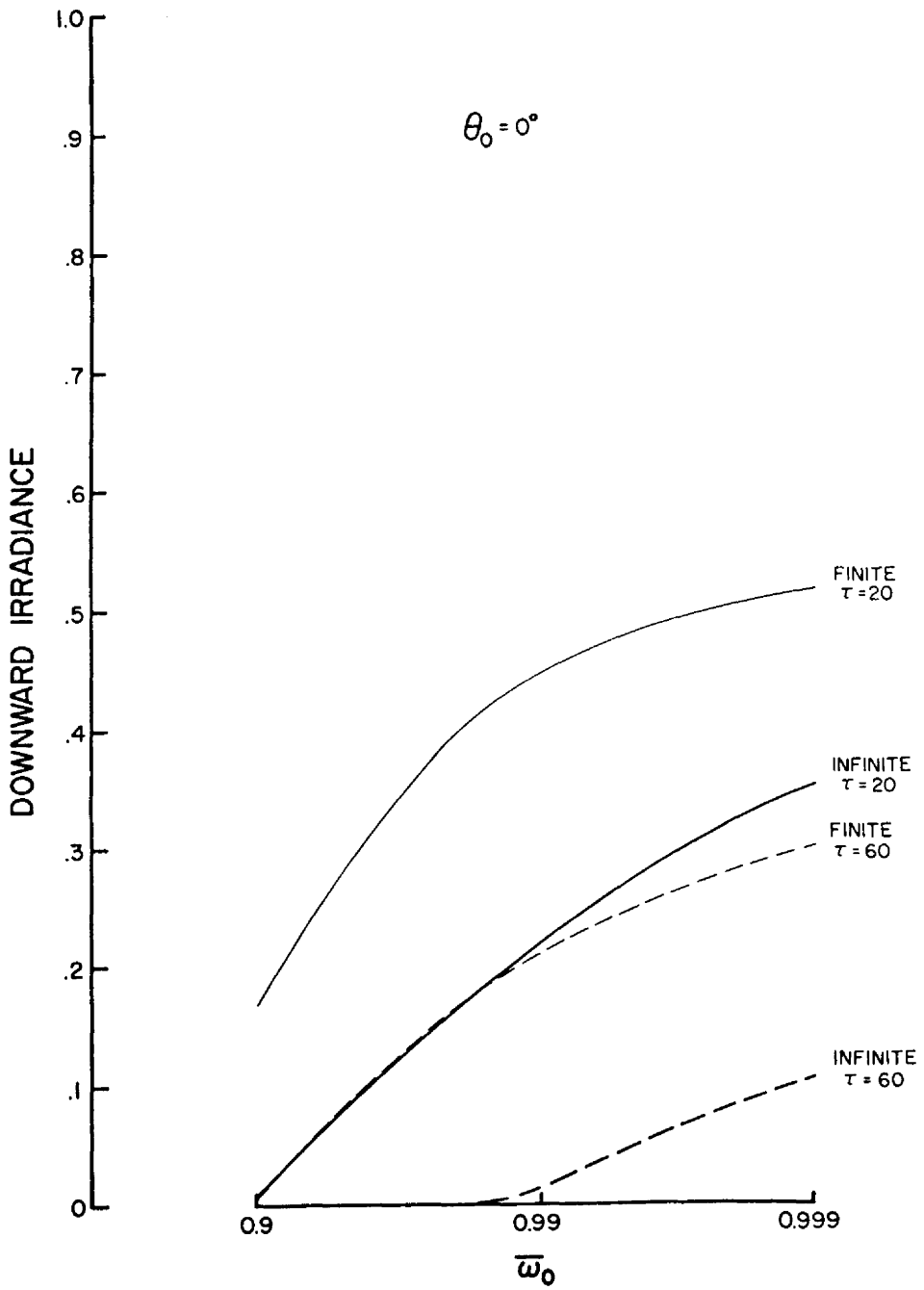

Figure 21. Downward irradiance versus $\bar{\omega}_0$, for the finite and infinite clouds, $\tau = 20$ and $\tau = 60$, $\theta_0 = 0°$.

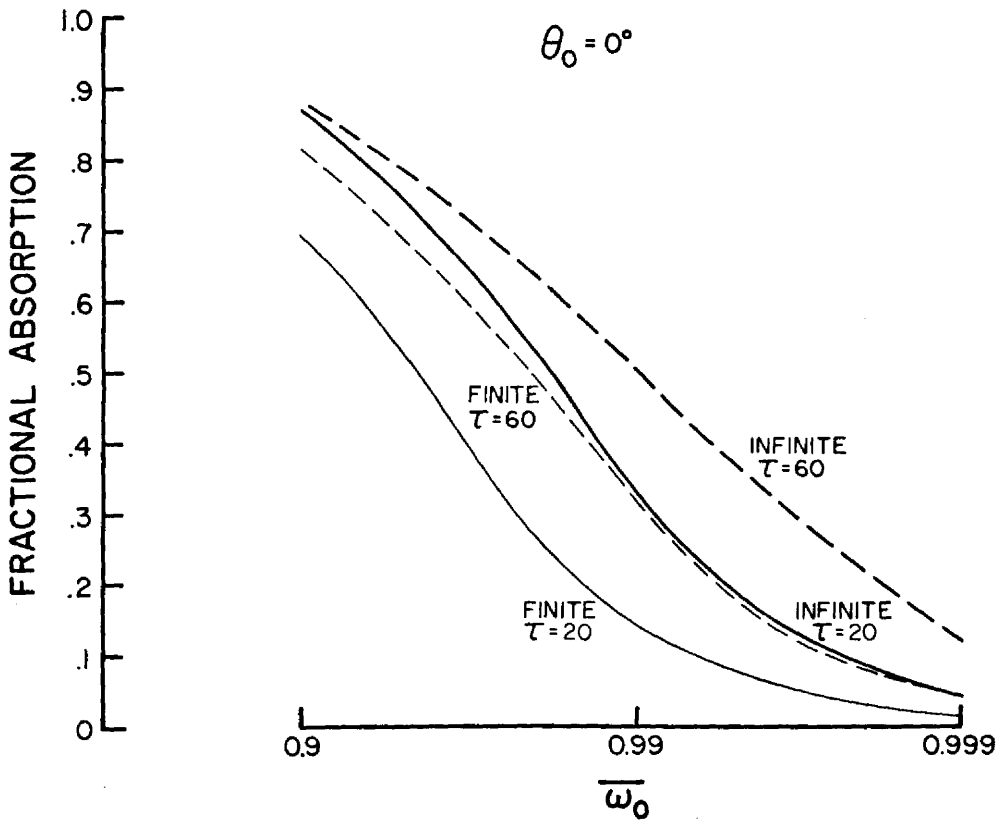

Figure 22. Fractional absorption versus $\bar{\omega}_0$, for the finite and infinite clouds, $\tau = 20$ and $\tau = 60$, $\theta_0 = 0°$.

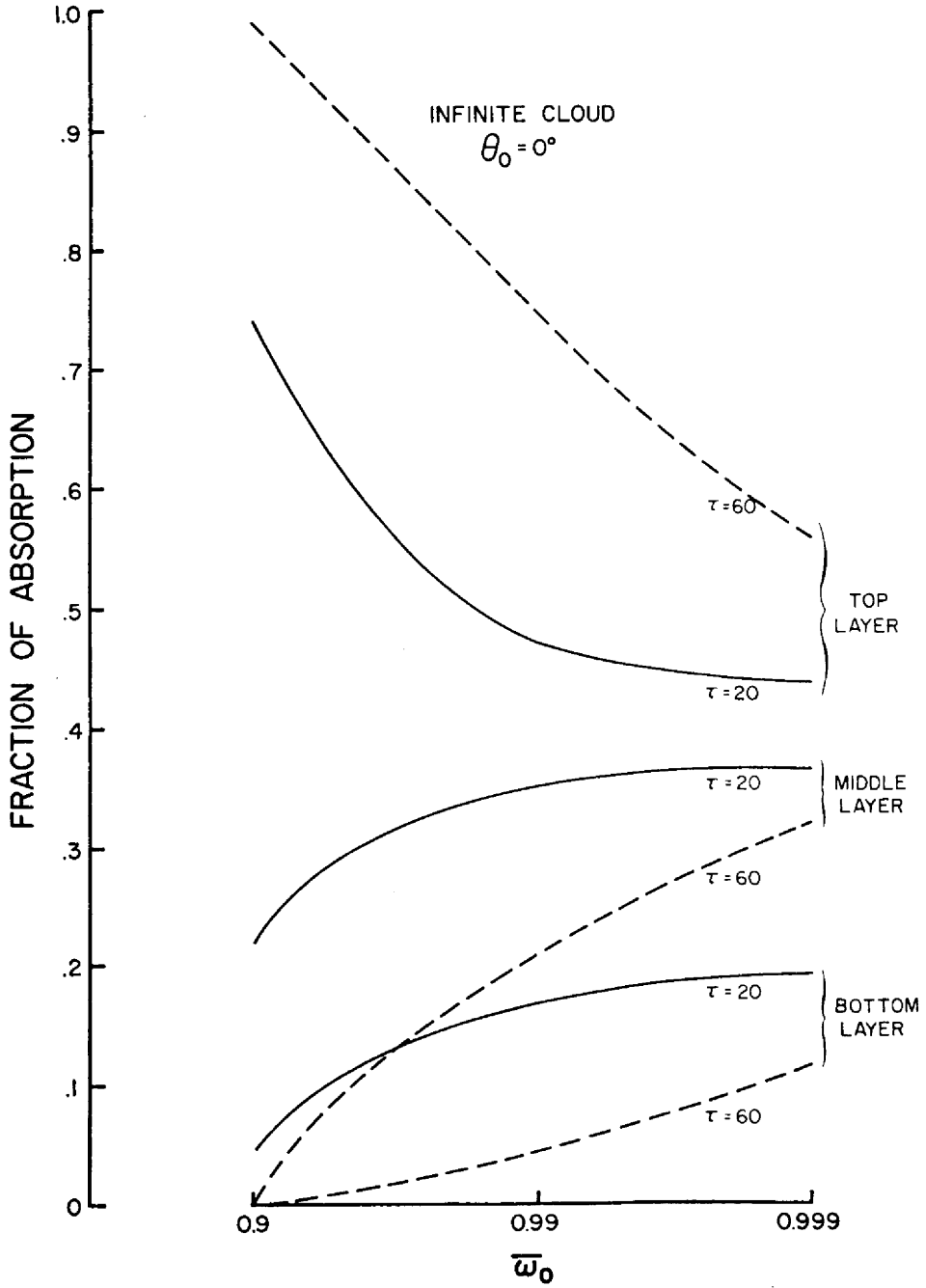

Figure 23. Fraction of absorption versus $\bar{\omega}_0$, for the infinite cloud by layers, $\theta_0 = 0°$, $\tau = 20$ and $\tau = 60$.

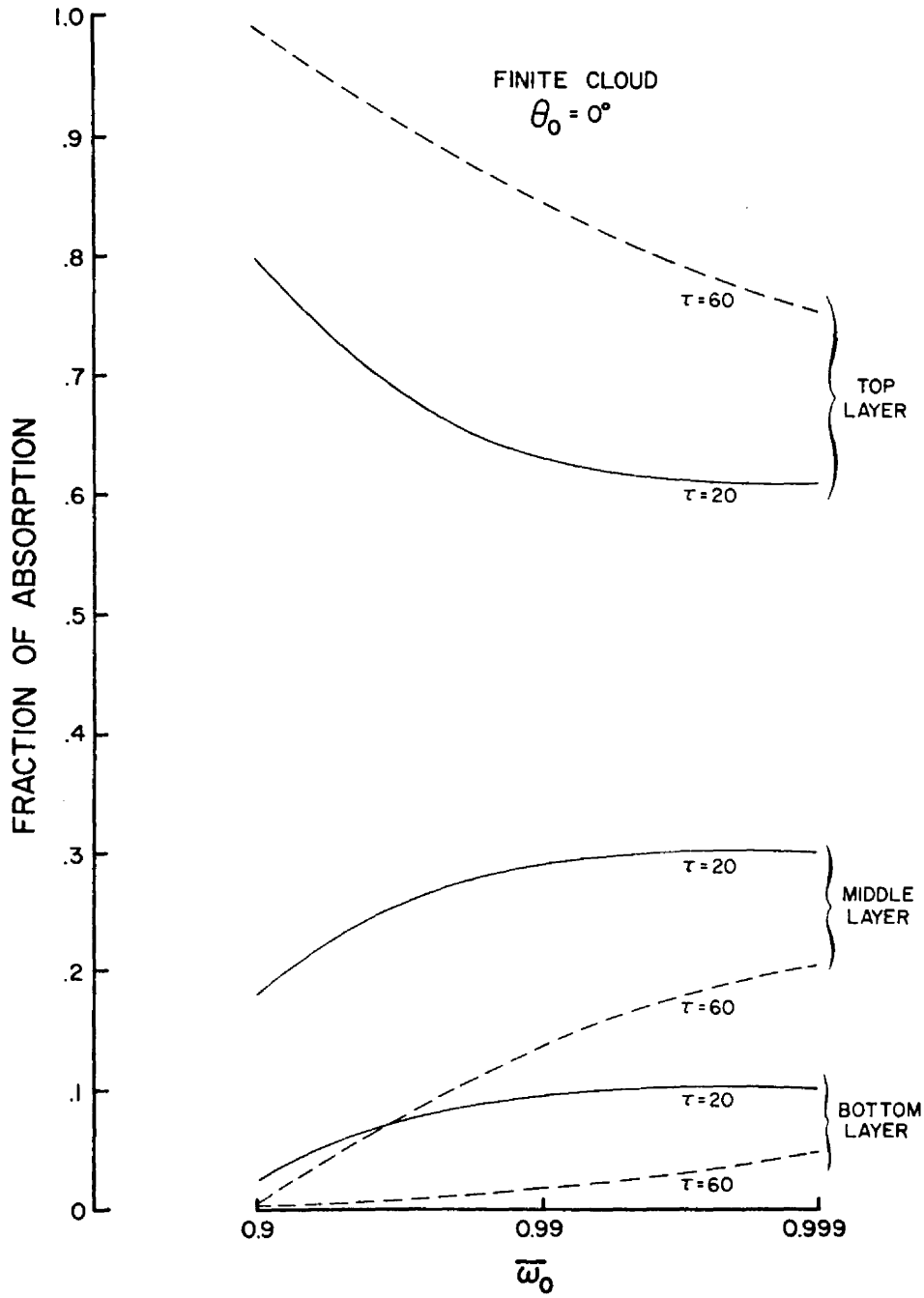

Figure 24. Fraction of absorption versus $\bar{\omega}_0$, for the finite cloud by layers, $\theta_0 = 0°$, $\tau = 20$ and $\tau = 60$.

Table 6. Irradiance results $\tau = 60$.

Case	Directional Reflectance		Downward Irradiance		Fractional Absorption (%)	Fraction Absorbed (%) in Layer		
	Total	Top	Total	Bottom		1	2	3
$\tau = 60$, Finite, $\theta_0 = 0°$								
$\bar{\omega}_0 = 1.0$	.668	.460	.332	.016	0	0	0	0
$\bar{\omega}_0 = 0.999$	.650	.454	.303	.012	4.7	74.9	20.5	4.6
$\bar{\omega}_0 = 0.99$	.477	.354	.214	.003	30.9	84.2	13.9	1.9
$\bar{\omega}_0 = 0.9$	.130	.112	.060	.000	81.0	99.1	0.9	0
$\tau = 60$, Infinite, $\theta_0 = 0°$								
$\bar{\omega}_0 = 1.0$	.865		.135		0	0	0	0
$\bar{\omega}_0 = 0.999$	.774		.105		12.1	56.1	32.1	11.8
$\bar{\omega}_0 = 0.99$	.480		.014		50.6	74.4	21.1	4.5
$\bar{\omega}_0 = 0.9$	.118		0		88.2	98.9	1.1	0

Figure 21 shows the decrease in downward irradiance with increasing optical depth as a function of the single scattering albedo. When the optical depth is increased from 20 to 60 the downward irradiance from the finite cloud decreases 38% to 65% (Table 6) as $\bar{\omega}_0$ decreases from 1.0 to 0.9. The infinite cloud decreases in downward irradiance 64% to 98%. The finite cloud always lets more light escape downward than an equally thick infinite cloud with the same single scattering albedo and the percentage decreases in downward irradiance is less in the finite cloud with increasing optical depth than in the infinite cloud.

With an increase in optical depth an increase in the number of encounters occurs allowing a greater fraction of the light incident to be absorbed. Photons in a finite cloud have a greater opportunity to escape after a few encounters than photons in an infinite cloud. Figure 22 illustrates the increase in the fraction of the incident photons that is absorbed for two optical depths as the single scattering albedo is decreased in both the finite and infinite cases. At $\bar{\omega}_0$ = 0.999 the infinite cloud and finite cloud both show an increase of about 180% in fractional absorption while at $\bar{\omega}$ = 0.99 the infinite cloud shows a 56% increase while the finite cloud shows 110% increase. At $\bar{\omega}$ = 0.9 the infinite cloud shows only a 1.5% increase while the finite cloud increases 17.4%. With stronger absorption the photons are being absorbed before they can escape from a finite cloud resulting in increases with optical depth greater than for the infinite cloud. Figures 23 and 24 show the fraction of total absorption by layers for τ = 20 and τ = 60 for the infinite and finite clouds respectively. As the optical depth increases more photons are absorbed in the top layer and tne middle and bottom layers show less absorption. At

$\bar{\omega}$ = 0.9 virtually all of the absorption occurs in the top layer in both the finite and infinite clouds of τ = 60.

Increasing the optical depth of finite and infinite clouds from τ = 20 to τ = 60 with the sun vertical produces about a 25% increase in directional reflectance in both cases, a larger increase in absorption in the finite cloud than the infinite, and smaller decrease in downward irradiance in the finite cloud than in the infinite cloud.

B. Radiance results

The following graphs compare the radiance values from the total infinite cloud, the total cube cloud, and the cube top or bottom alone, as a function of cosine θ for an optical depth of 20. The first of the two graphs in each set shows the relative radiance in all ϕ boxes as a function of cosine θ from directly upward ($\cos\theta$ = 1.0) through horizontal ($\cos\theta$ = 0.0) to directly downward ($\cos\theta$ = -1.0). This type of graph could be integrated to provide the upward irradiance and the downward irradiance. The second graph in each set of two illustrates a scan from the -Y axis in the phi box 0°-15° through the vertical Z axis and down to the horizontal +Y axis in the phi box 165°-180°. It represents a scan of the cloud viewed from above in a slice containing the solar plane (see figure 5). The dashed line on this graph represents the cube top alone.

The conservative cases illustrate the basic differences due to geometric considerations. The conservative case ($\bar{\omega}_0$ = 1.0) with the sun vertical ($\theta_0 = 0^0$) is shown in figures 25 and 26. The solid line represents the infinite cloud, the dotted line represents the total cube cloud and the dashed line represents the cube top or cube bottom

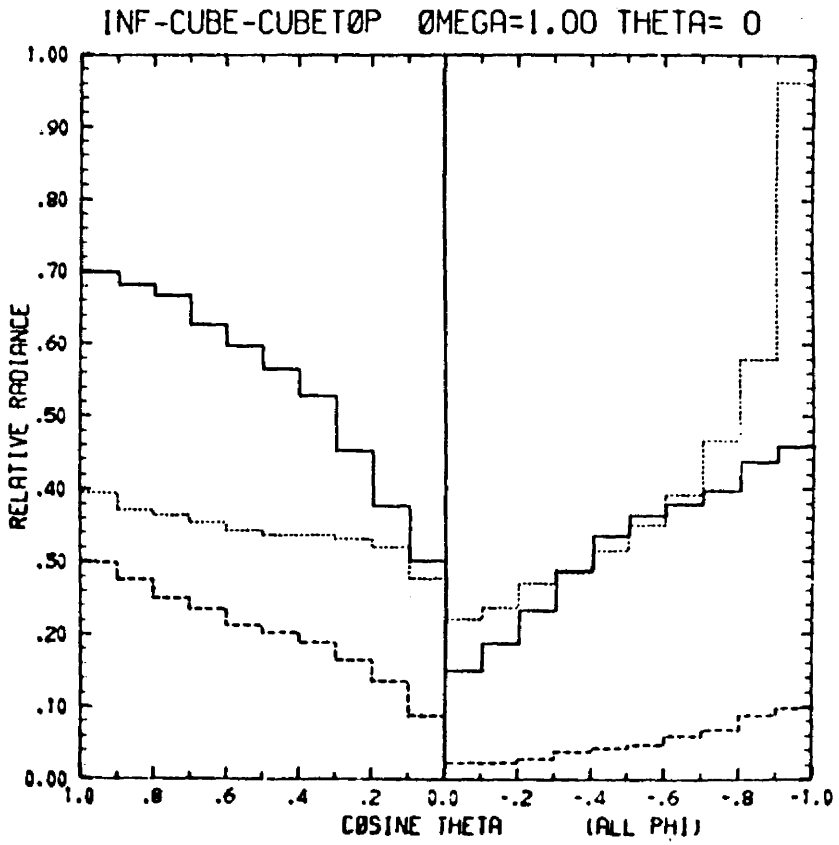

Figure 25. Upward and downward radiance (all ϕ) vs. cosine θ, for τ=20, $\bar{\omega}_o$ = 1.0, θ_o=0° (infinite ———, total cube ·····, cube top------).

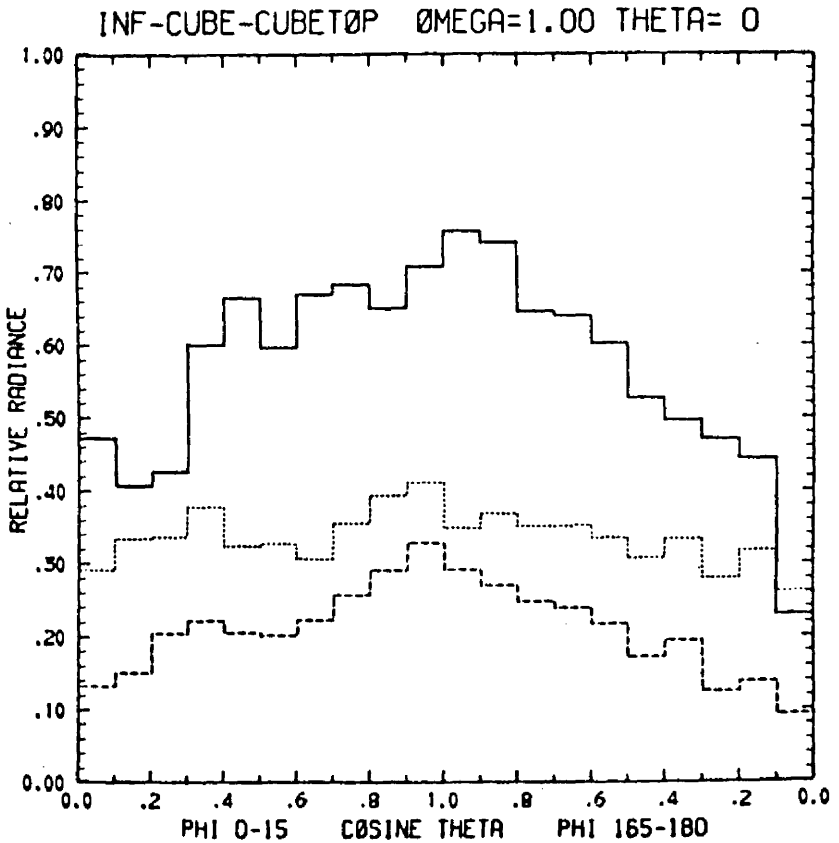

Figure 26. Upward radiance near the solar plane vs. cosine θ, for τ =20, $\bar{\omega}_o$ = 1.0, θ_o = 0°. (Infinite ———, total cube ·····, cube top -----).

alone. Figure 25 for all ϕ boxes indicates that the infinite cloud top monotonically decreases in brightness as you go from the vertical to the horizontal. The infinite cloud bottom monotonically increases from horizontal to directly downward. The cube top and cube bottom show similar patterns but with much lower values and less slope. The total cube cloud shows a much flatter response in the upward direction due to the addition of light from the sides going upward. The upward values from the cube top and sides are considerably less than the infinite cloud and greater than the cube top alone. In the downward direction the cube top and sides show monotonically increasing values with a large spike heading nearly directly downward. This spike is due to light entering the top and exiting the sides heading downward at small angles with respect to the sides. The cube cloud shows a lower upward irradiance and a higher downward irradiance than the infinite cloud as a result of light exiting the cube sides in a downward direction.

Figure 26 illustrates the vertical scan for the conservative case with the sun vertical. This type of graph exhibits much more Monte Carlo noise than the all phi graphs as a result of limiting the output to two ϕ boxes of only 15° each. The infinite cloud exhibits a somewhat symmetric distribution with the cloud appearing brightest near the vertical. The cube top demonstrates a similar pattern but at lower values. The total cube cloud shows a much flatter response with higher values than the cube top alone. The light exiting the sides in an upward direction must increase from the vertical towards the horizontal to produce such a flattened response.

When the sun is tipped off the vertical light is now incident upon the +Y face of the finite cloud. Since the light is uniformly distributed over the incident faces and travelling in a slant direction, some light may enter an edge of a face and exit the cloud through the adjacent edge after only a few encounters. Figures 27 and 28 illustrate the conservative case with the solar zenith angle equal to 30°. The infinite cloud in Figure 27, shows again a monotonic decrease from vertical to horizontal but with a flatter response than at $\theta_o = 0°$. The infinite cloud's downward response shows again a monotonic increase from horizontal to vertically downward. Light entering an infinite cloud at an acute angle to the top surface need only be turned a small angle through scattering to escape the top, hence infinite clouds become brighter as the sun is tipped off the vertical. The finite cloud top produces a flatter response at 30° than at 0° due to this edge enter-exit effect with the sides contributing some light which exits the top of the cloud. The total cube cloud produces a similar pattern but with higher values due to light from the sides. In the downward direction at $\theta_o = 30^o$, the edge effect produces a downward spike around $\cos\theta = -0.85$. This is evident in the bottom only response (dashed line) and also in the total cube downward response (dotted line). The total cube downward spike is larger due to the addition of light entering the -Y, X edge and exiting the -Y face after only a few scatters.

The scan in cosine θ graph with $\theta_o = 30^o$ produces a slight shift of the maximum from the vertical towards the incident sun angle and a secondary maximum at about $\cos\theta = 0.2$ in the ϕ box 0°-15°. This pattern is due to light being scattered a few times and exiting

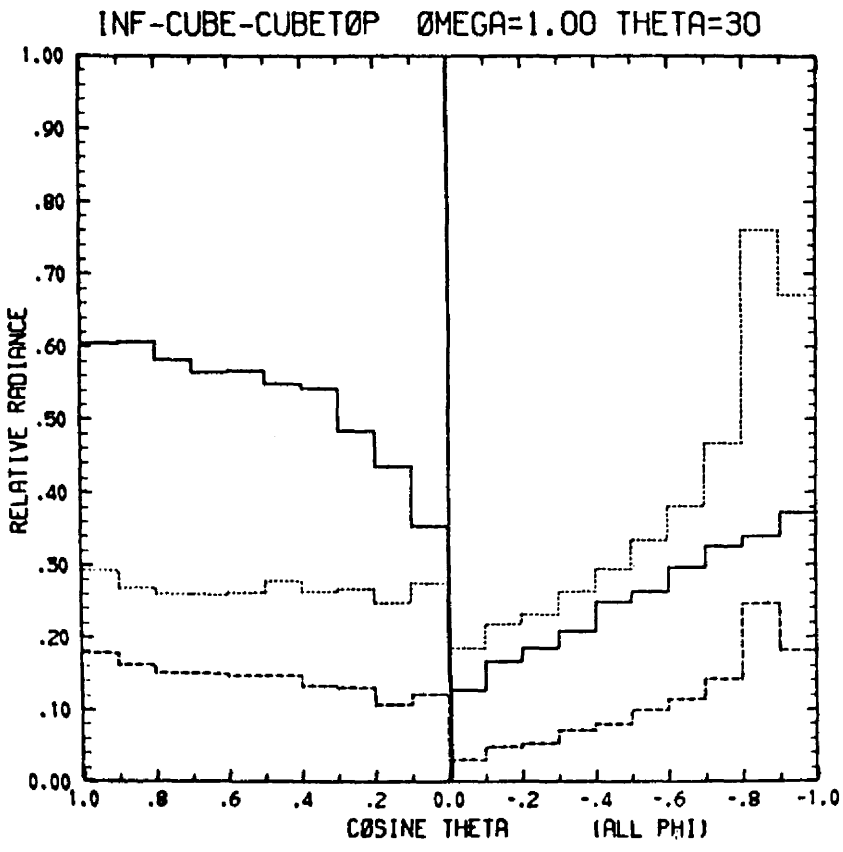

Figure 27. Same as figure 25 except $\theta_o = 30^o$

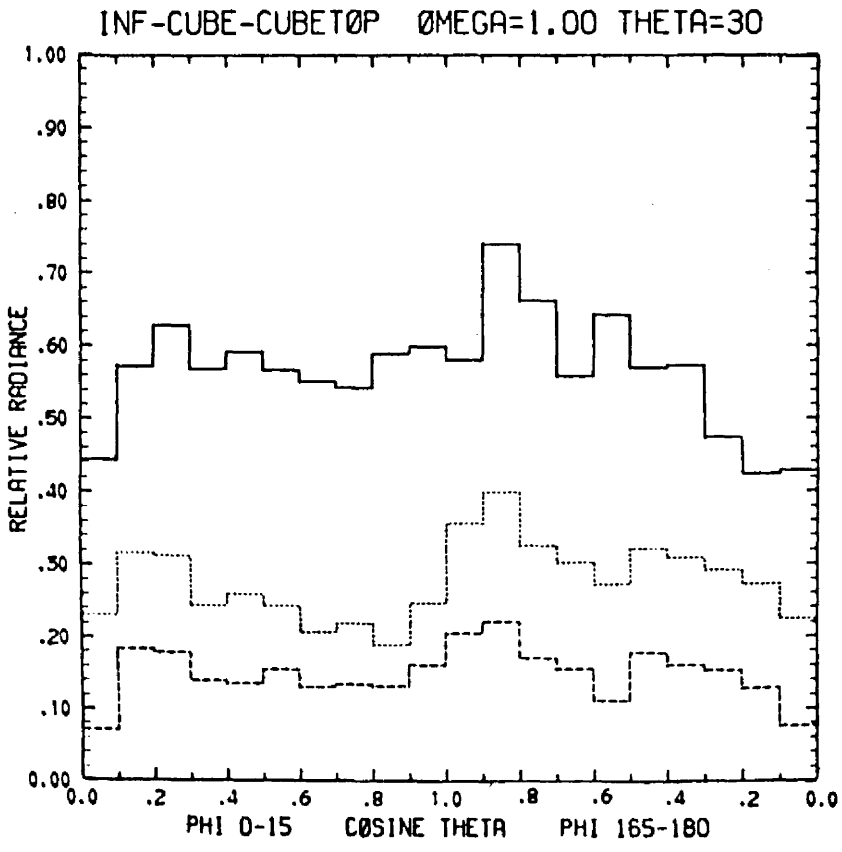

Figure 28. Same as figure 26 except $\theta_o = 30^o$.

the top of the cloud. This secondary maximum is observed in all three lines, the infinite cloud, the total cube cloud, and the cube top alone. The shifted center maximum is a backscatter phenomena.

Figure 29 and 30 illustrate the conservative case with the sun tipped off at 60°. The pattern of upward radiance at all ϕ now changes to a nearly monotonic increase from vertical to horizontal in all three cases. At 60^0 photons need only scatter 30^0 to be heading upward. The vertical scales on figures 29 and 30 have been changed from 1.0 to 0.5 and 1.4 respectively. The reduced values on the all phi graph are due to the decreased input as a result of increased zenith angle. The cube top and total cube in the downward direction show a peak at cosine θ = 0.5 due to edge effects.

Figure 30 illustrates the upward scan from -Y to +Y axes. The infinite cloud shows increasing values with low angles above the -Y axis as a result of light entering only 30^0 above the surface being scattered a few times and escaping upward at low angles. The secondary peak at $\cos\theta$ = 0.5 in the ϕ 165^0 - 180^0 box is a backscatter phenomena. The cube photons entering at $\theta_0 = 60^0$ have a greater opportunity to escape the sides heading downward than to escape the top going upward. The total cube shows only slightly greater values above the -Y direction than the top alone. In the +Y direction the sides contribute about as much as the top alone.

The effects of absorption with the sun vertical upon the radiance patterns of the infinite cloud are illustrated in figure 31 and 32, and for the finite cloud in figures 33 and 34. In these figures all four values of the single scattering albedo are shown with the solid line representing $\bar{\omega}_0 = 1.0$, the dotted line representing $\bar{\omega}_0 = 0.999$, the

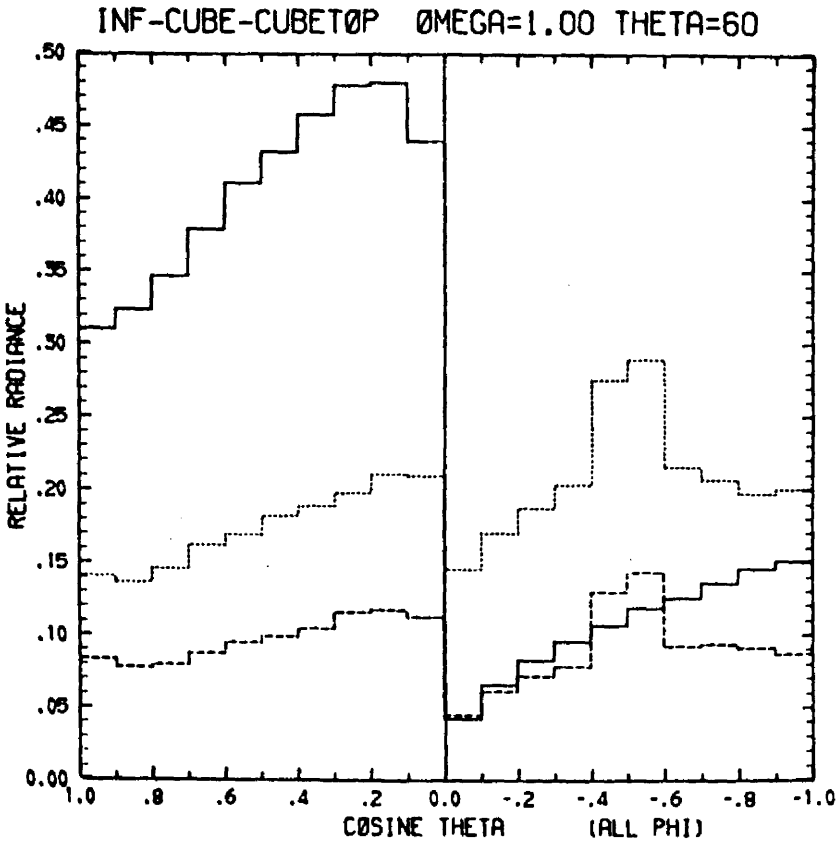

Figure 29. Same as figure 25 except $\theta_o = 60^o$

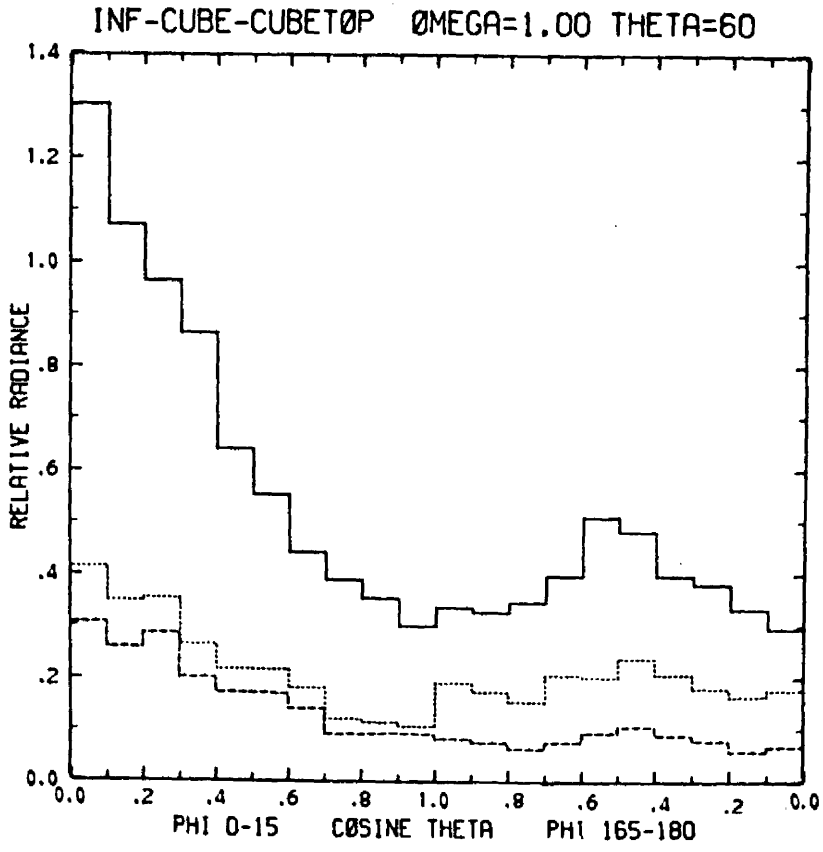

Figure 30. Same as figure 26 except $\theta_o = 60^o$.

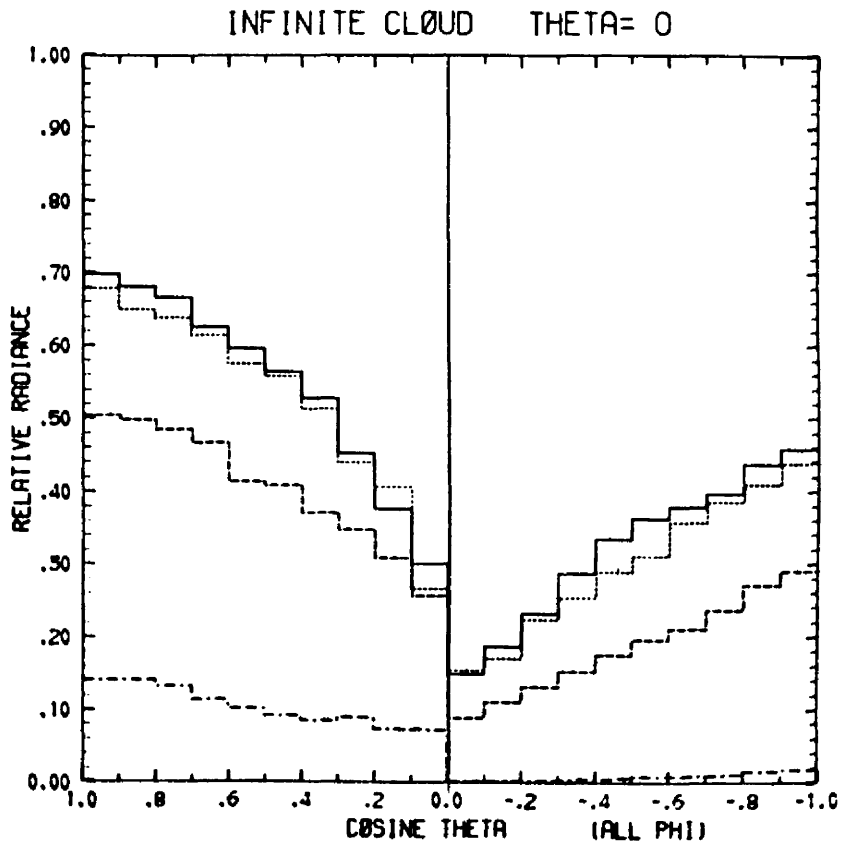

Figure 31. Upward and downward radiance (all ϕ) vs. cosine theta for $\theta_0 = 0^0$, τ=20, ($\bar{\omega}_0$= 1.0 ———, 0.999 ·····, 0.99 ------, 0.9 -·-·-)

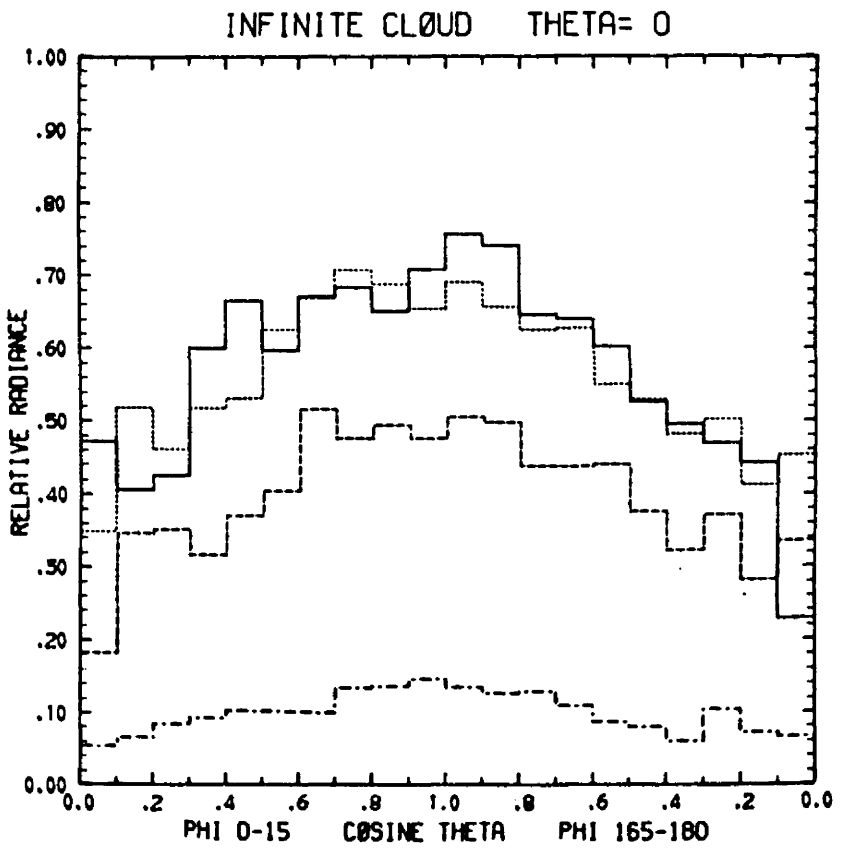

Figure 32. Upward relative radiance vs. cosine theta for $\theta_0 = 0^0$, τ=20 ($\bar{\omega}_0$= 1.0 ———, 0.999 ·····, 0.99 -----, 0.9 -·-·-)

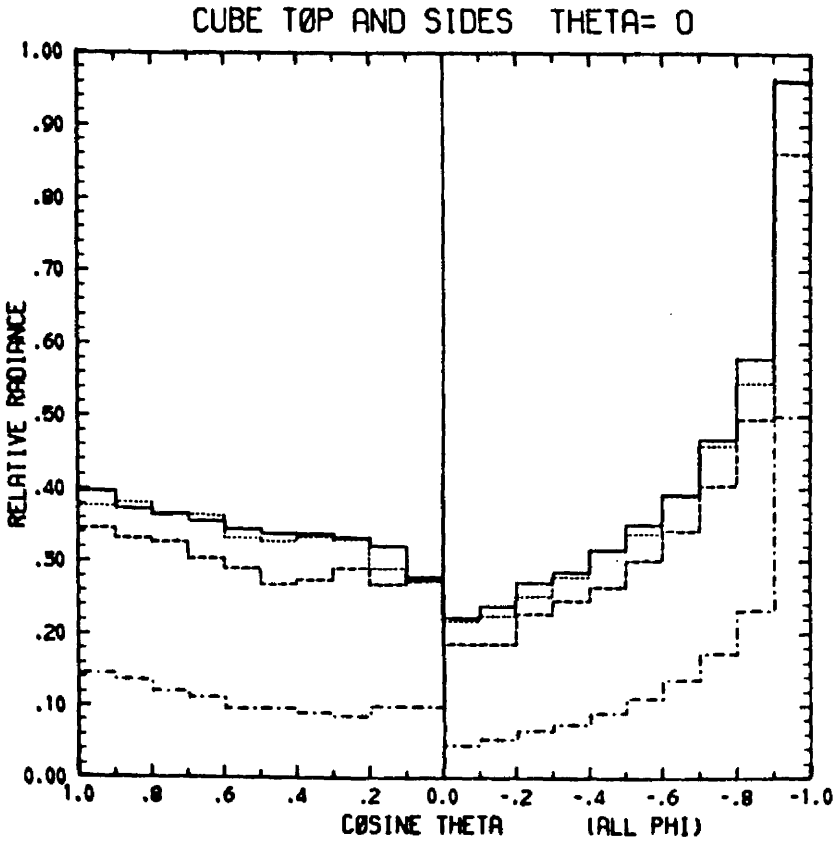

Figure 33. Same as figure 31 but for finite cloud.

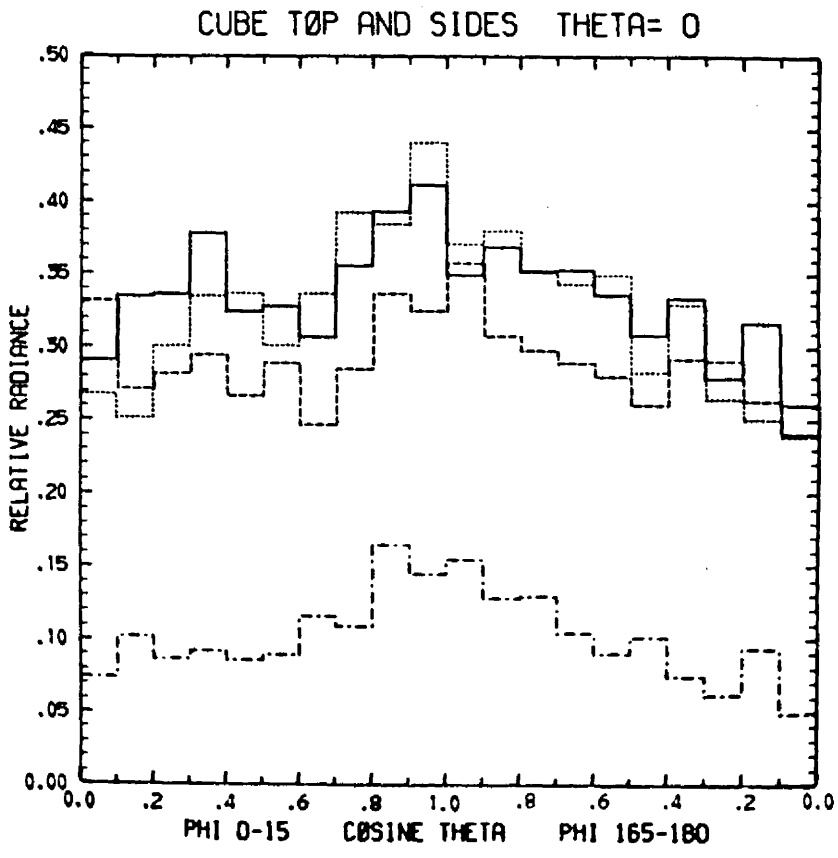

Figure 34. Same as figure 32 but for finite cloud.

the dashed line representing $\bar{\omega}_0 = 0.99$, and the dash-dot combination representing $\bar{\omega}_0 = 0.9$.

The relative radiance from the infinite cloud at $\bar{\omega}_0 = 0.999$ is in general reduced only 1-6% from the conservative values in the upward direction for all ϕ (figure 31). The reductions in relative radiance in the total cube appear smaller than those of the infinite cloud. At $\bar{\omega}_0 = 0.999$ the fractional absorption is about 4% for the infinite cloud and about 1.5% for the finite cloud at $\tau = 20$ (Tables 4 and 5). In the upward hemisphere scan graphs (figures 32 and 34) the reductions in radiance values from the conservative case are small and within the Monte Carlo noise at $\bar{\omega}_0 = 0.999$.

At $\bar{\omega}_0 = 0.99$ the reductions in relative radiance become more apparent especially in the infinite cloud with reductions up to 30% in the upward direction and 48% in the downward direction for all ϕ at $\theta_0 = 0^0$ The cubic cloud shows smaller reductions in relative radiance, about 15% in the upward direction and about 13% in the downward direction. At $\bar{\omega}_0 = 0.9$ about 80% of the incident photons are absorbed in the infinite cloud and about 60% in the cubic cloud (Tables 4 and 5). Figure 31 illustrates that the infinite cloud experiences a reduction from the conservative case of about 70-80%. Almost no light exits the bottom of the infinite cloud with $\bar{\omega}_0 = 0.9$. The cubic cloud (figure 33) experiences about a 65-70% reduction. The downward radiance shows a reduction of 50-80% with a significant amount still able to exit the cloud. The scan from -Y to +Y (figures 32 and 34) show reductions from conservative values of about 80% for the infinite cloud and about 60-80% for the cubic cloud.

Figures 35 to 38 show the effects of solar angle changes in a strongly absorbing case ($\bar{\omega}_0 = 0.9$). The solid line represents $\theta_0 = 0^o$, the dotted line represents $\theta_0 = 30^o$ and the dashed line represents $\theta_0 = 60^o$. At 60^o both the infinite cloud (figure 35) and the cubic cloud (figure 37) show smaller reductions from the conservative case than at 0^o or 30^o. A complete set of graphs for all the solar angles and all single scattering albedo values used are contained in Appendix A.

A study of the graphs presented indicate that the shape of a radiance pattern is detemined primarily by the cloud shape geometries and the solar zenith angle. Absorption tends to decrease the values of the relative radiance without drastically changing the shape of the radiance patterns. Absorption tends to slightly flatten out the patterns by reducing the directly upward values more than the horizontal values. Photons need to be turned through scattering a larger angle to exit the cloud directly upward than to exit near horizontal. The amount of absorption in this model increases with the number of scatter encounters. The infinite cloud demonstrates a greater reduction in radiance values at a given single scattering albedo than a cubic cloud, for the reason just stated. With absorption the infinite cloud shows a greater reduction in relative radiance values in the downward direction than in the upward direction. The cubic cloud shows slightly less reductions downward than upward. Photons are able to escape out the sides of a cubic cloud heading downward after only a few scatters and not be absorbed.

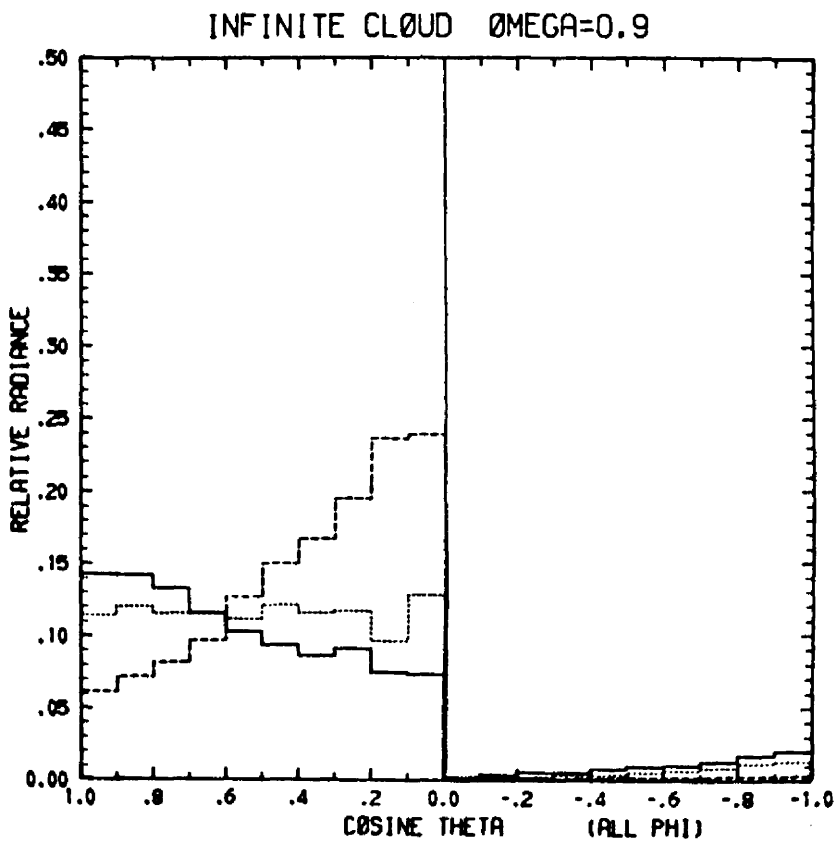

Figure 35. Upward and downward radiance (all ϕ) vs. cosine theta for the infinite cloud τ=20, $\bar{\omega}_0$ = 0.9 (θ_0= 0^0 ———, 30^0 ·····, 60^0 ------)

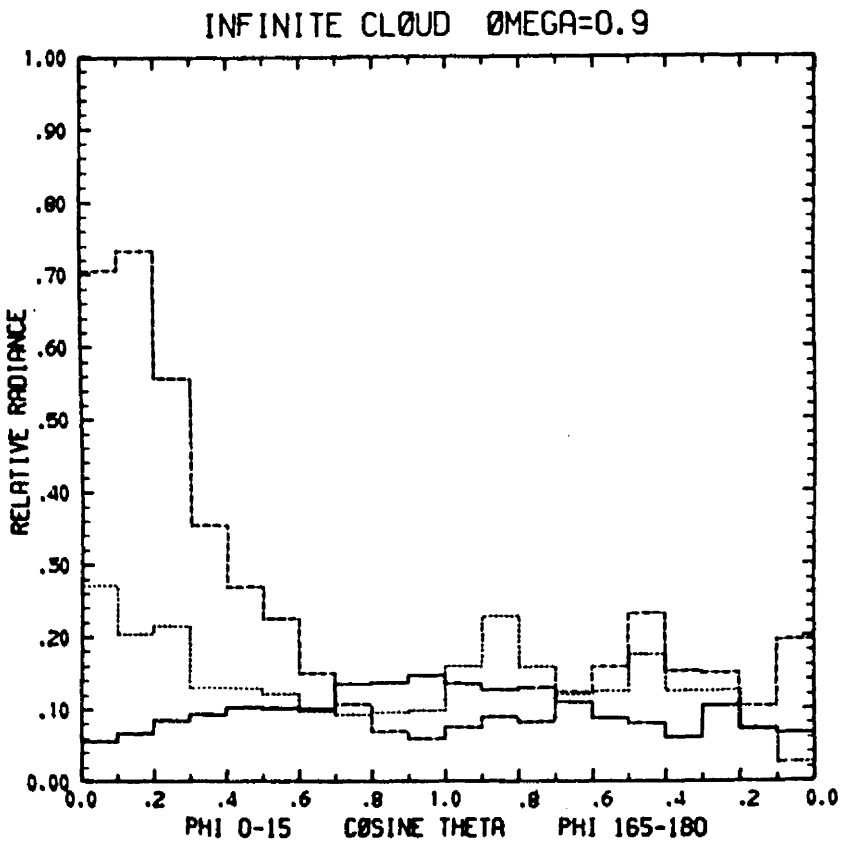

Figure 36. Upward relative radiance vs. cosine theta for the infinite cloud τ=20, $\bar{\omega}_0$= 0.9 (θ_0=0^0 ———, 30^0 ·····, 60^0 ------)

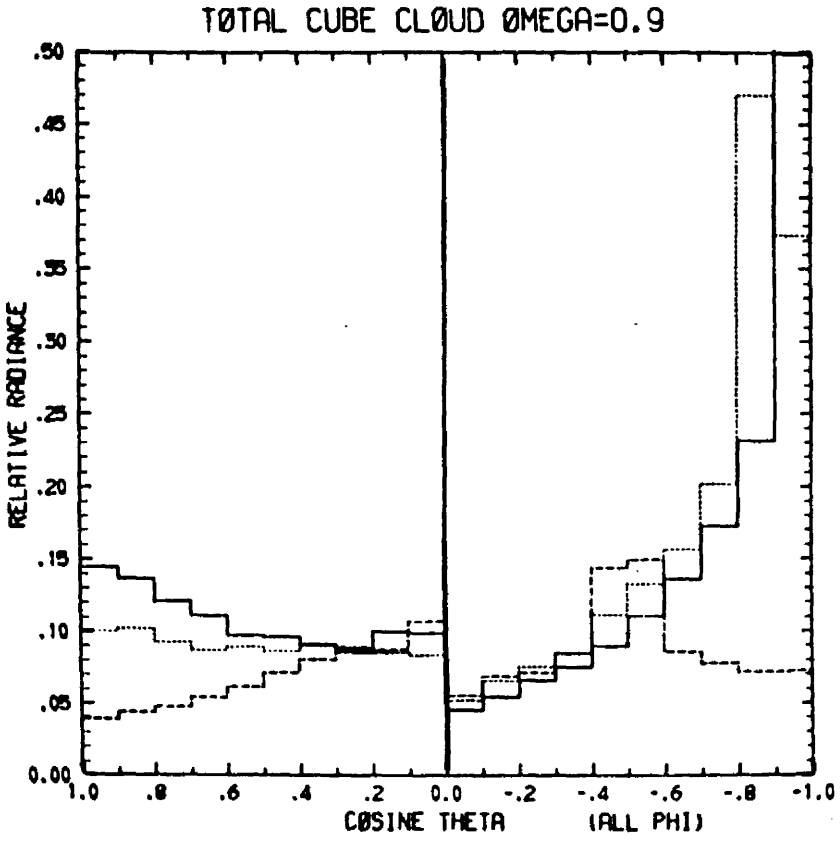

Figure 37. Same as figure 35 but for the finite cloud.

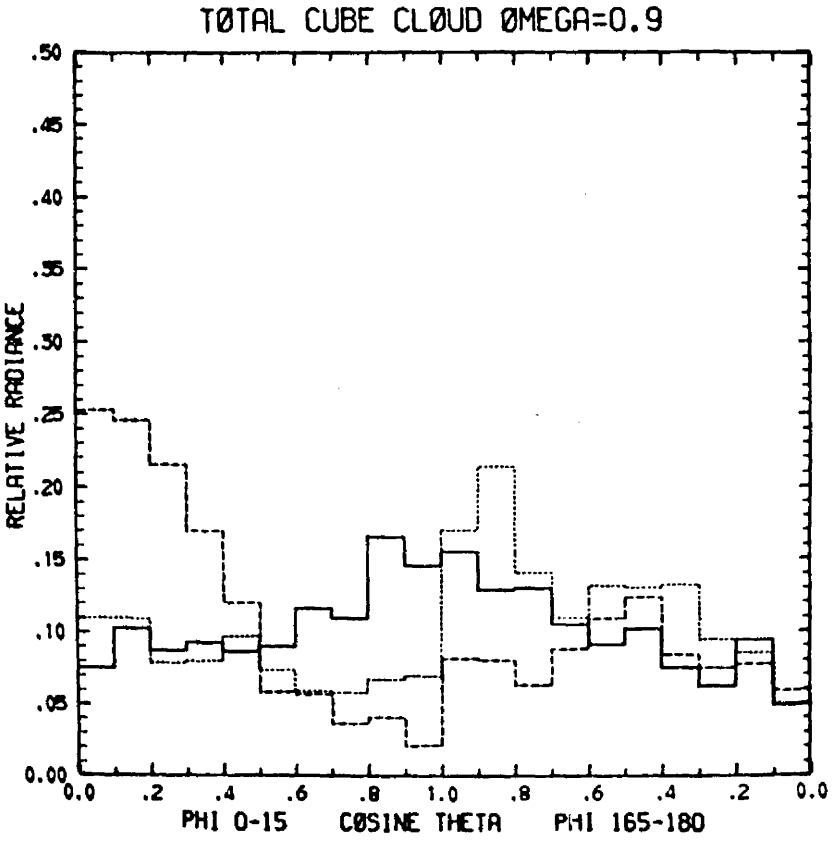

Figure 38. Same as figure 36 but for the finite cloud.

Increasing the optical depth from 20 to 60 produces a large increase in the total number of scattering events with a resulting increase in running time. Figures 39 to 46 are for $\tau = 60$, $\theta_o = 0°$. Figures 39 and 40 illustrate the conservative case for the infinite cloud, total cube cloud and cube top or bottom alone. The infinite cloud at $\tau = 60$ shows about a 30% increase in upward radiance values (all ϕ) compared to $\tau = 20$ and a 60-70% decrease in downward radiance values. The shape of the radiance pattern in the upward direction remains about the same but in the downward direction the pattern is flatter at $\tau = 60$ than at $\tau = 20$. The total cubic cloud shows an increase of 25-55% in the upward direction with a steepened shape from $\tau = 20$ to $\tau = 60$. In the downward direction the total cube shows an 18-60% decrease with a flattened shape from $\tau = 20$ to $\tau = 60$. With an increased optical thickness photons that might have escaped downward out the sides of the cube with only a few scatters at $\tau = 20$, have more scatters and apparently exit going upwards. The large spike downward off the sides of the cube is considerably reduced at $\tau = 60$. The cube top and bottom alone behave in a manner analagous to the infinite cloud with very little light exiting the bottom of either cloud. In Figure 40 both the infinite cloud and the total cube show increases in relative radiance from $\tau = 20$ to $\tau = 60$ of about 30-60%. With increased optical depth photons have more scatters and are able to be turned around and exit upwards. Fewer photons reach the middle and lower layers with the sun vertical.

With absorption added to a thickened cloud the increased number of scatters causes more absorption than at a smaller optical depth. However the increased number of scatters also causes less light to exit

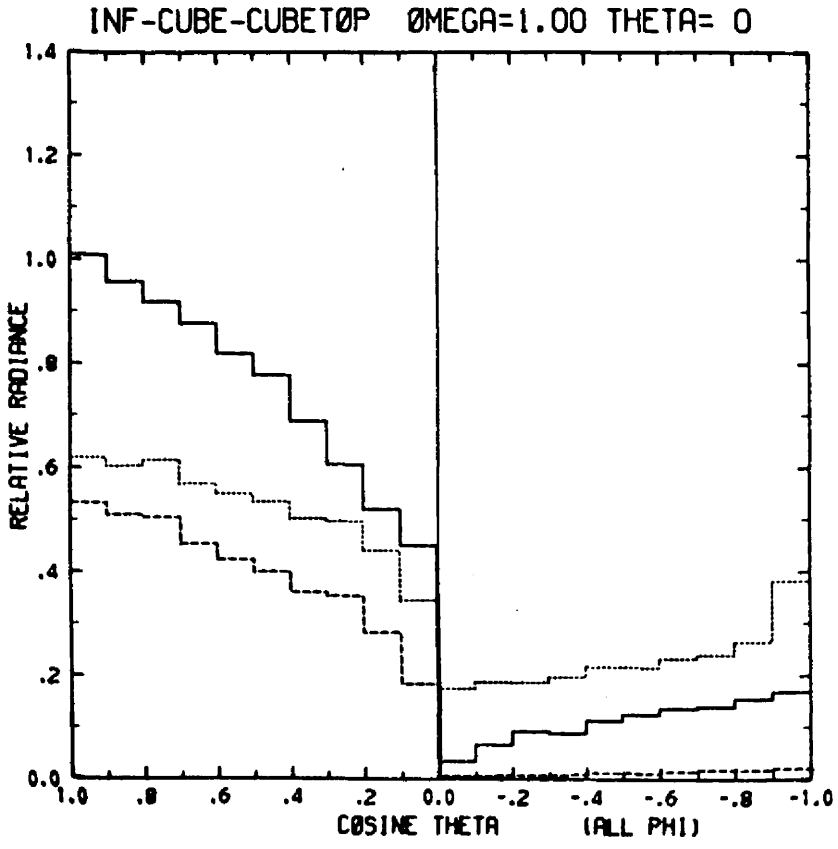

Figure 39. Same as figure 25 but for τ= 60.

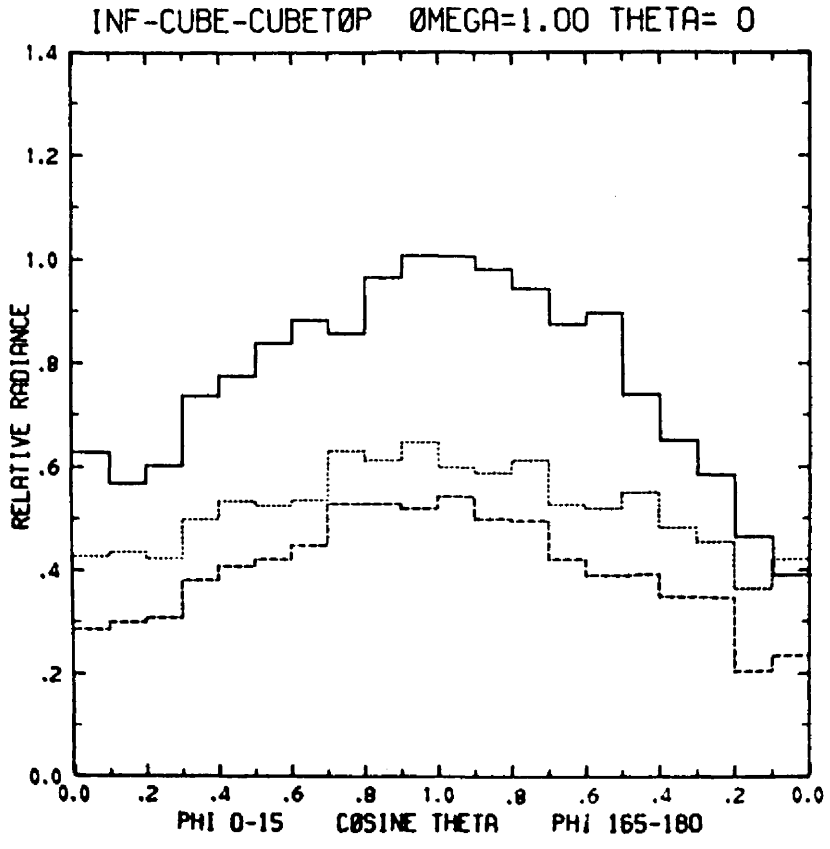

Figure 40. Same as figure 26 but for τ=60.

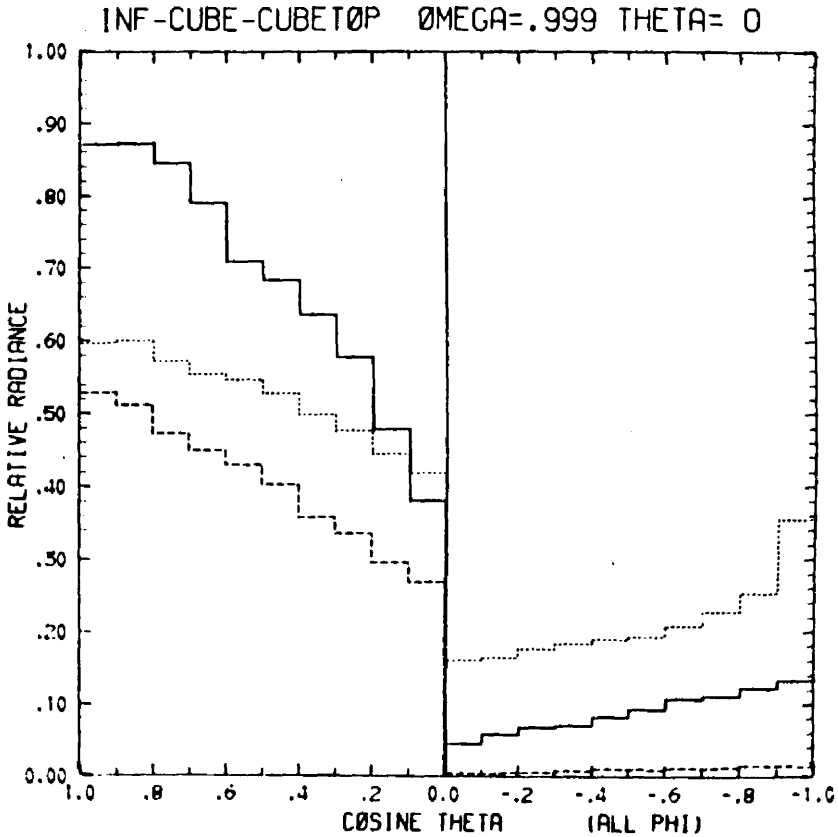

Figure 41. Same as figure 25 but $\bar{\omega}_0$ = 0.999, τ = 60.

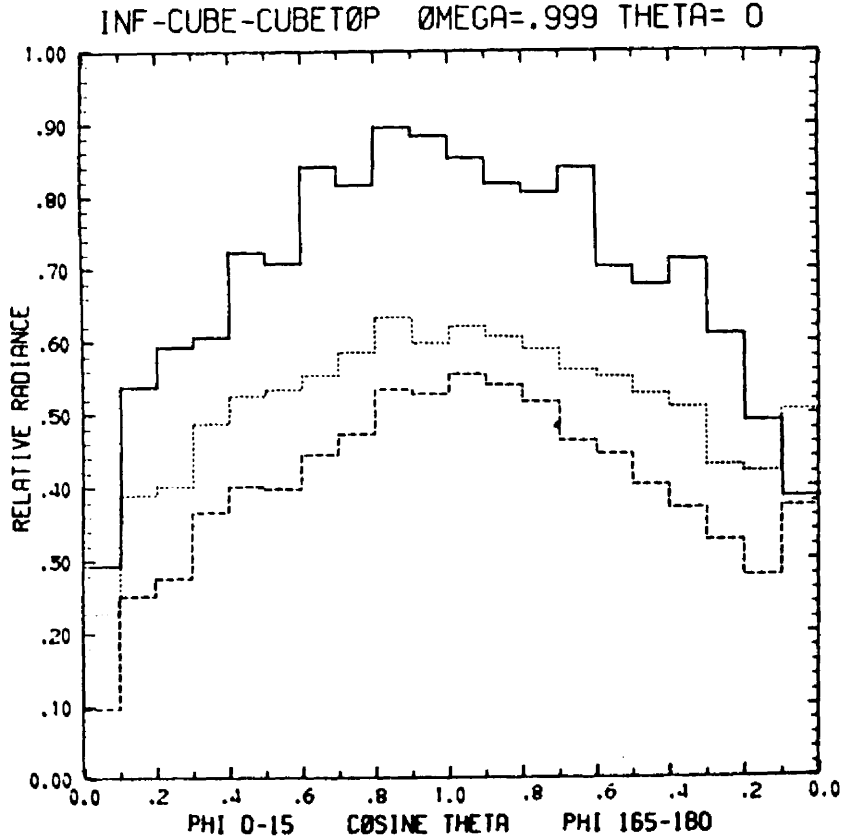

Figure 42. Same as figure 26 but $\bar{\omega}_0$ = 0.999, τ = 60.

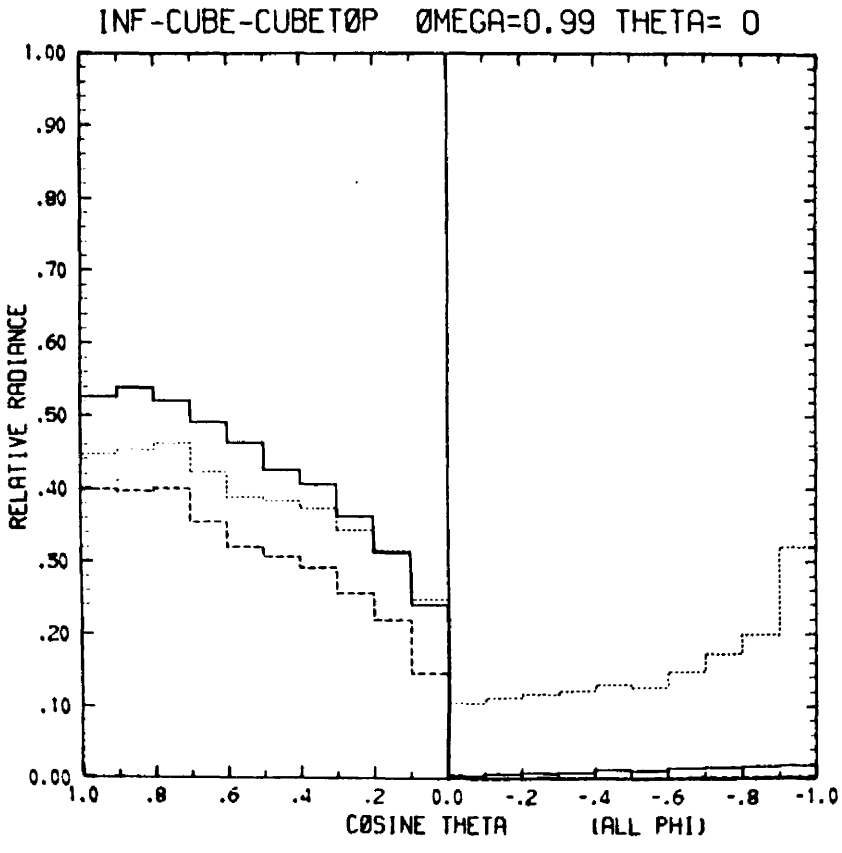

Figure 43. Same as figure 25 but $\bar{\omega}_0$ = 0.99, τ = 60.

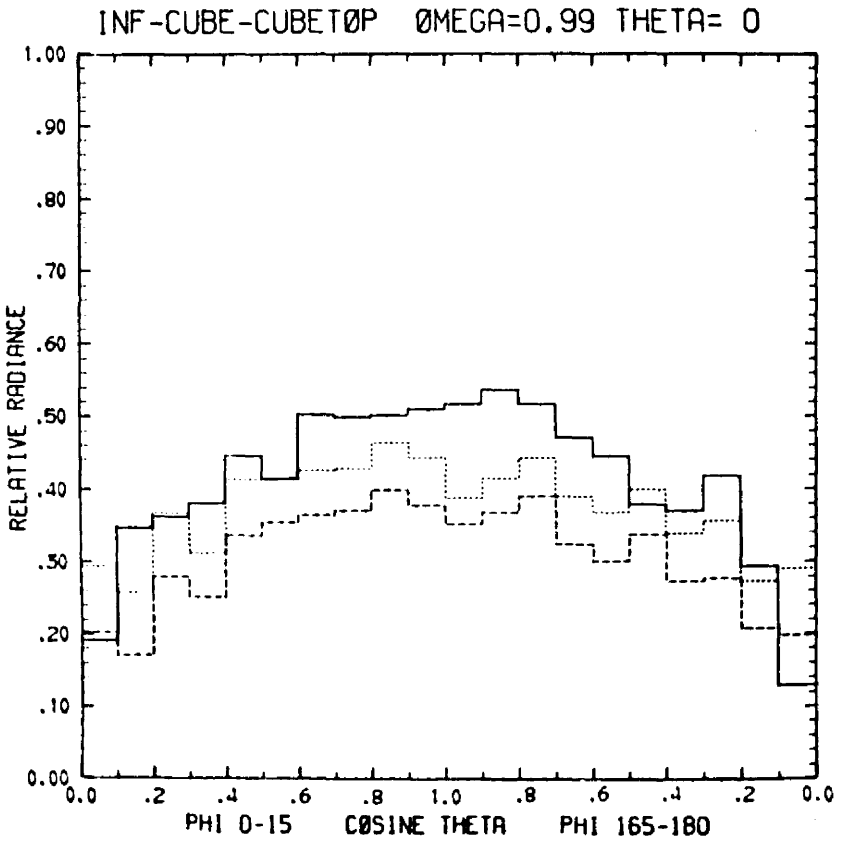

Figure 44. Same as figure 26 but $\bar{\omega}_0$ = 0.99, τ = 60.

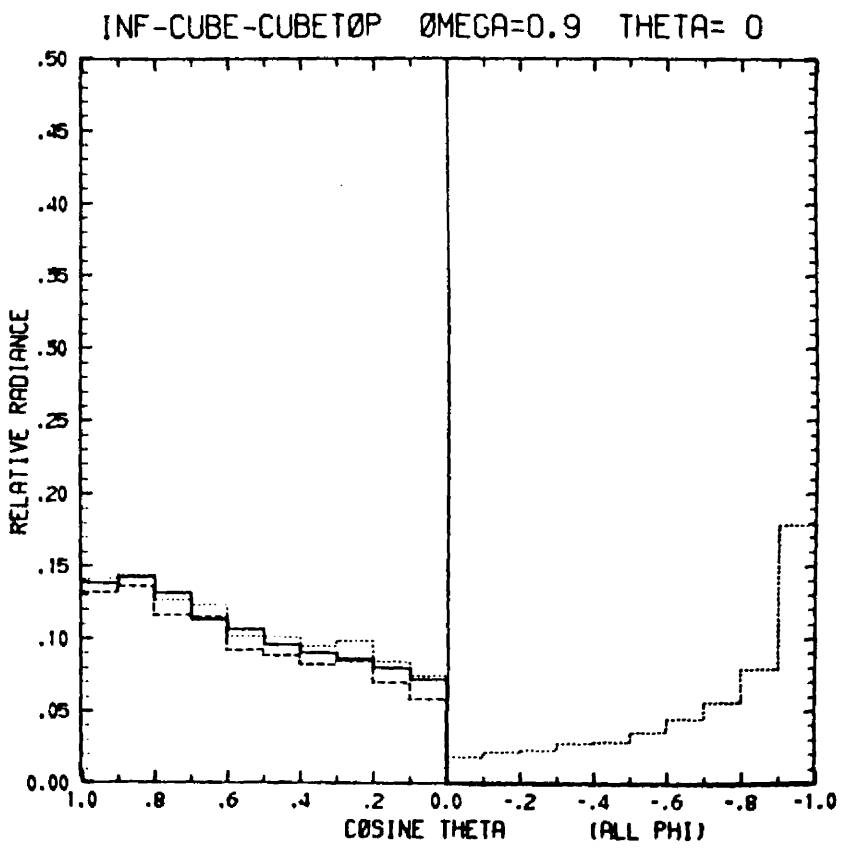

Figure 45. Same as figure 25 but $\bar{\omega}_0$ = 0.9, τ = 60.

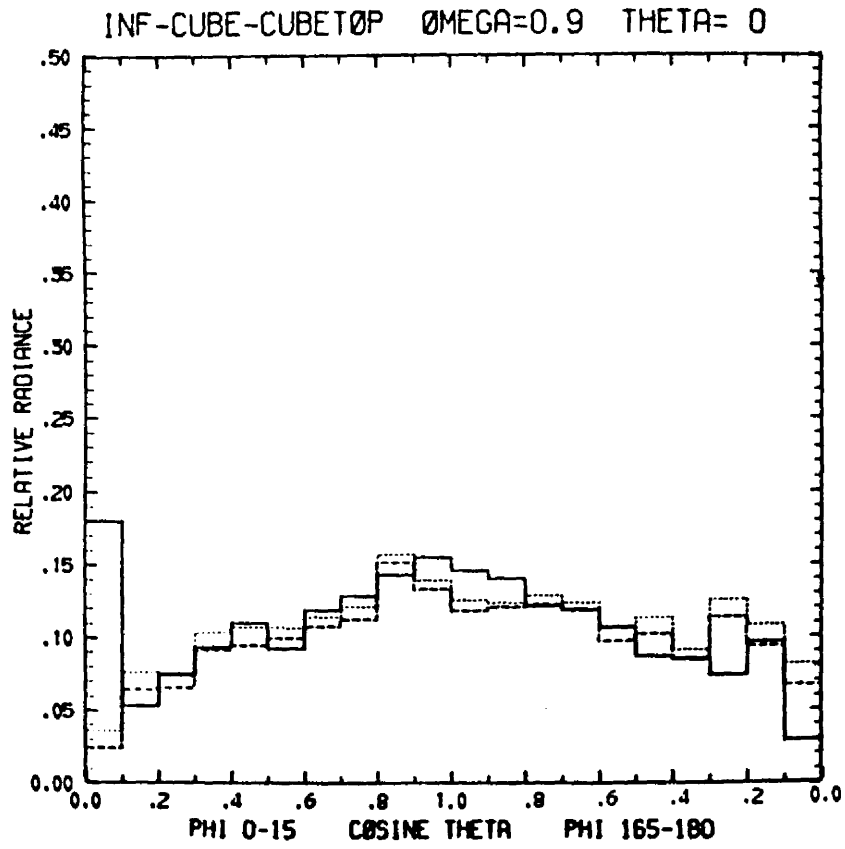

Figure 46. Same as figure 26 but $\bar{\omega}_0$ = 0.9, τ = 60.

downward and causes a higher directional reflectance. If absorption becomes large it will dominate and cause the cloud to be quite dark regardless of its optical depth.

Figures 41 and 42 show the results of $\tau = 60$, $\theta_0 = 0^0$, $\bar{\omega}_0 = .999$ for the infinite, cube and cube top or bottom. Figure 41 indicates that the infinite cloud shows an increase in the upward radiance values of about 30% and a decrease of about 70% in the downward radiance values when the optical depth is increased from $\tau = 20$ to $\tau = 60$. The reductions from the conservative case are about 15% in the upward direction and a 0-30% reduction in the downward direction at $\tau = 60$. These reductions are larger than similar reductions at $\tau = 20$ indicating that absorptive effects increase with increasing optical depths. The cubic cloud shows increases of about 35% in the upward direction and decreases ranging from 40-160% in the downward direction compared to values of a $\tau = 20$ cloud. Reductions from a conservative $\tau = 60$ cubic cloud to an $\bar{\omega}_0 = .999$ cubic cloud are about 3-17% decrease in the upward direction and 6-11% decrease in the downward direction.

Figure 42 indicates that the reductions in the ϕ box graph for the infinite cloud are about 10-20% from the conservative case.

Figures 43 and 44 illustrate $\bar{\omega}_0 = 0.99$ at $\theta_0 = 0^0$ for $\tau = 60$ clouds. As absorption increases in a thick cloud absorptive effects being to dominate over the effects of increased thickness, however, the effects of cloud shape can still be detected. Figure 43 shows that the infinite cloud is only slightly brighter in radiance values at $\tau = 60$ $\bar{\omega}_0 = .99$ than at $\tau = 20$. The cube and cube top however are brighter at $\tau = 60$ than at $\tau = 20$ in the upward direction. In the downward direction for all ϕ at $\tau = 60$ only the cube sides contribute a

significant amount. The straight down spike is still detectable but is reduced to about 60% of its corresponding $\tau = 20$ value. In Figure 44 the infinite cloud is about the same as its corresponding $\tau = 20$ values but the cube top and total cube show increases of about 40-50% above corresponding $\tau = 20$ values.

With increasing absorption, absorption effects totally dominate over increased optical thickness and cloud shape effects, except in the downward direction where the cube sides are still detectable. Figures 45 and 46 illustrate $\bar{\omega}_0 = .9$ for $\tau = 60$ clouds with the infinite cloud, cube top and total cube almost indistinguishable in the upward direction (Figures 45 and 46) with only the cube sides allowing light to exit downward (Figure 46).

Increasing the optical thickness of conservative clouds from $\tau = 20$ to $\tau = 60$ appears to increase the upward radiance from the cube more than the infinite and to decrease the downward radiance values from the infinite cloud more than the cubic cloud. Absorption with increased optical thickness reduces the upward radiance values but severely darkens the bottom of both clouds with the cube sides providing the majority of the downward radiance values.

IV. CONCLUSIONS

Results of Mie absorption upon shortwave irradiance values and radiance patterns of finite and infinite cloud models have been presented for a range of absorption and a range of solar zenith angles. In a finite cloud a smaller fraction of incident light is absorbed than in an infinite cloud. Both cloud types show a maximum fraction of absorption with the sun vertical. In an infinite cloud as the sun is tipped off the vertical the absorption decreases in the lower layers of the cloud, while in the finite cloud the lower layers increase in absorption as the sun is tipped. The infinite cloud shows an increasing directional reflectance and a corresponding decrease in downward irradiance as the solar zenith angle increases. The finite cloud shows a maximum directional reflectance and a minimum downward irradiance at $\theta_o = 0^o$.

The shapes of radiance patterns are determined primarily by cloud shape and sun angle geometry. Absorption tends to decrease and flatten the pattern but not significantly change the general shape of the radiance pattern. The infinite cloud shows a greater change in radiance patterns at each amount of absorption than the finite cloud. Reductions from the conservative radiance values are greater in the downward direction than in the upward direction for the infinite cloud but the reductions in the finite cloud are greater in the upward direction than for the downward direction. The reductions from conservative values to $\bar{\omega}_o = 0.9$ values are less at $\theta_o = 60^o$ than at 30^o or 0^o in both cloud models.

Increasing the optical depth from $\tau = 20$ to $\tau = 60$ with the sun vertical produces about a 25% increase in directional reflectance except at $\bar{\omega}_0 = 0.9$. The downward irradiance values decrease more for the infinite cloud than the finite cloud with increased optical depth. There is a larger increase in fractional absorption in the finite cloud than in the infinite. Increased optical depth results in increased upward radiance and decreased downward radiance in both cloud models at each absorption amount. The upward radiance patterns keep about the same shape with increased optical depth but the downward spike of light from the cube sides is reduced with increased optical depth but is still evident even at $\bar{\omega}_0 = 0.9$.

Although the finite cloud has been shown to fractionally absorb less than an infinite cloud, a finite cloud has a greater number of photons incident at non-zero solar zenith angles than an equal volume of infinite cloud. Hence a finite cloud may have total absorptions greater than an equal volume of infinite cloud at large solar zenith angles and small single scattering albedoes.

REFERENCES

Busygin, V. P., N. A. Yevstratov and Ye. M. Feygel'son, 1973: Optical properties of cumulus and radiant fluxes for cumulus cloud cover. Atmos. Oceanic Phys., 9, 1142-1151.

Cashwell, E. D., and C. J. Everett, 1959: A Practical Manual on the Monte Carlo Method for Random Walk Problems. Pergamon Press, 153 pp.

Danielson, R. E., D. R. Moore and H. C. Van de Hulst, 1969: The transfer of visible radiation through clouds. J. Atmos. Sci., 26, 1078-1087.

Deirmendjian, D., 1969: Electromagnetic Scattering on Spherical Polydispersions. American Elsevier, 290 pp.

International Association of Meteorology and Atmospheric Physics (I. U. G. G.), Radiation Commission, Standard Procedures to Compute Atmospheric Radiative Transfer in a Scattering Atmosphere, Numerical Comparisons of the Methods, 1976.

Kattawar, G. W., and G. N. Plass, 1971: Radiance and polarization of light reflected from optically thick clouds. Appl. Opt., 10, 74-80.

McKee, T. B., and S. K. Cox, 1974: Scattering of visible radiation by finite clouds. J. Atmos. Sci., 31, 1885-1892.

McKee, Thomas, and Stephen K. Cox, 1976: Simulated radiance patterns for finite cubic clouds. J. Atmos. Sci., 33, 2014-2020.

Twomey, S., 1972: The effect of cloud scattering on the absorption of solar radiation by atmospheric dust. J. Atmos. Sci., 29, 1156-1159.

Twomey, S., 1976: Computations of the absorption of solar radiation by clouds. J. Atmos. Sci., 33, 1087-1091.

APPENDIX A

Complete Set of Radiance Results

APPENDIX A

Complete Set of Radiance Results

Appendix A contains 60 graphs representing the complete set of radiance results for the cases studied. The graph on the left of each page represents the upward and downward radiance for all ϕ boxes, while the graph on the right represents a vertical scan form -Y to +Y in the first ϕ box.

Each of the first twelve pages is for a certain single scattering albedo and solar zenith angle at $\tau = 20$. Results shown for the infinite cloud (solid line), the total cubic finite cloud (dotted line), and the cube top only (dashed line).

The next eight pages are the same results but grouped in a different manner with the first four pages for the infinite cloud and the next four pages for the total cubic cloud. Each page is for a given value of the single scattering albedo with the results for $\theta_0 = 0^o$ (solid line), 30^o (dotted line), and 60^o (dashed line) being shown on each graph.

The next six pages contain the same data as presented but grouped by solar zenith angle, first for the infinite cloud then the finite cloud. Results are shown at the given solar zenith angle for the four values of the single scattering albedo: 1.0 (solid line), 0.999 (dotted line), 0.99 (dashed line), 0.9 (dashed-dot combination line).

The last four pages of graphs are for an increased optical depth ($\tau = 60$) but otherwise are identical to the first set of graphs presented for the infinite (solid line), total cube (dotted line), and the cube top only (dashed line).

LIST OF APPENDIX FIGURES

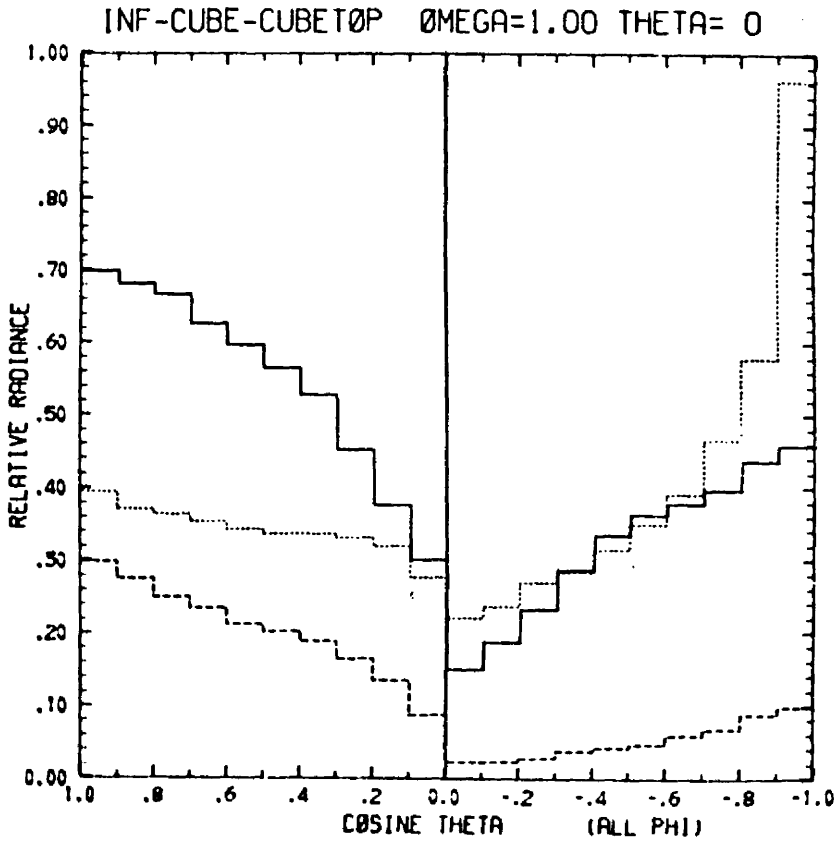

Figure A1. Upward and downward radiance (all ϕ) versus cosine θ, for $\tau = 20$, $\bar{\omega}_0 = 1.0$, $\theta_0 = 0^0$ (infinite ———, total cube ....., cube top ----) (same as Figure 25).

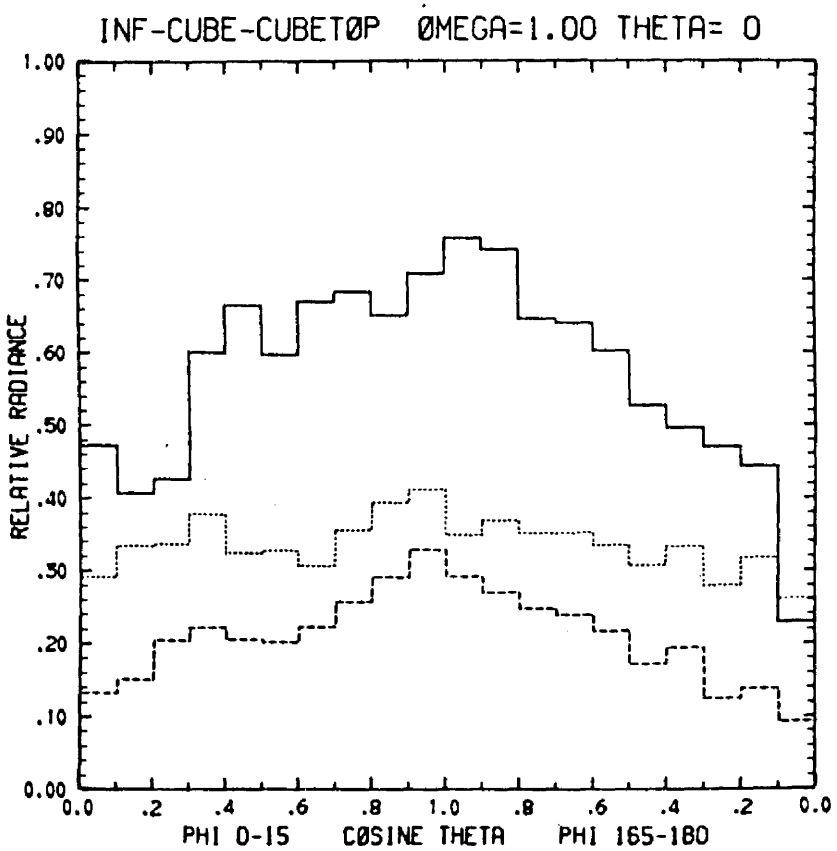

Figure A2. Upward radiance near the solar plane versus cosine θ, for $\tau = 20$, $\bar{\omega}_0 = 1.0$, $\theta_0 = 0^0$. (Infinite ———, total cube ...., cube top ----) (same as Figure 26).

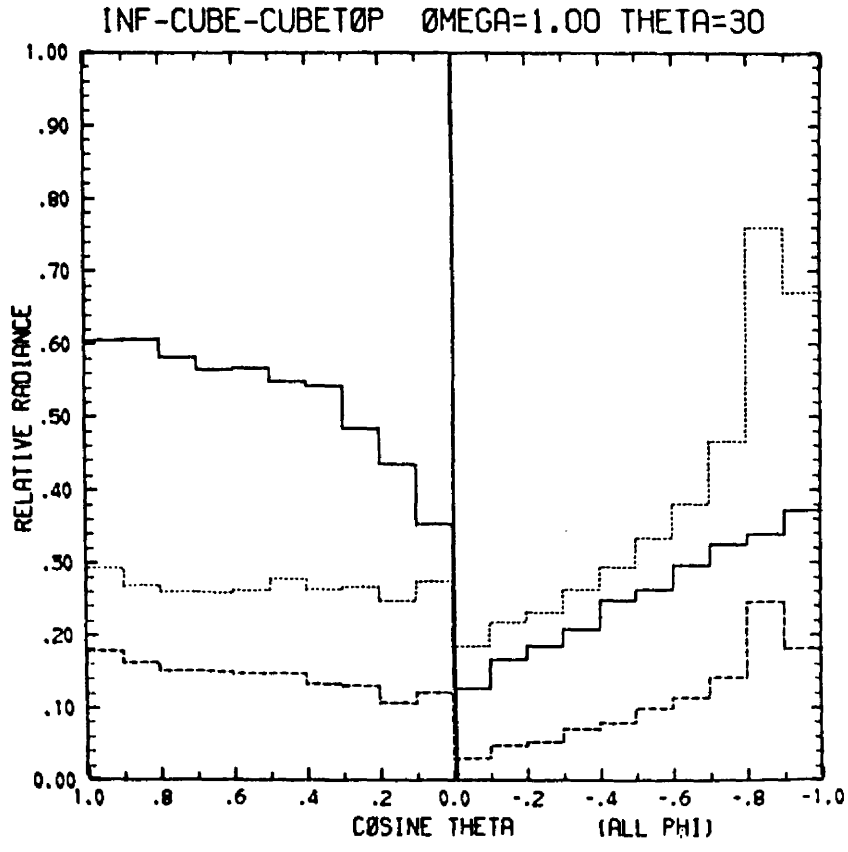

Figure A3. Same as Figure A1 except $\theta_o = 30^o$ (same as Figure 27).

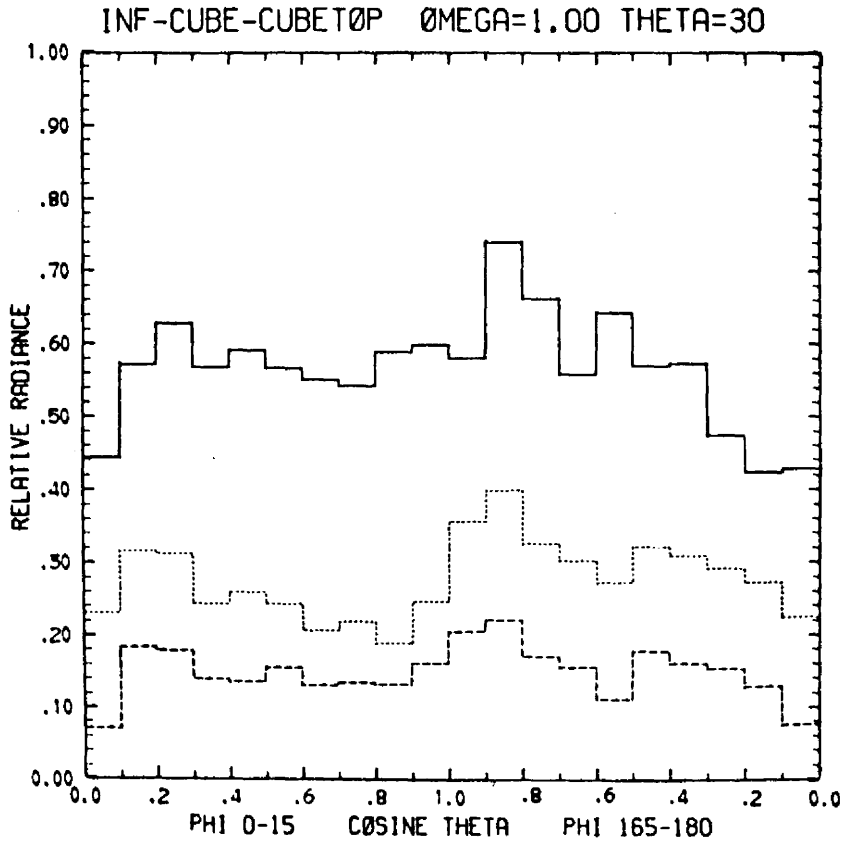

Figure A4. Same as Figure A2 except $\theta_o = 30^o$ (same as Figure 28).

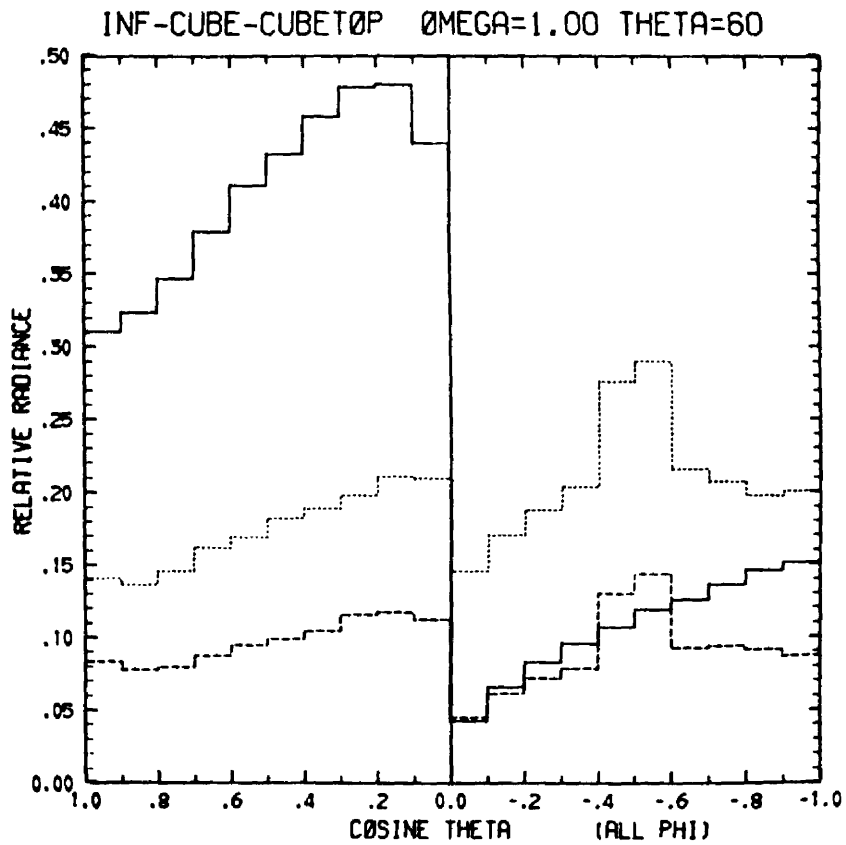

Figure A5. Same as Figure A1 except $\theta_o = 60^o$ (same as Figure 29).

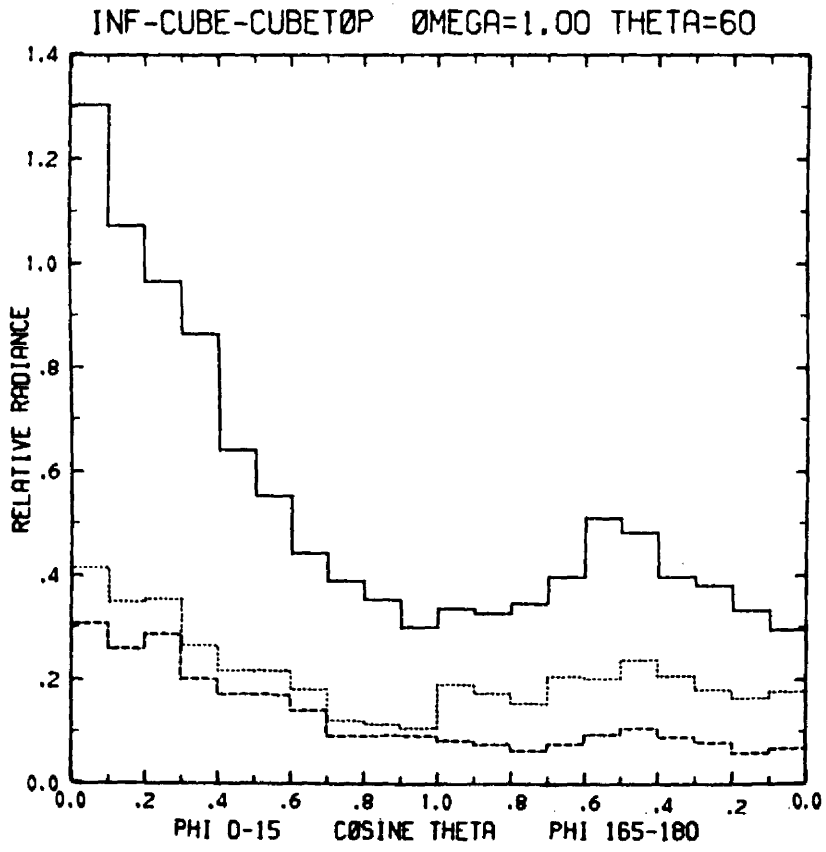

Figure A6. Same as Figure A2 except $\theta_o = 60^o$ (same as Figure 30).

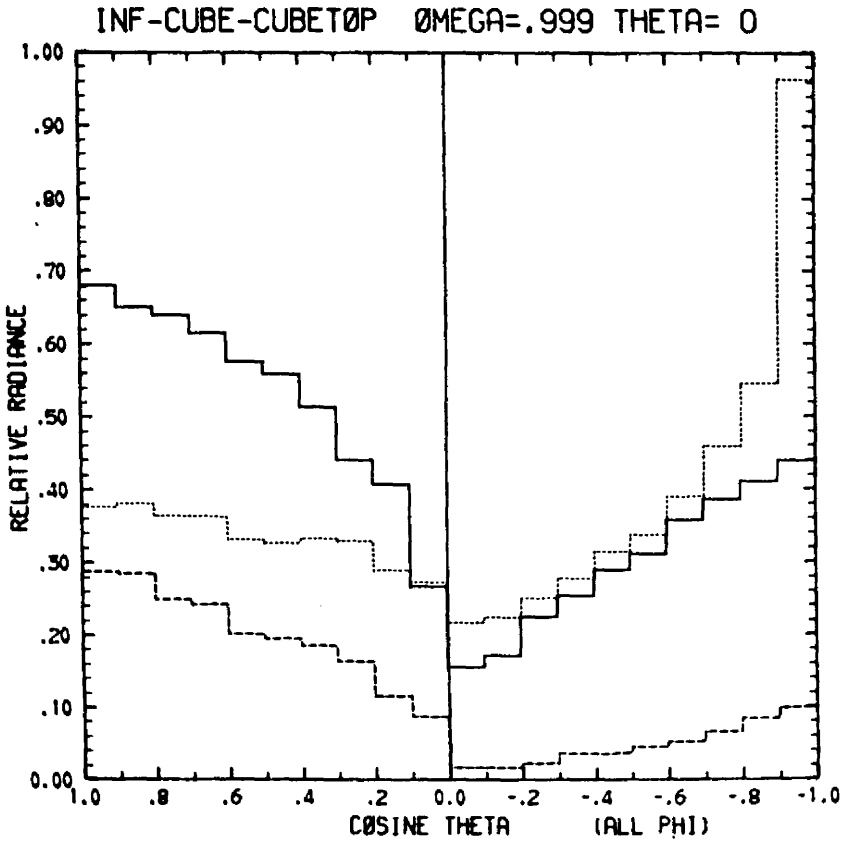

Figure A7. Same as Figure A1 except $\bar{\omega}_0$ = 0.999.

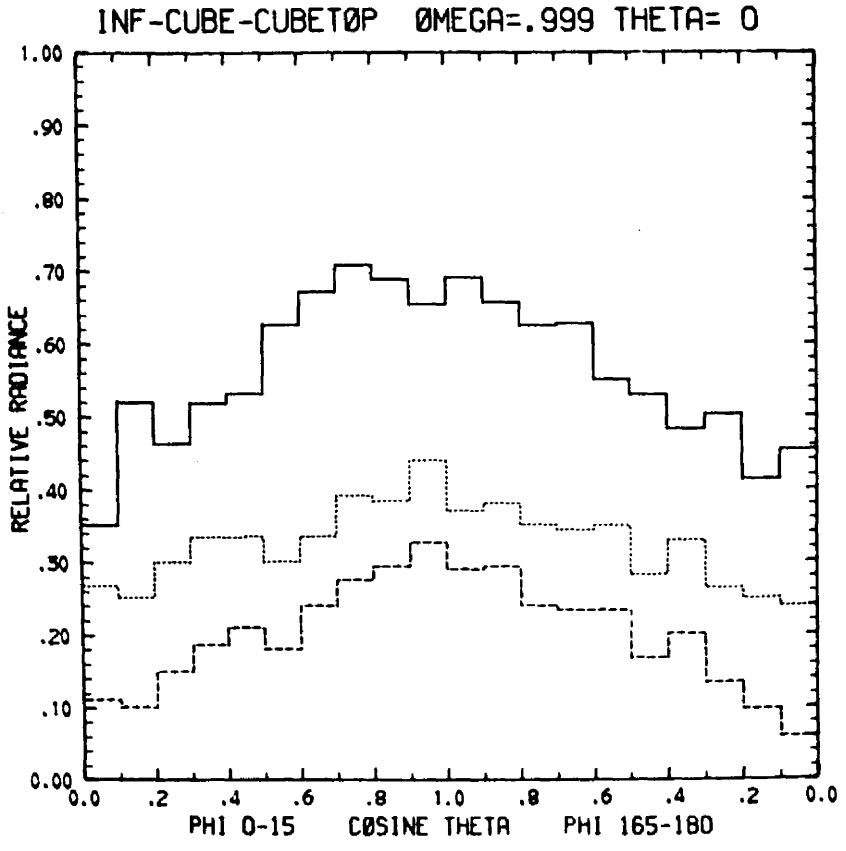

Figure A8. Same as Figure A2 except $\bar{\omega}_0$ = 0.999.

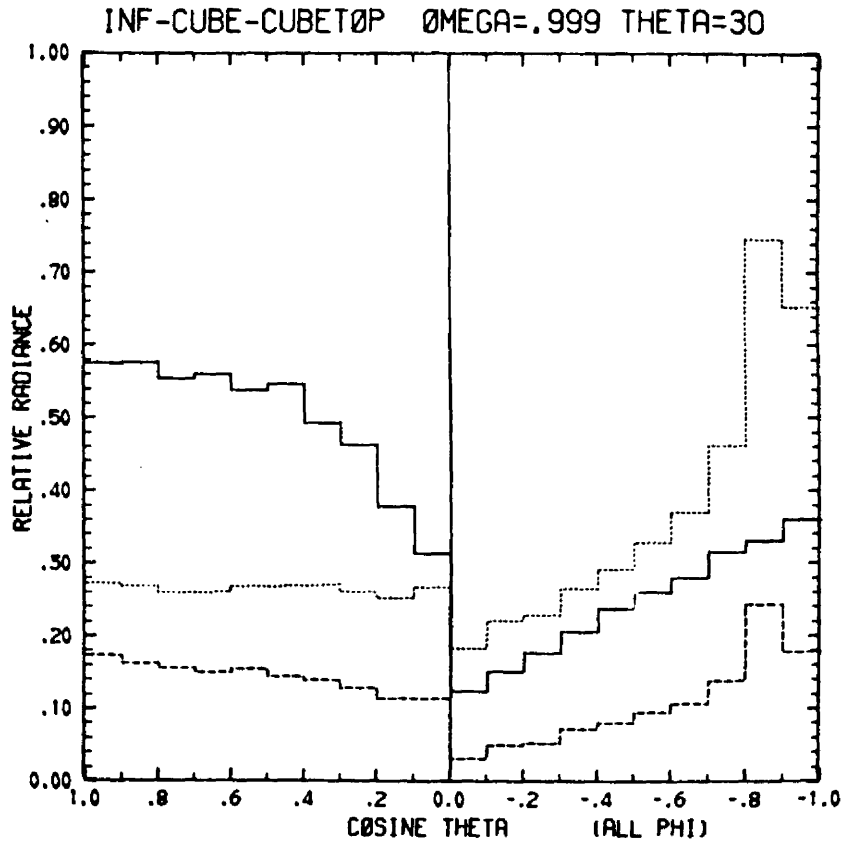

Figure A9. Same as Figure A1 except $\bar{\omega}_0$ = 0.999, $\theta_0 = 30^0$.

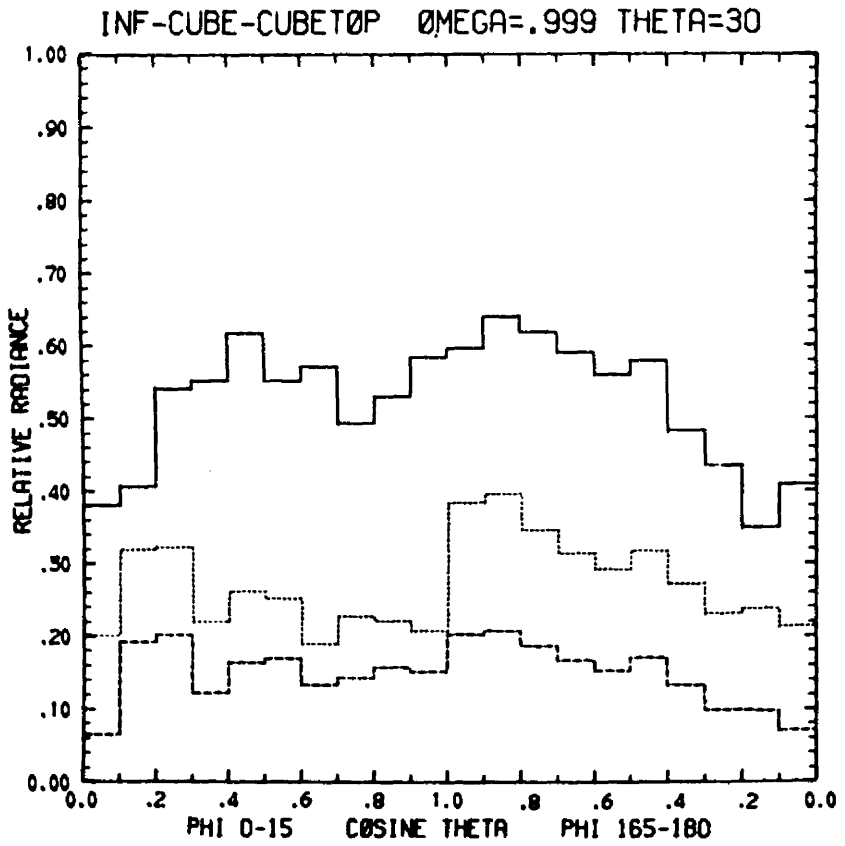

Figure A10. Same as Figure A2 except $\bar{\omega}_0$ = 0.999, $\theta_0 = 30^0$.

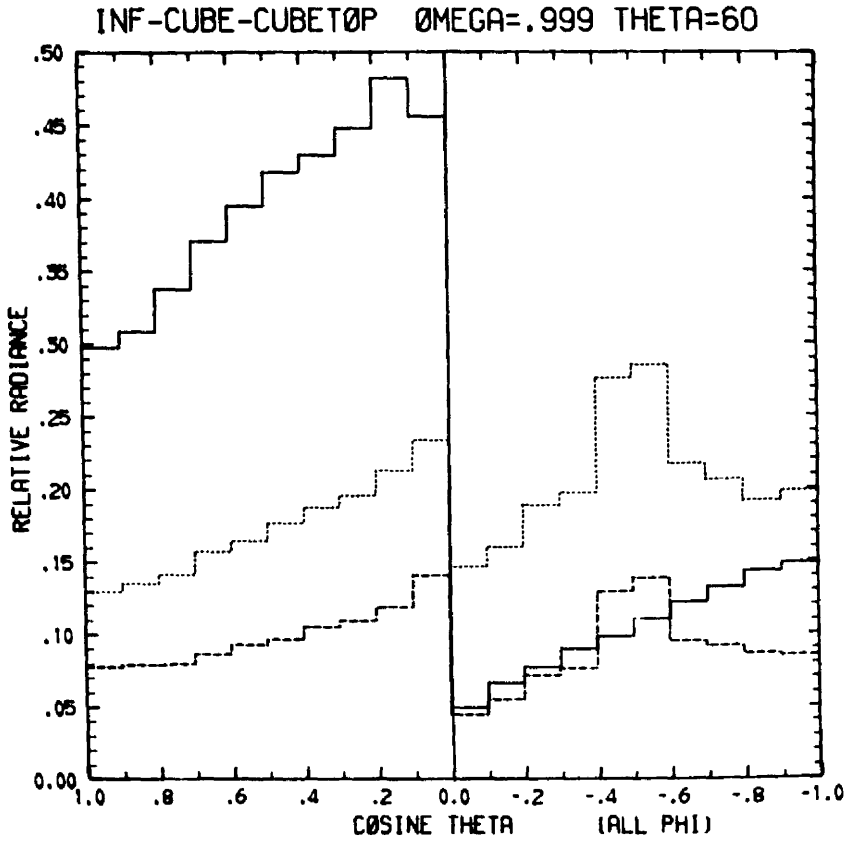

Figure A11. Same as Figure A1 except $\bar{\omega}_0$ = 0.999, $\theta_0 = 60^0$.

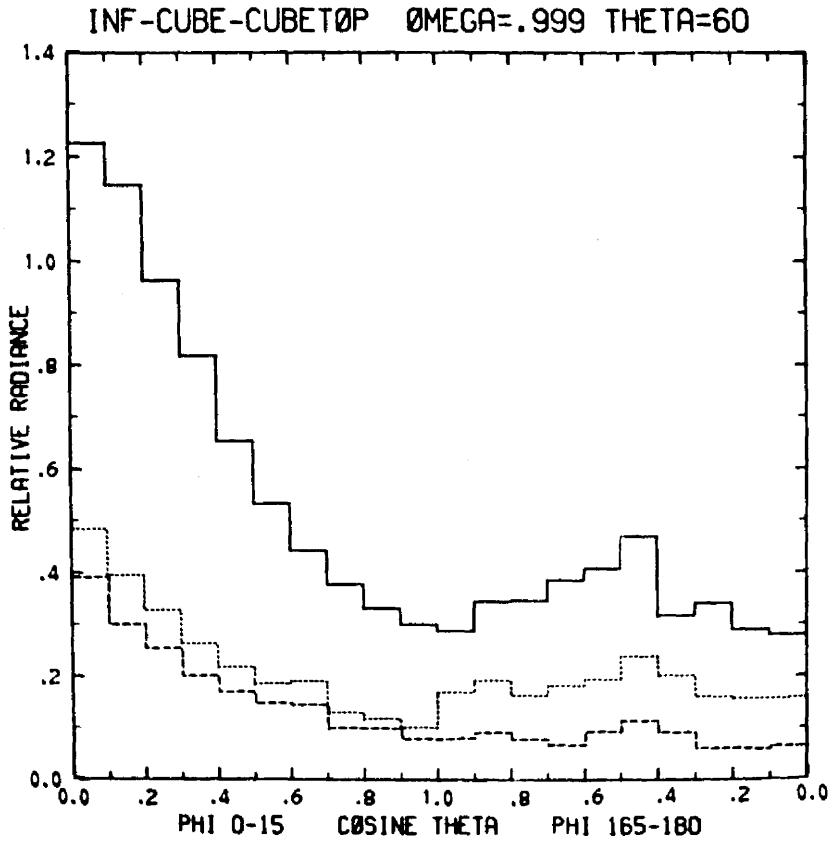

Figure A12. Same as Figure A2 except $\bar{\omega}_0$ = 0.999, $\theta_0 = 60^0$.

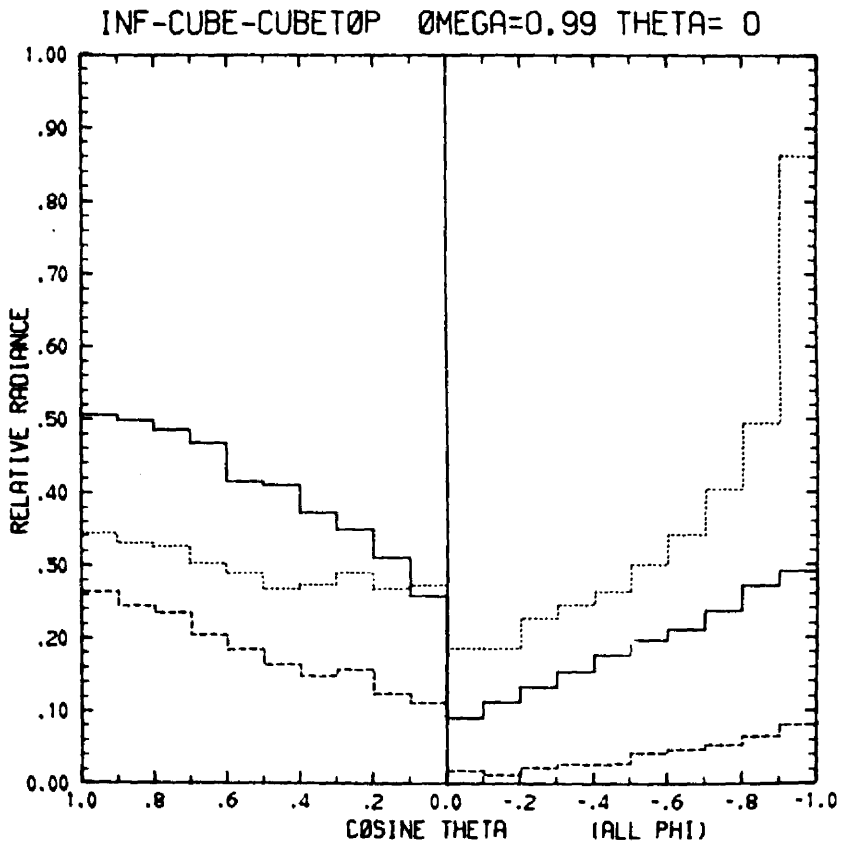

Figure A13. Same as Figure A1 except $\bar{\omega}_0$ = 0.99.

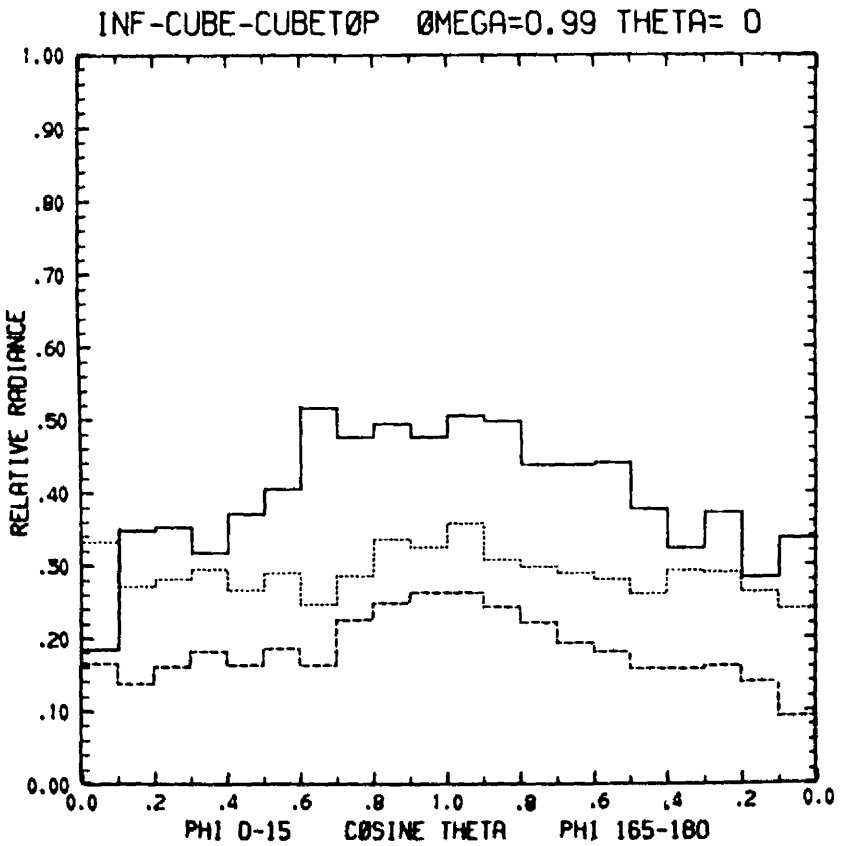

Figure A14. Same as Figure A2 except $\bar{\omega}_0$ = 0.99.

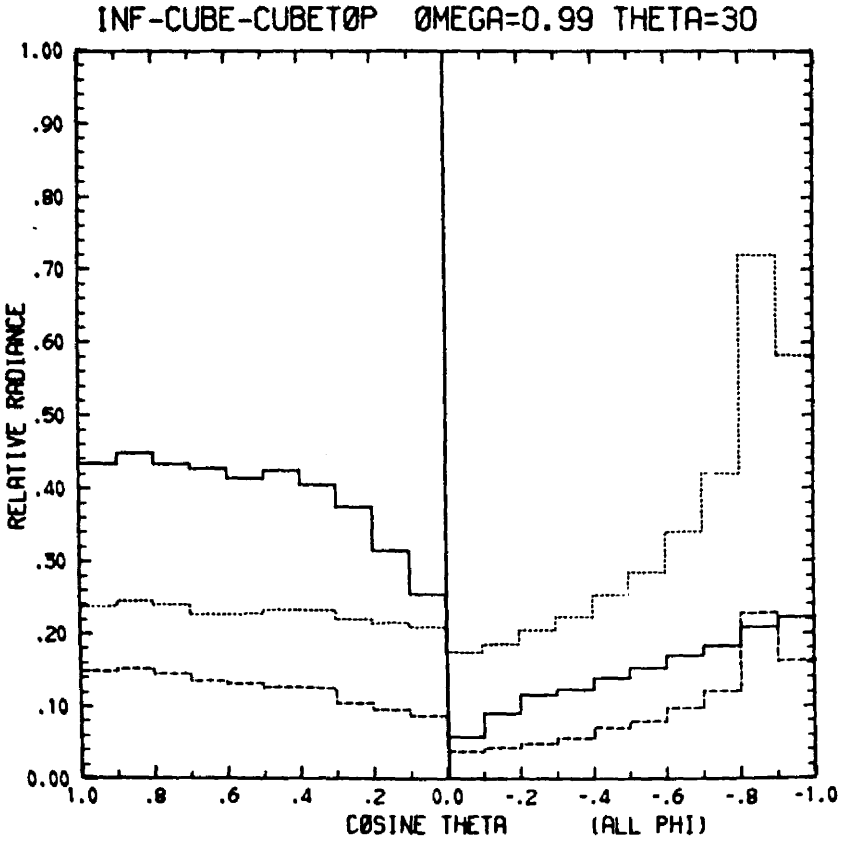

Figure A15. Same as Figure A1 except $\bar{\omega}_0 = 0.99$, $\theta_0 = 30^0$.

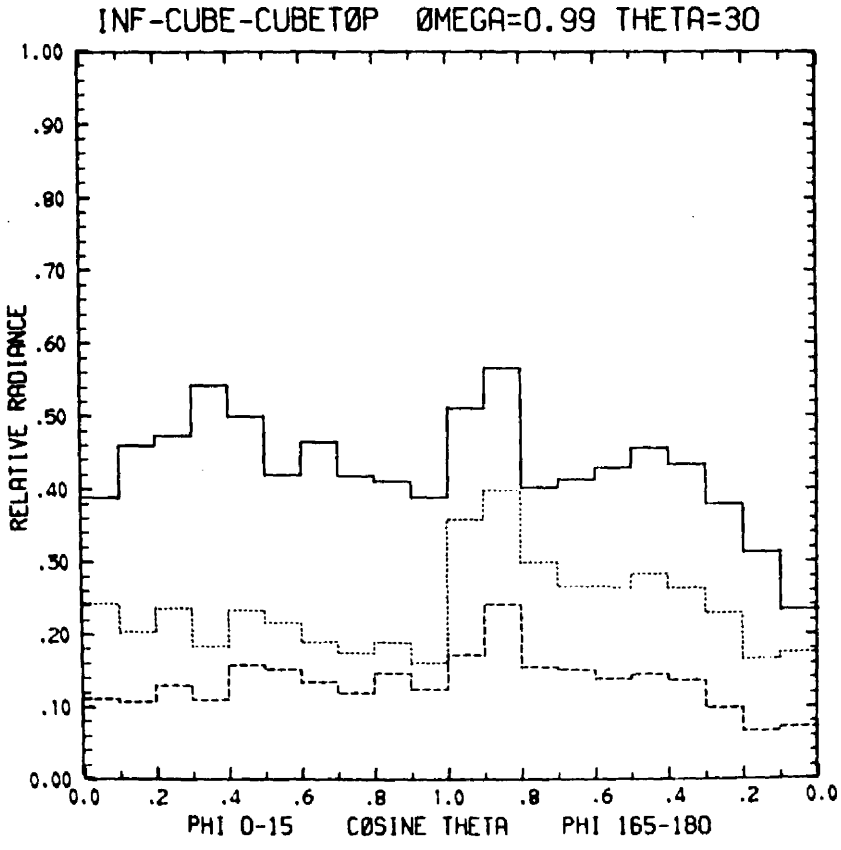

Figure A16. Same as Figure A2 except $\bar{\omega}_0 = 0.99$, $\theta_0 = 30^0$.

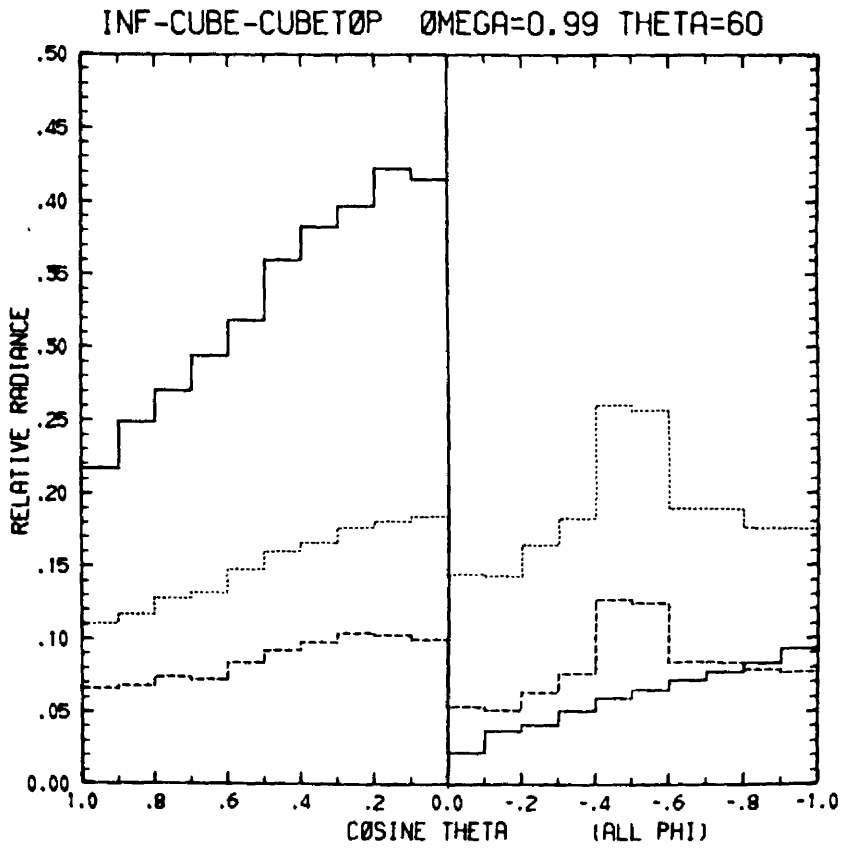

Figure A17. Same as Figure A1 except $\bar{\omega}_0 = 0.99$, $\theta_0 = 60^0$.

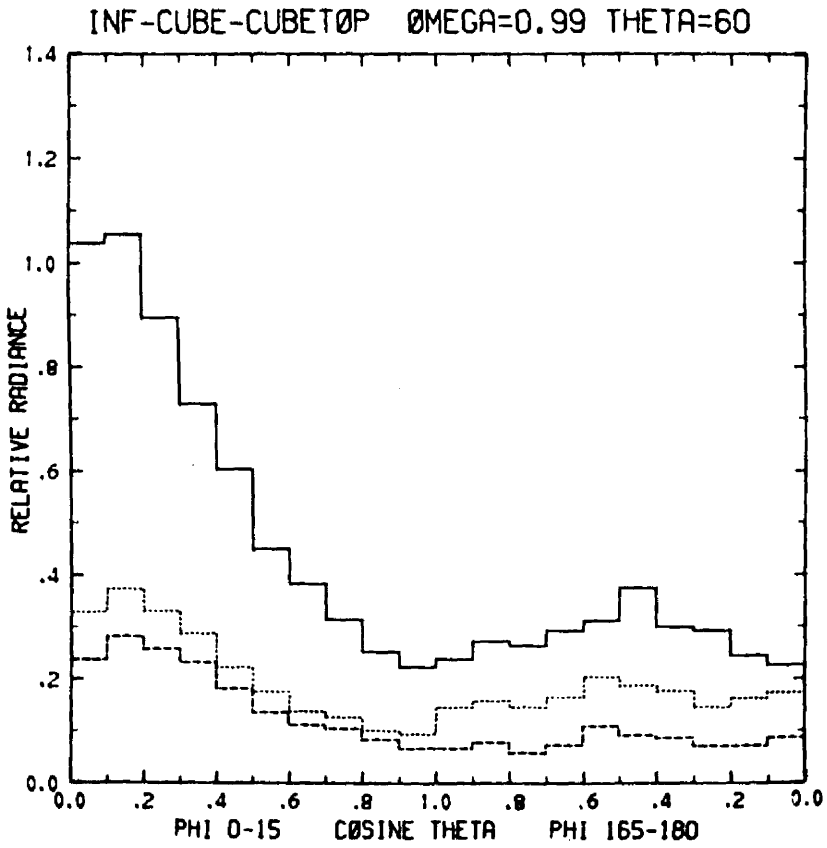

Figure A18. Same as Figure A2 except $\bar{\omega}_0 = 0.99$, $\theta_0 = 60^0$.

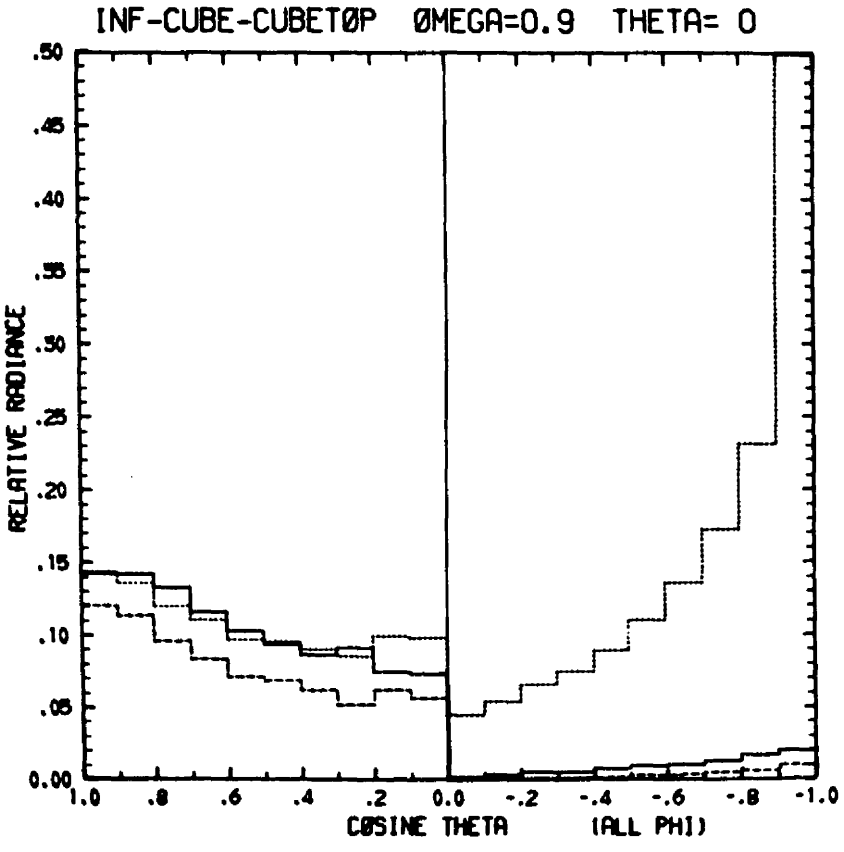

Figure A19. Same as Figure A1 except $\bar{\omega}_0$ = 0.9.

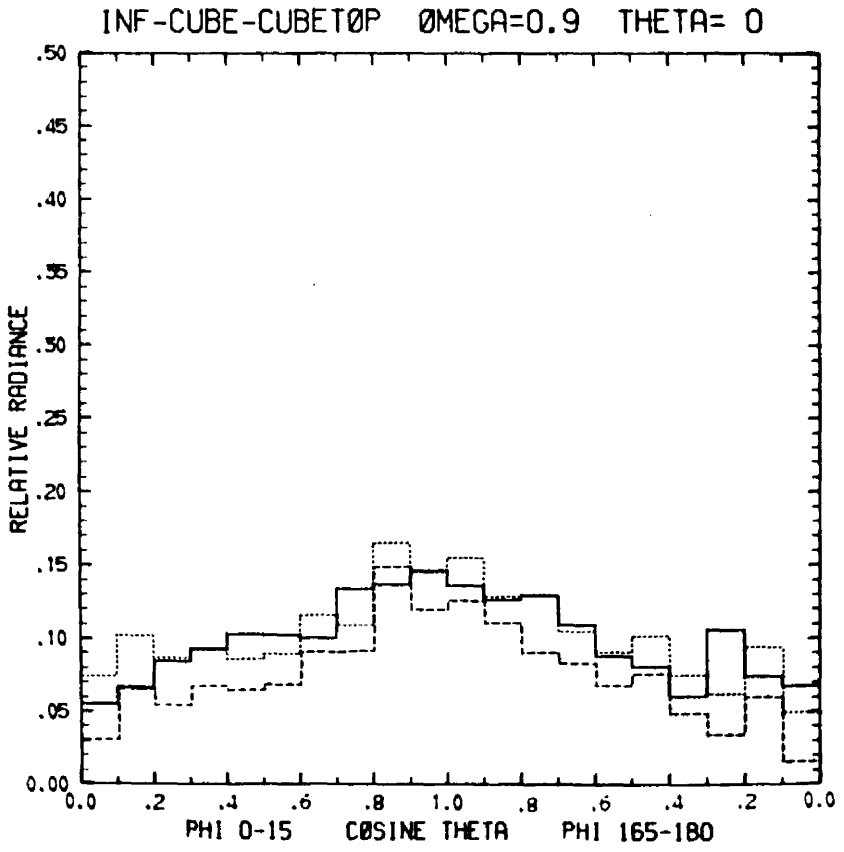

Figure A20. Same as Figure A2 except $\bar{\omega}_0$ = 0.9.

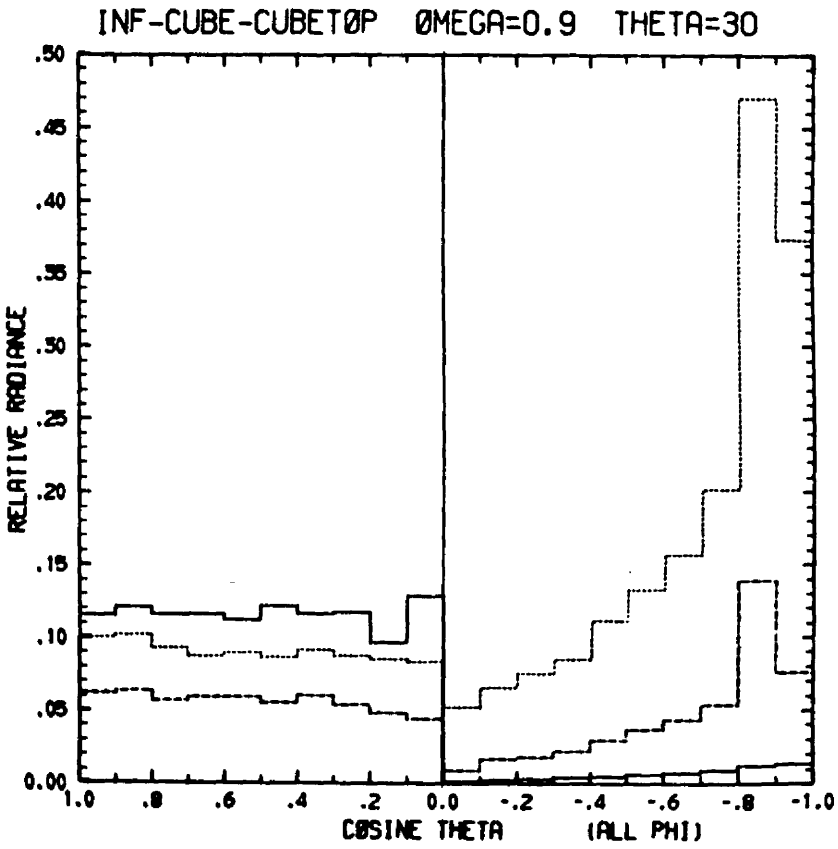

Figure A21. Same as Figure A1 except $\bar{\omega}_0 = 0.9$, $\theta_0 = 30^0$.

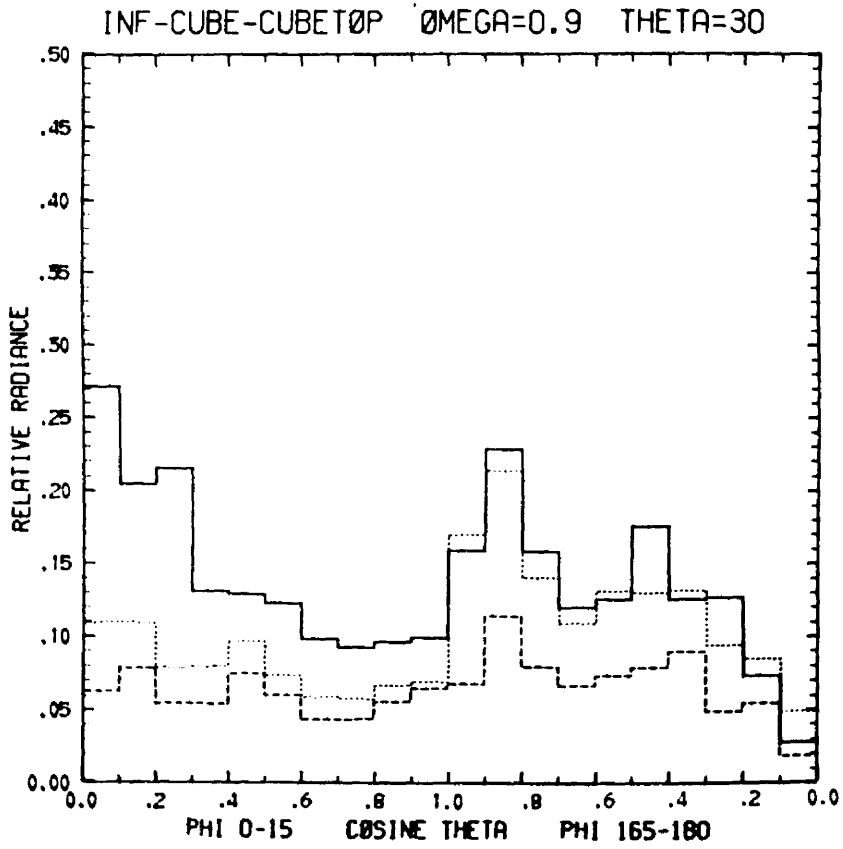

Figure A22. Same as Figure A2 except $\bar{\omega}_0 = 0.9$, $\theta_0 = 30^0$.

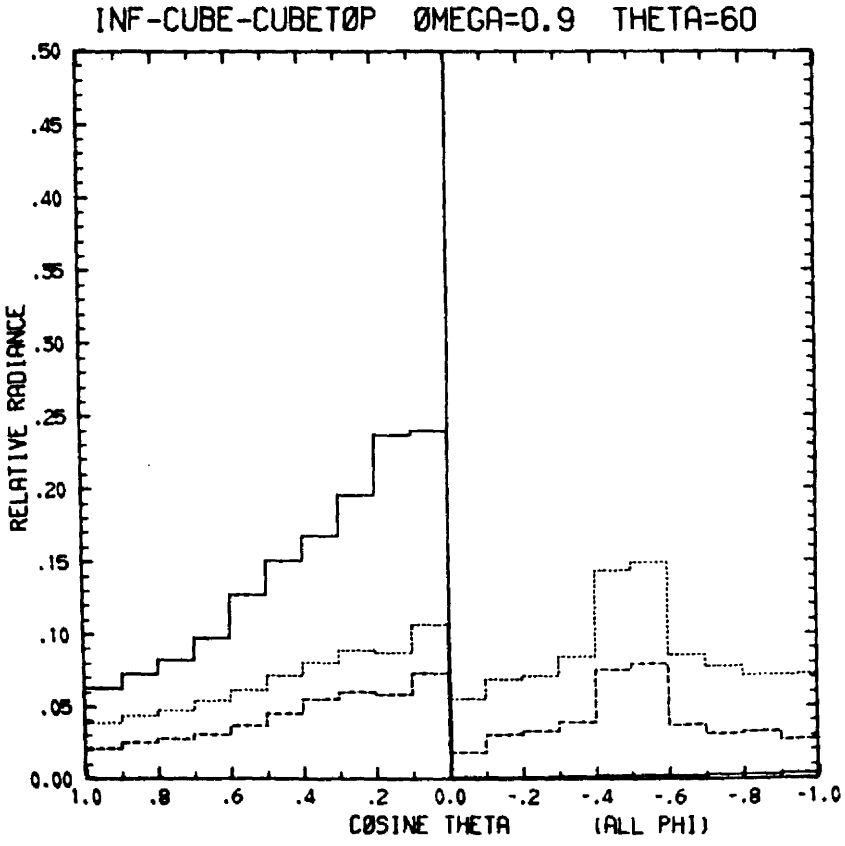

Figure A23. Same as Figure A1 except $\bar{\omega}_0 = 0.9$, $\theta_0 = 60^0$.

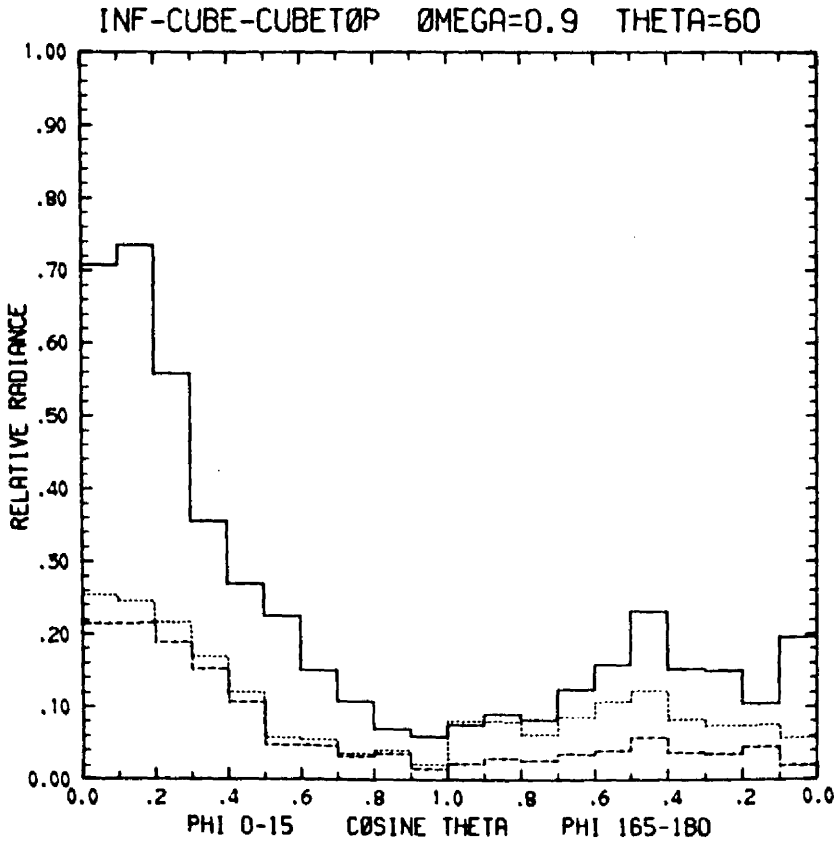

Figure A24. Same as Figure A2 except $\bar{\omega}_0 = 0.9$, $\theta_0 = 60^0$.

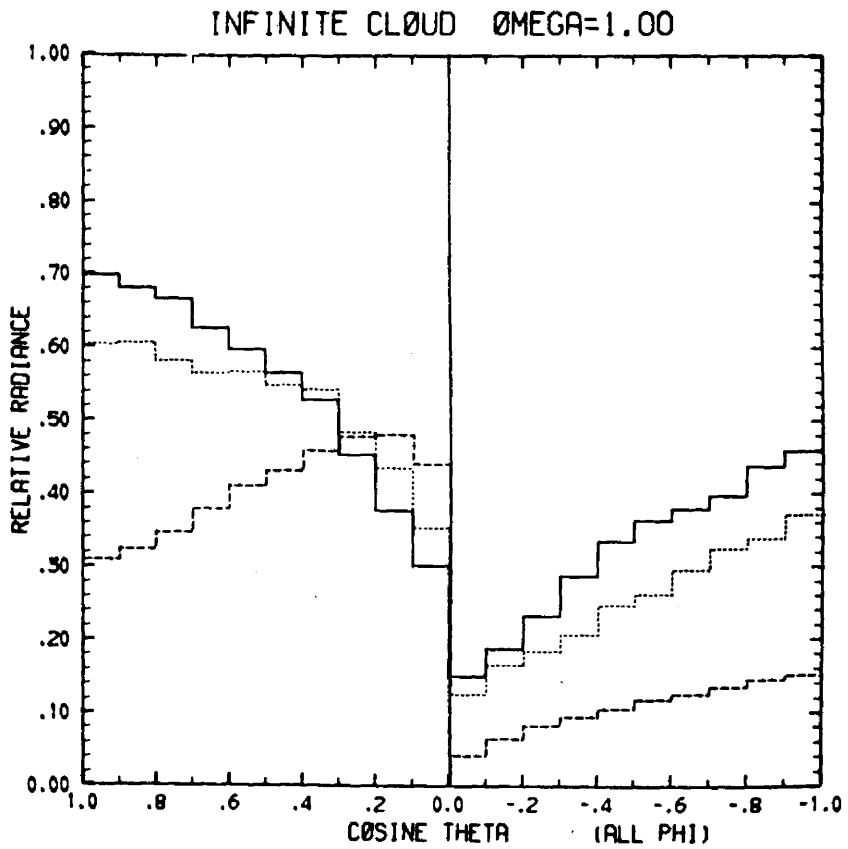

Figure A25. Upward and downward radiance (all ϕ) versus cosine θ for the infinite cloud, $\tau = 20$, $\bar{\omega}_0 = 1.0$ ($\theta_0 = 0^0$ ——, $\theta_0 = 30^0$ ...., $\theta_0 = 60^0$ ----).

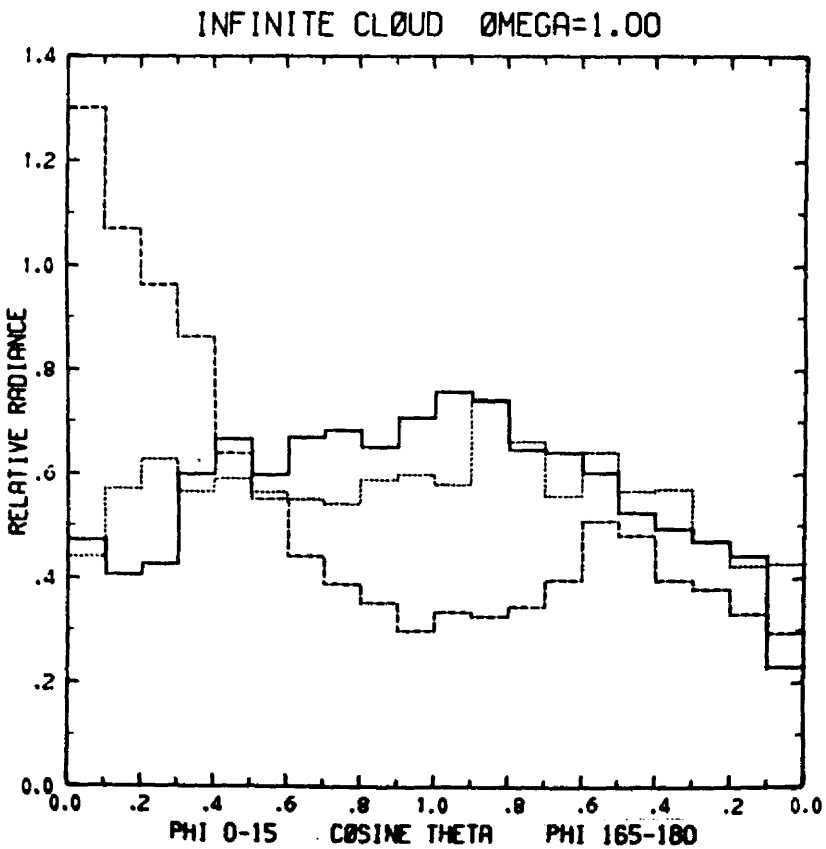

Figure A26. Upward radiance near the solar plane versus cosine θ for infinite cloud, $\tau = 20$, $\bar{\omega}_0 = 1.0$ ($\theta_0 = 0^0$ ——, $\theta_0 = 30^0$ ...., $\theta_0 = 60^0$ ----).

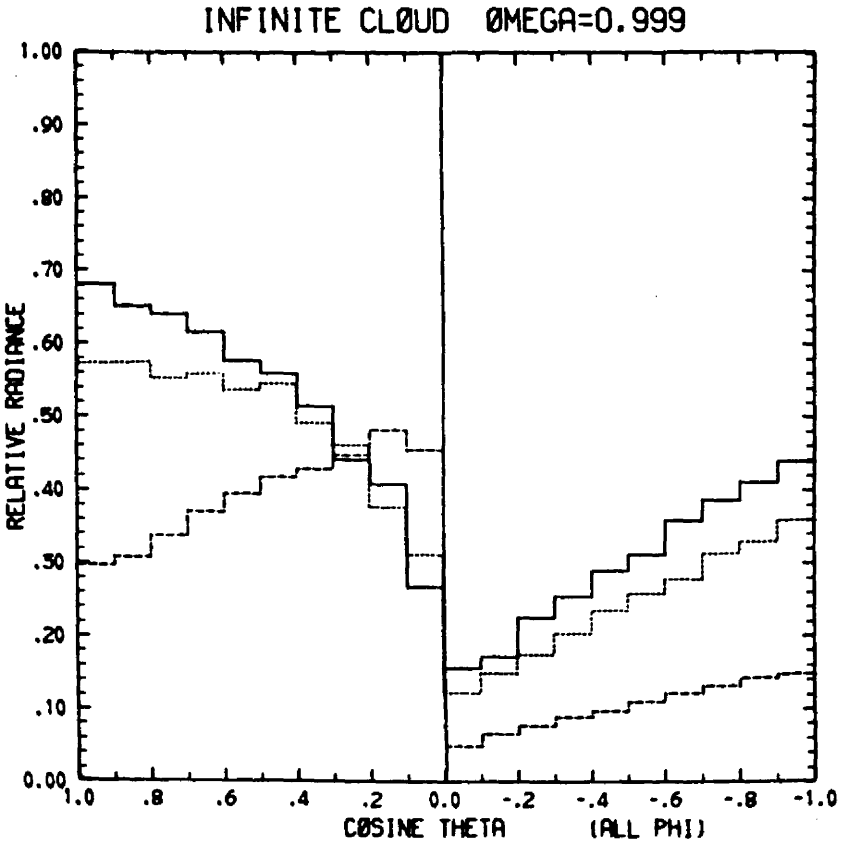

Figure A27. Same as Figure A25 except $\bar{\omega}_0$ = 0.999.

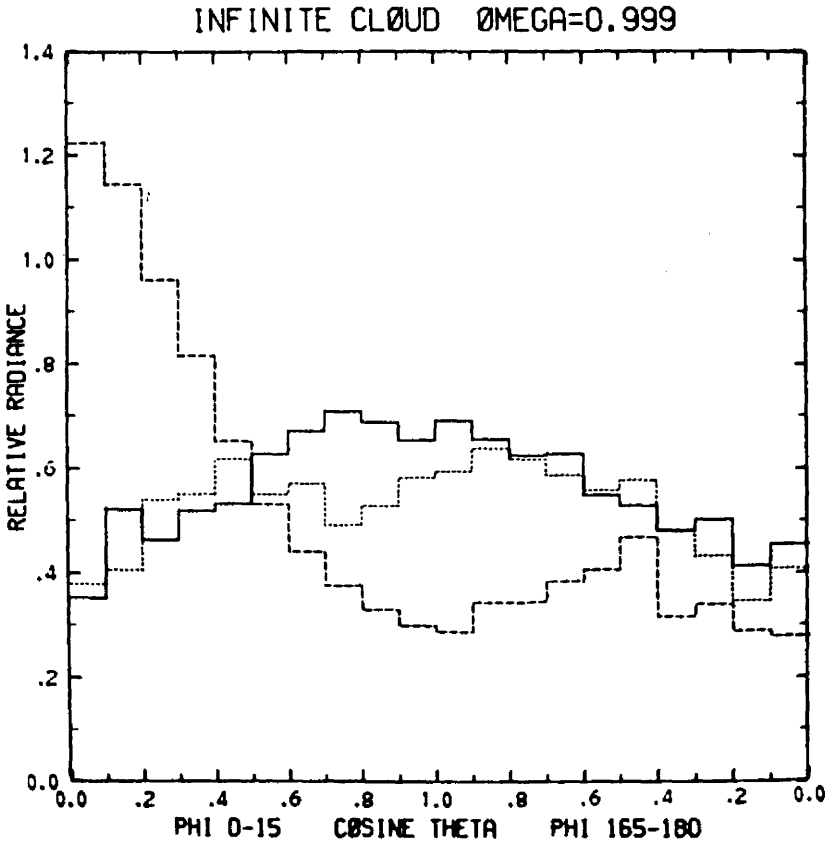

Figure A28. Same as Figure A26 except $\bar{\omega}_0$ = 0.999.

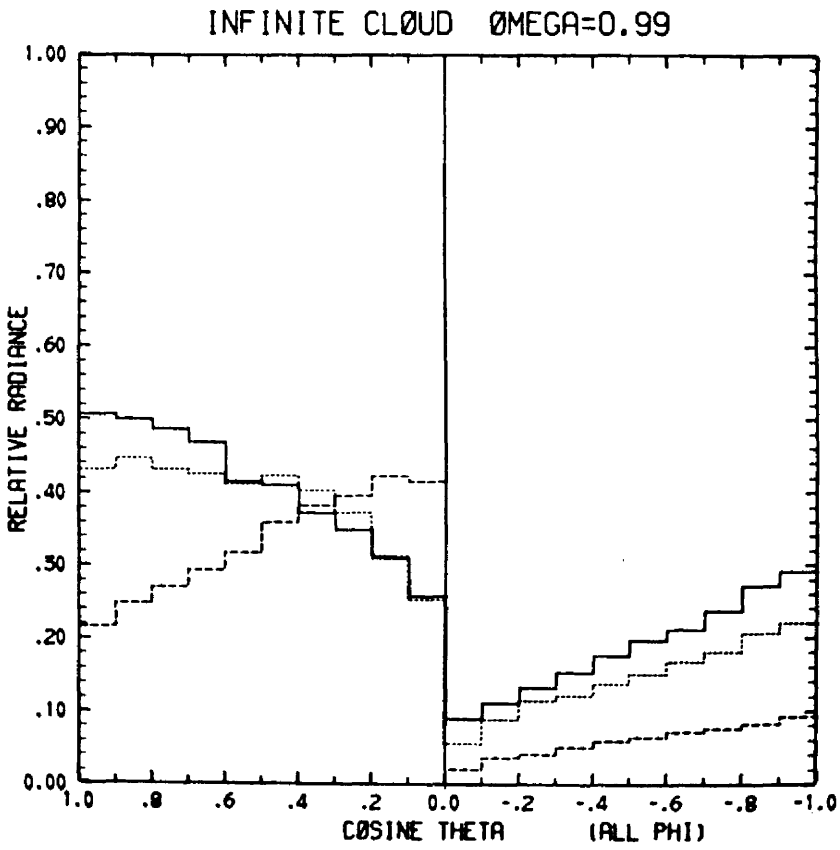

Figure A29. Same as Figure A25 except $\bar{\omega}_0$ = 0.99.

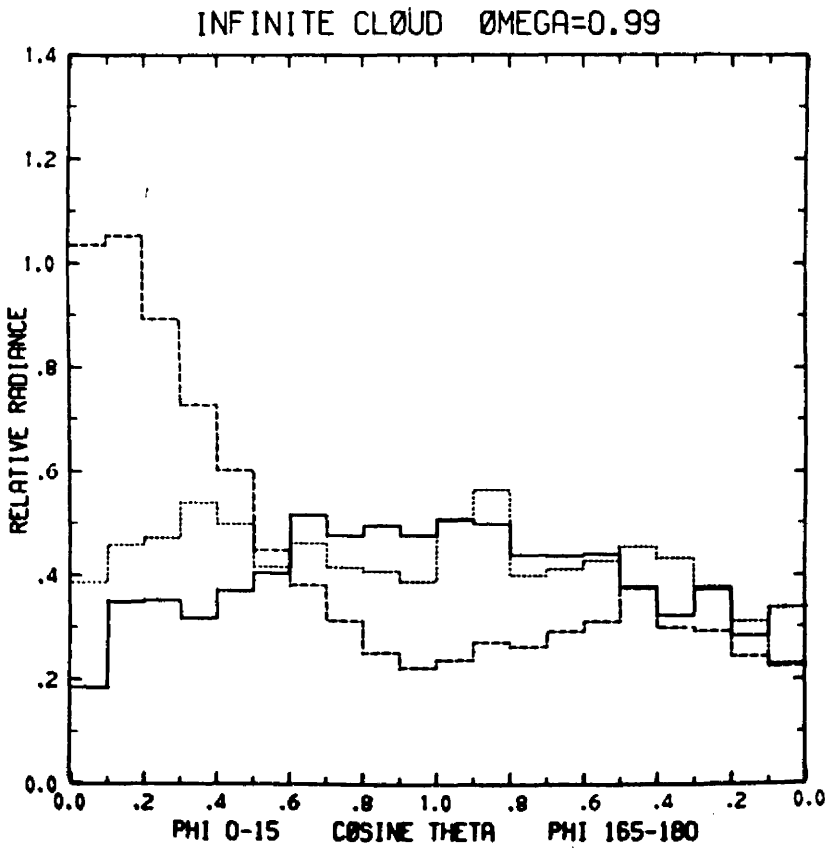

Figure A30. Same as Figure A26 except $\bar{\omega}_0$ = 0.99.

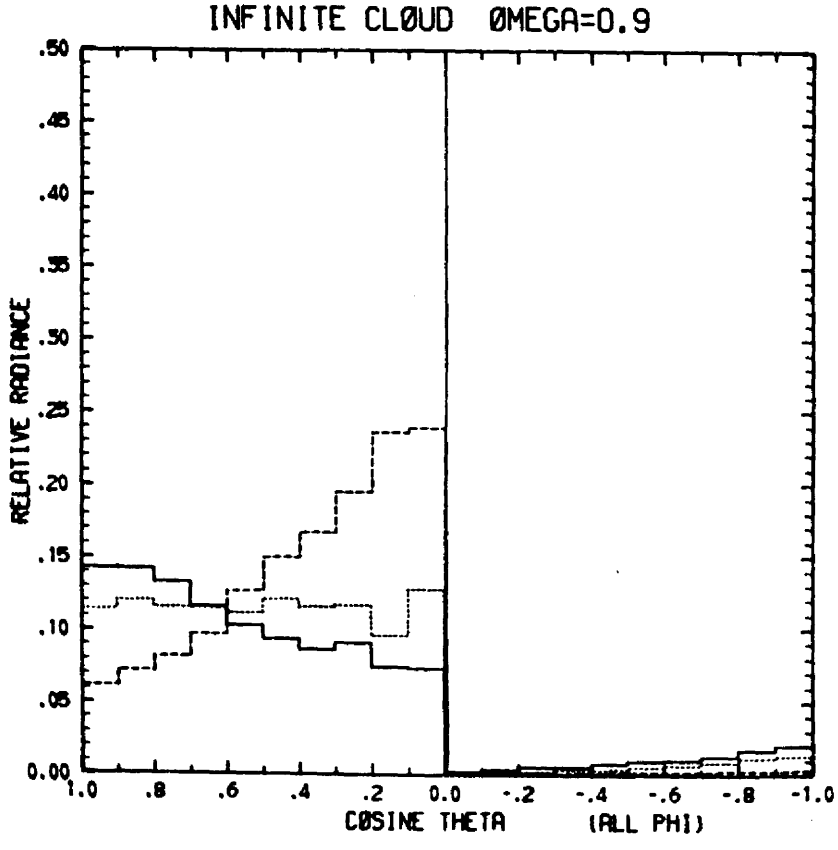

Figure A31. Same as Figure A25 except $\bar{\omega}_0$ = 0.9 (same as Figure 35).

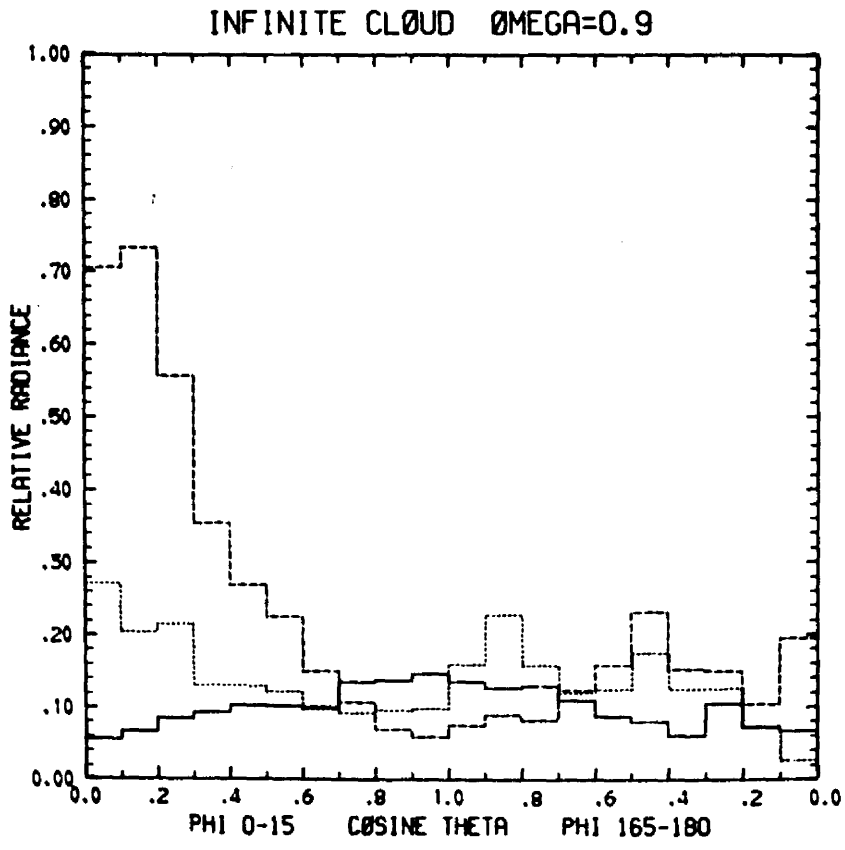

Figure A32. Same as Figure A26 except $\bar{\omega}_0$ = 0.9 (same as Figure 36).

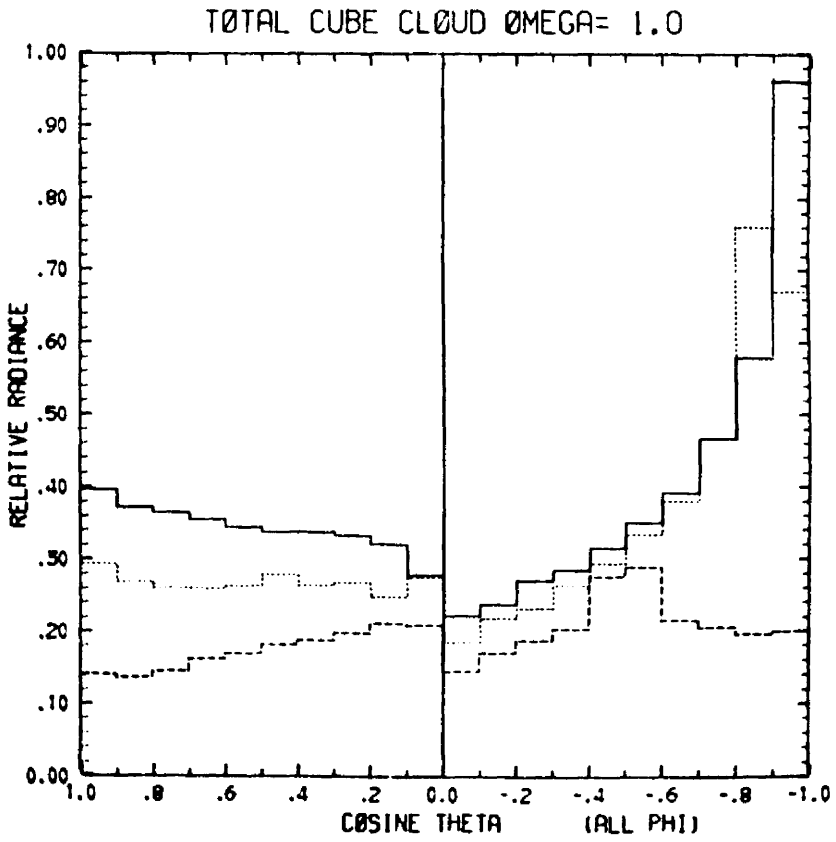

Figure A33. Same as Figure A25 except for finite cloud.

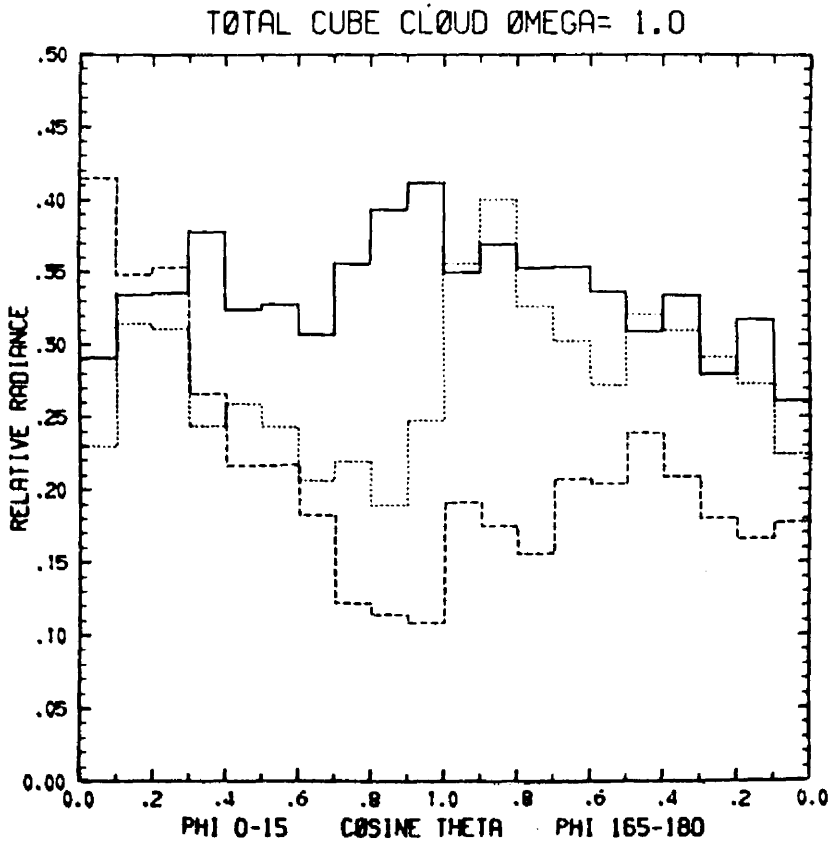

Figure A34. Same as Figure A26 except for finite cloud.

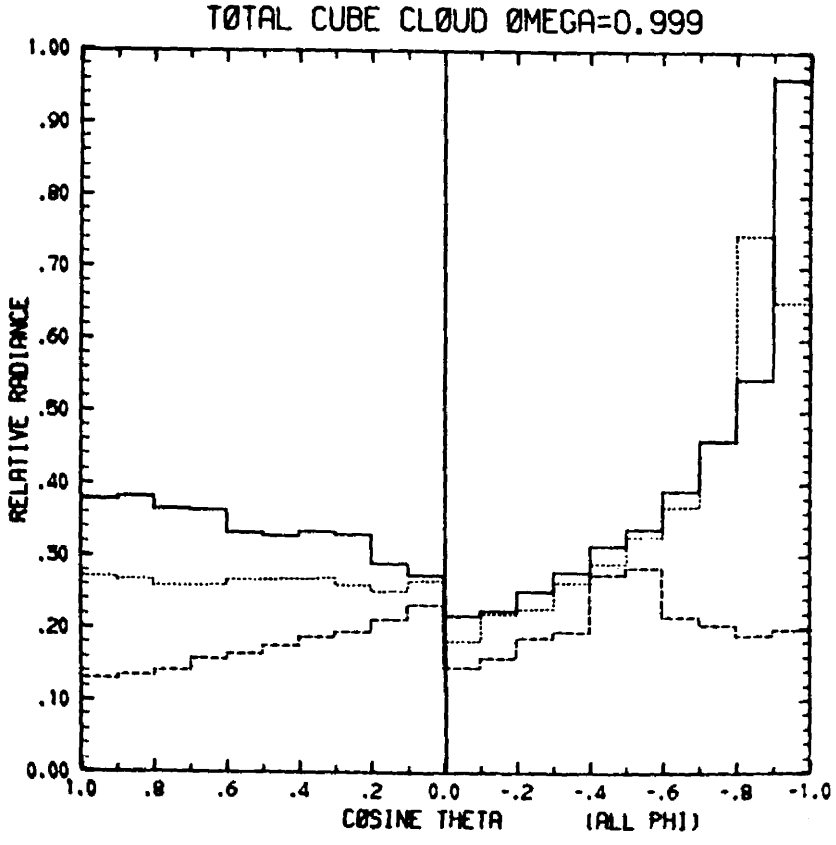

Figure A35. Same as Figure A25 except for finite cloud, $\bar{\omega}_0 = 0.999$.

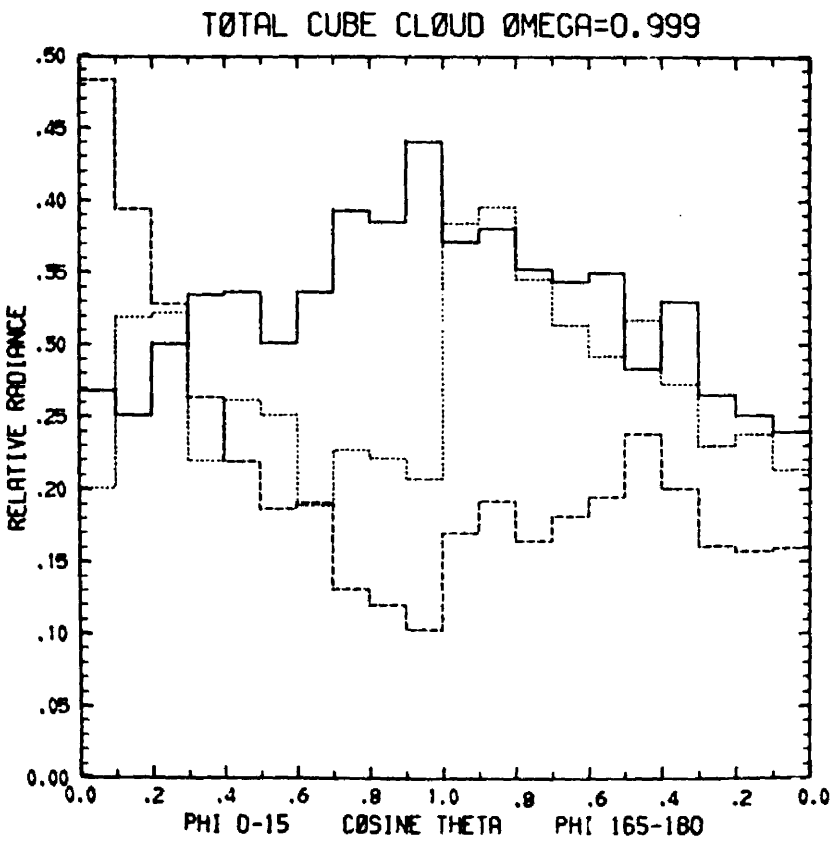

Figure A36. Same as Figure A26 except for finite cloud, $\bar{\omega}_0 = 0.999$.

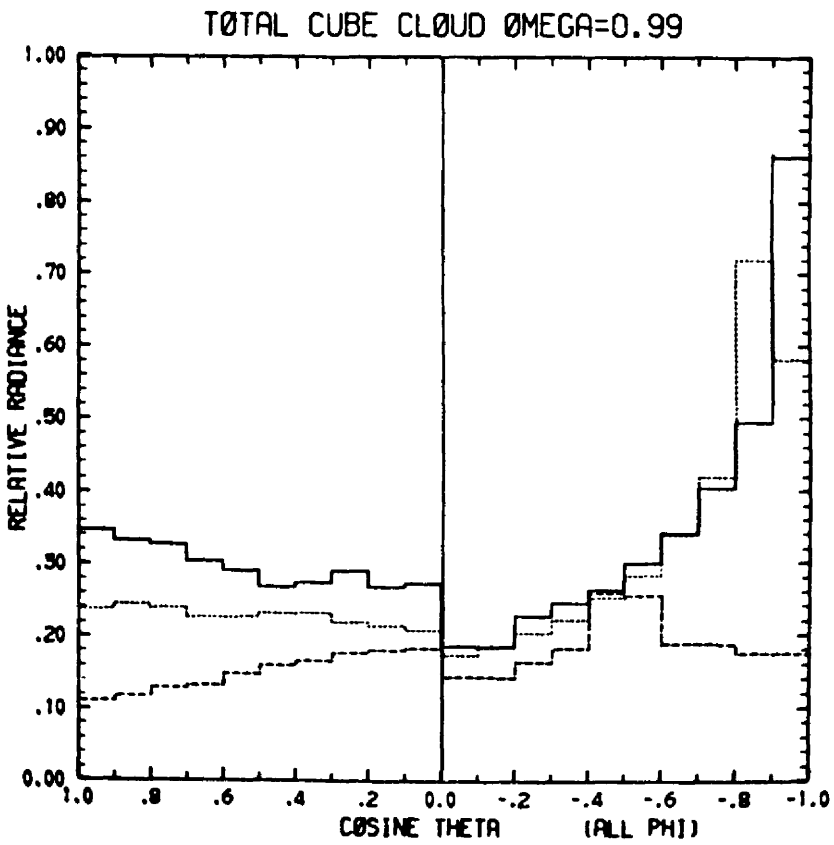

Figure A37. Same as Figure A25 except for finite cloud, $\bar{\omega}_0$ = 0.99.

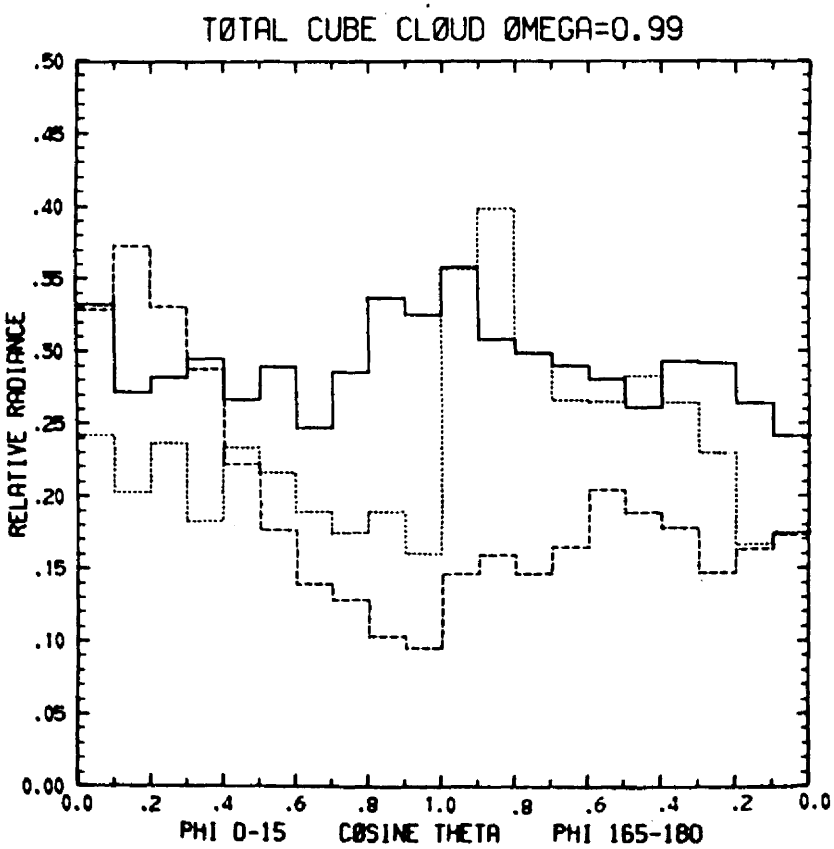

Figure A38. Same as Figure A26 except for finite cloud, $\bar{\omega}_0$ = 0.99.

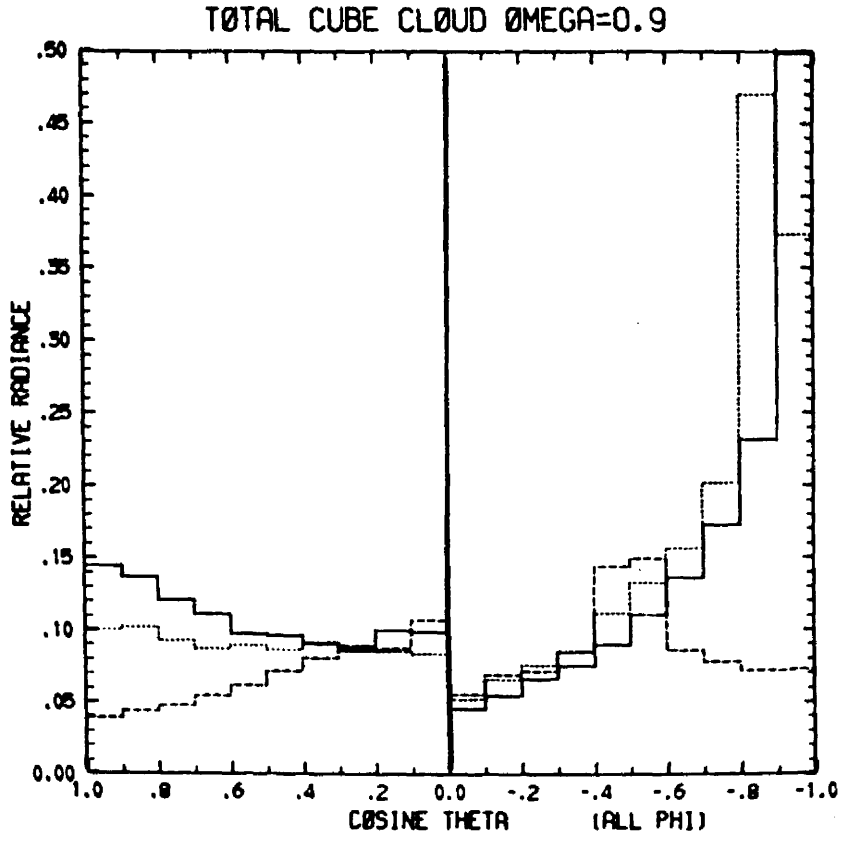

Figure A39. Same as Figure A25 except for finite cloud, $\bar{\omega}_0$ = 0.9 (same as Figure 37).

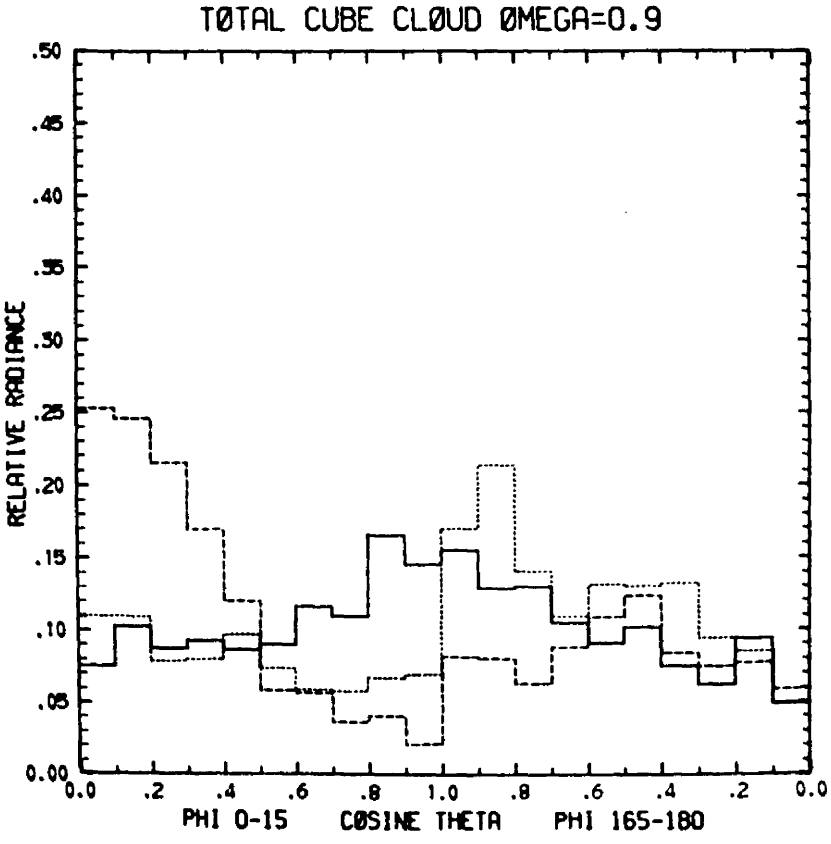

Figure A40. Same as Figure A26 except for finite cloud, $\bar{\omega}_0$ = 0.9 (same as Figure 38).

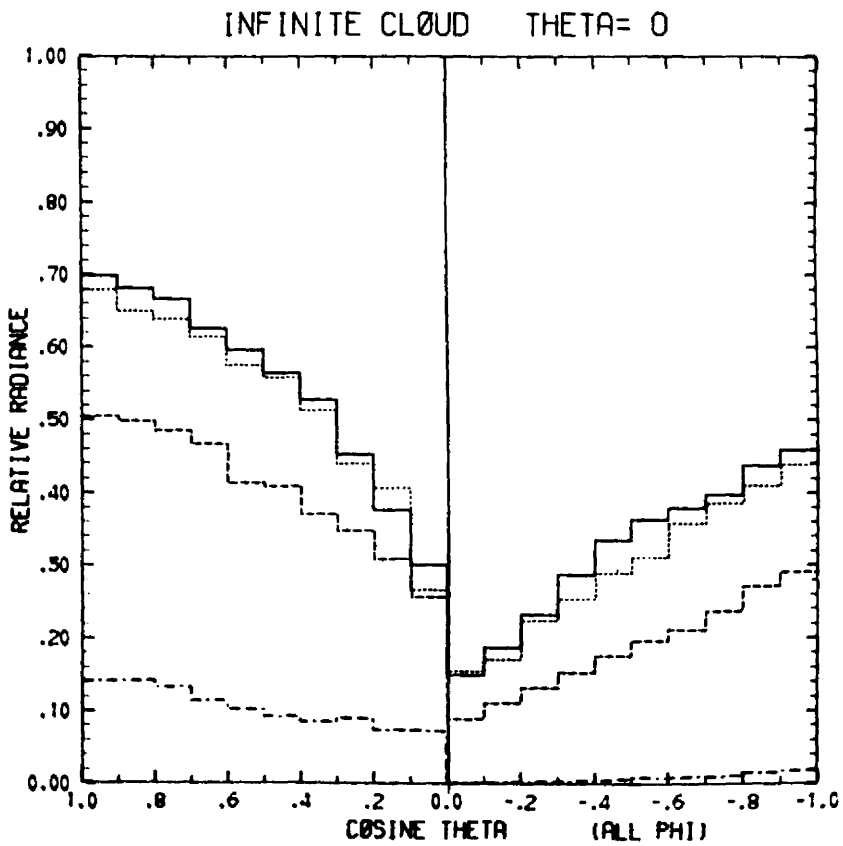

Figure A41. Upward and downward radiance (all ϕ) versus cosine θ for the infinite cloud, $\theta_0 = 0^0$, $\tau = 20$, ($\bar{\omega}_0 = 1.0$ ——, $\bar{\omega}_0 = 0.999$ ...., $\bar{\omega}_0 = 0.99$ ----, $\bar{\omega}_0 = 0.9$ -.-.-.) (same as Figure 31).

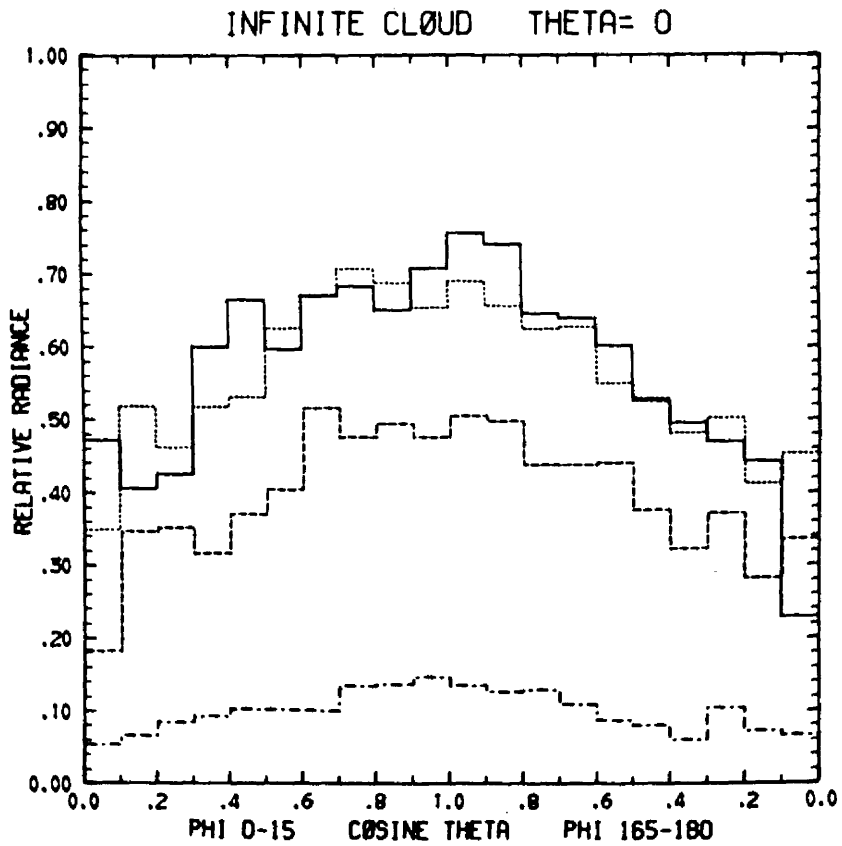

Figure A42. Upward relative radiance near the solar plane versus cosine θ for the infinite cloud, $\theta_0 = 0^0$, $\tau = 20$, ($\bar{\omega}_0 = 1.0$ ——, $\bar{\omega}_0 = 0.999$ ...., $\bar{\omega}_0 = 0.99$ ----. $\bar{\omega}_0 = 0.9$ -. -.-.) (same as Figure 32).

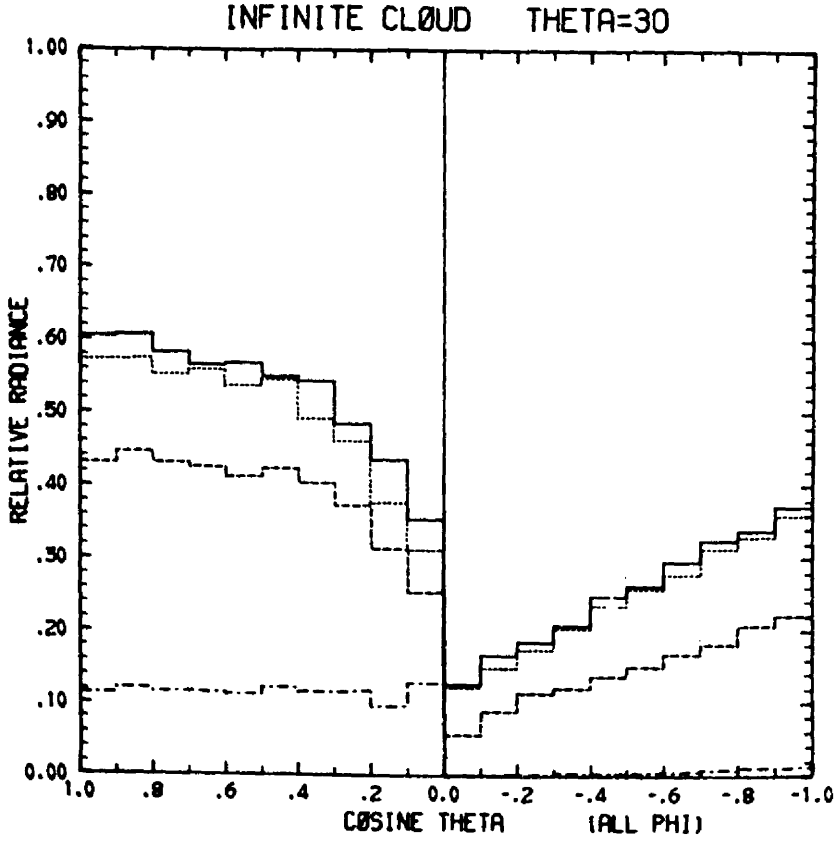

Figure A43. Same as Figure A41 except $\theta_0 = 30^0$.

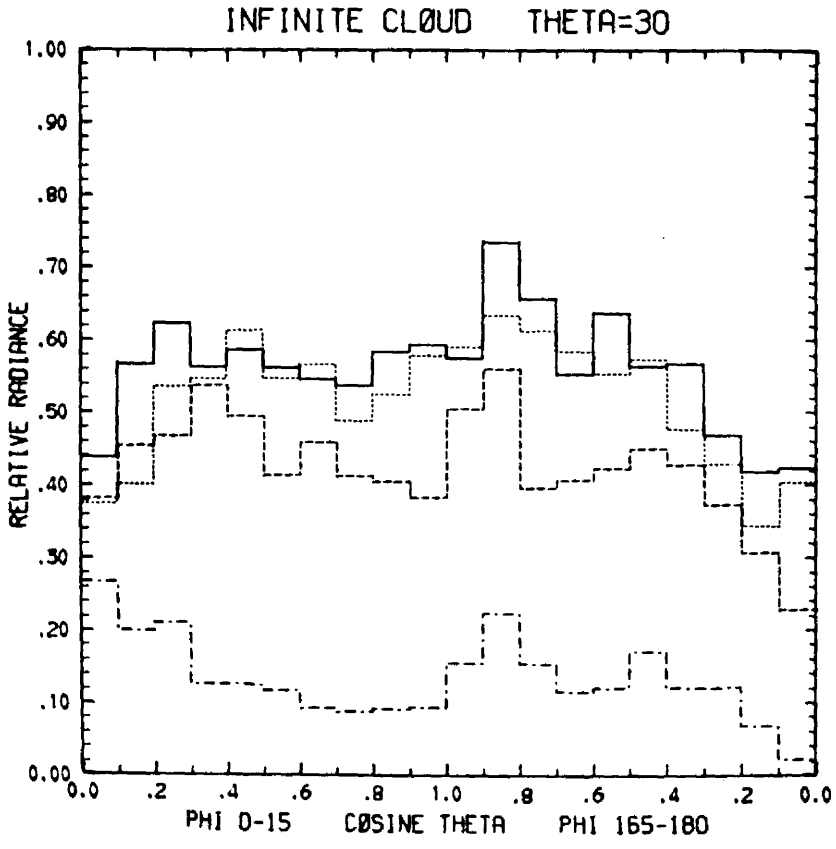

Figure A44. Same as Figure A42 except $\theta_0 = 30^0$.

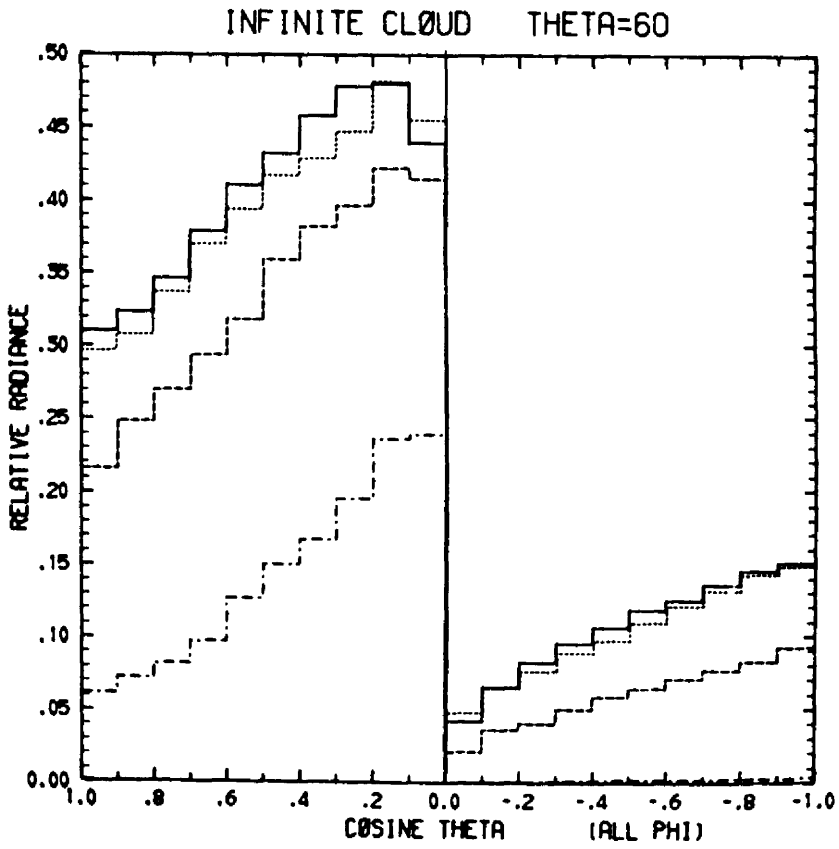

Figure A45. Same as Figure A41 except $\theta_o = 60^o$.

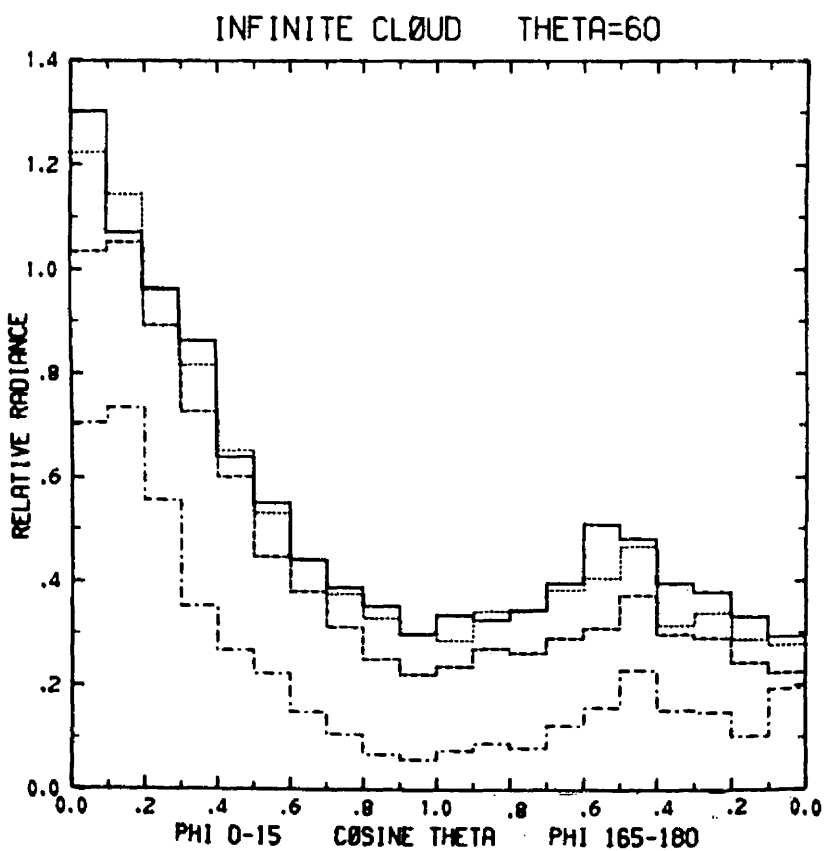

Figure A46. Same as Figure A42 except $\theta_o = 60^o$.

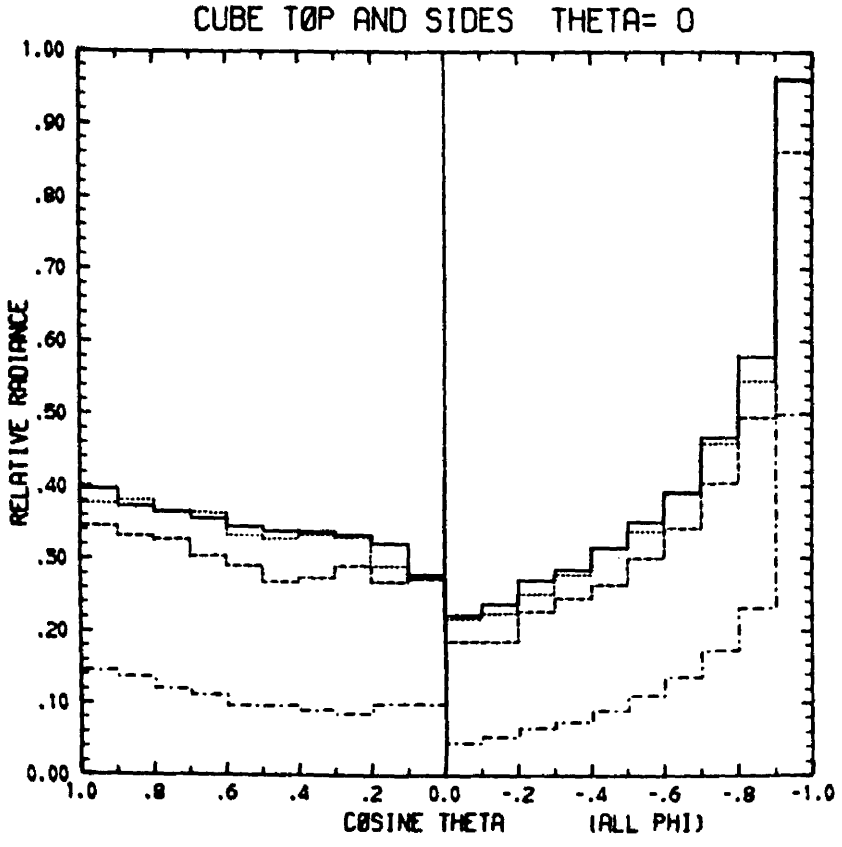

Figure A47. Same as Figure A41 except for finite cloud, (same as Figure 33).

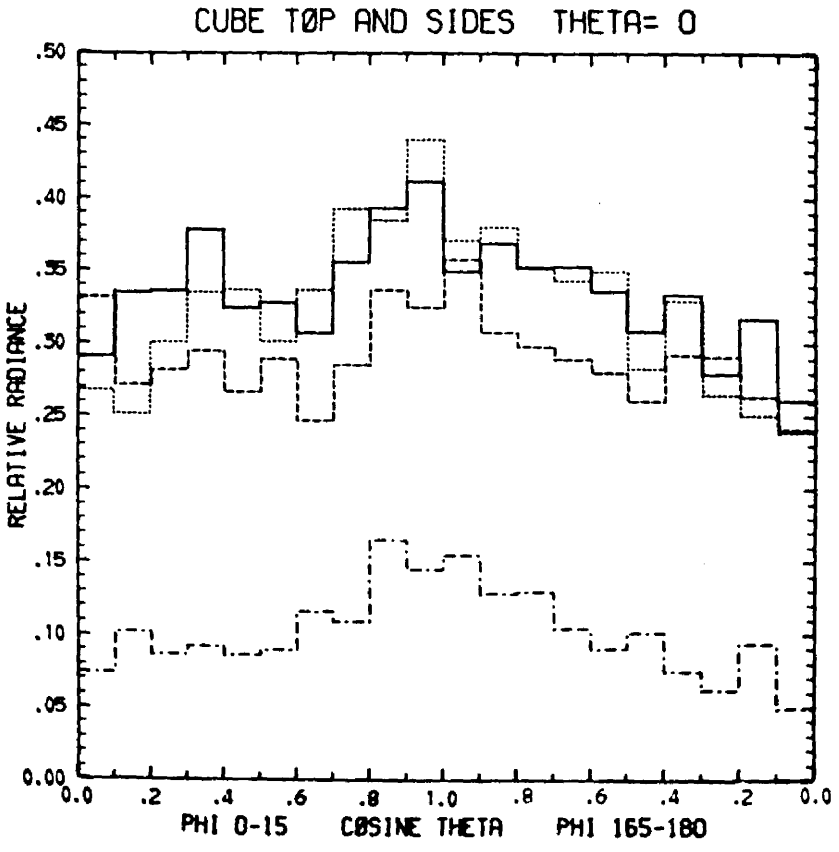

Figure A48. Same as Figure A42 except for finite cloud, (same as Figure 34).

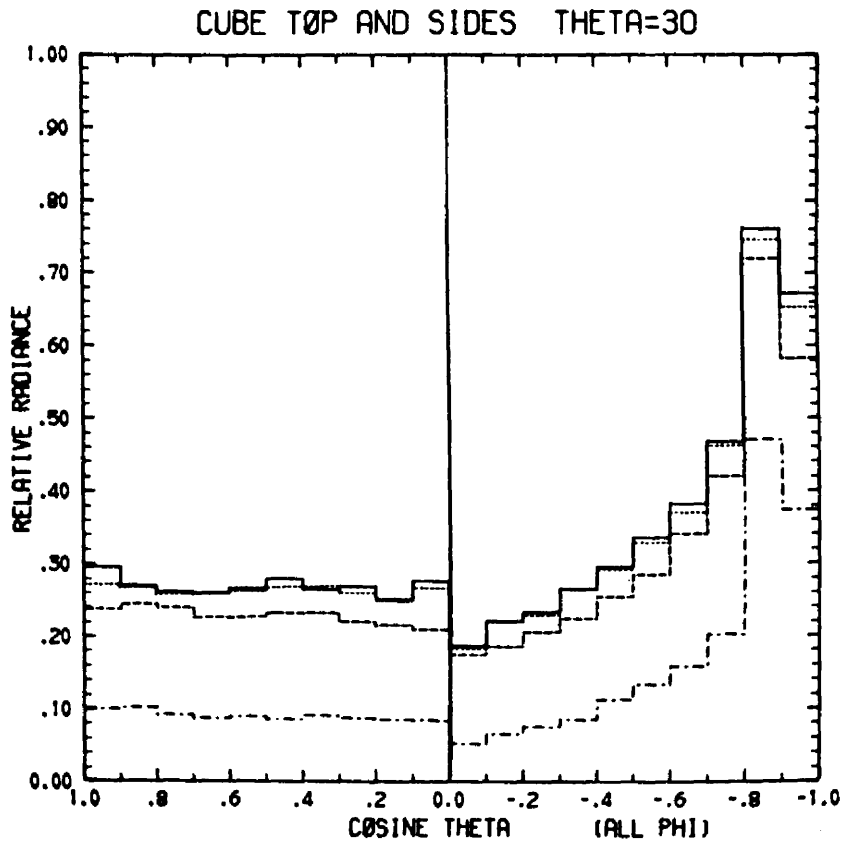

Figure A49. Same as Figure A41 except for finite cloud $\theta_o = 30^o$.

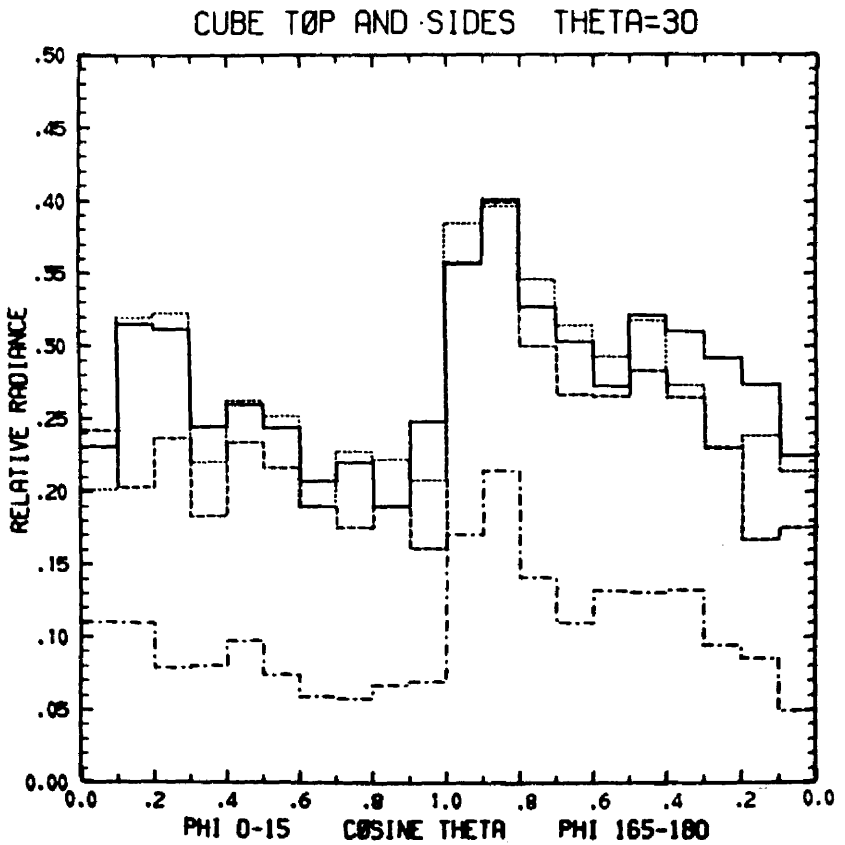

Figure A50. Same as Figure A42 except for finite cloud $\theta_o = 30^o$.

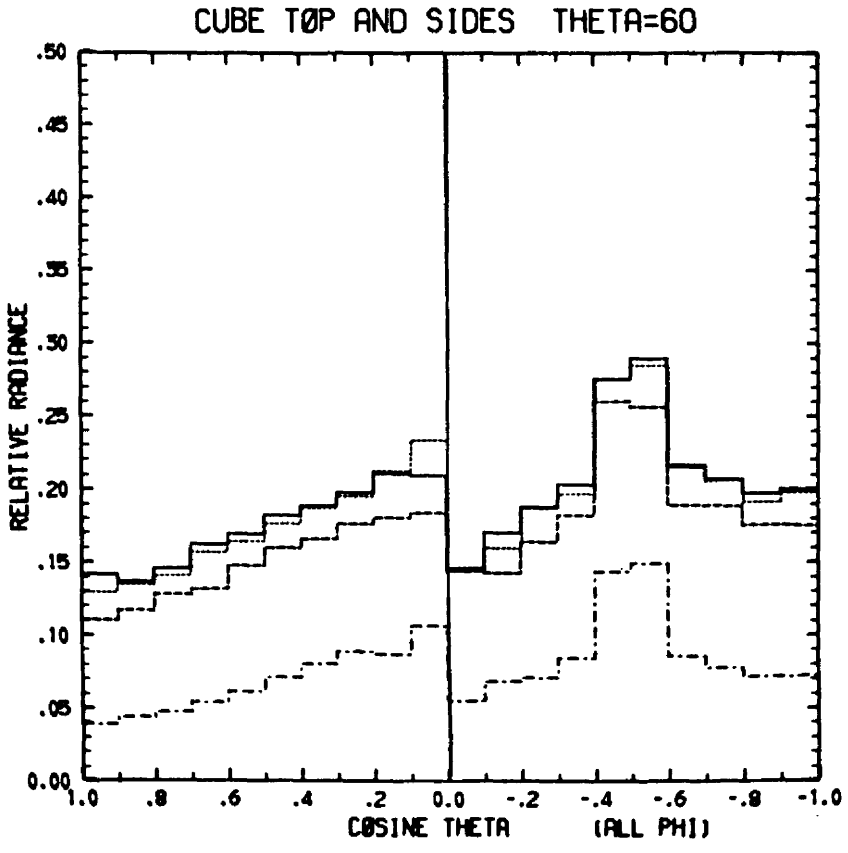

Figure A51. Same as Figure A41 except for finite cloud $\theta_o = 60^o$.

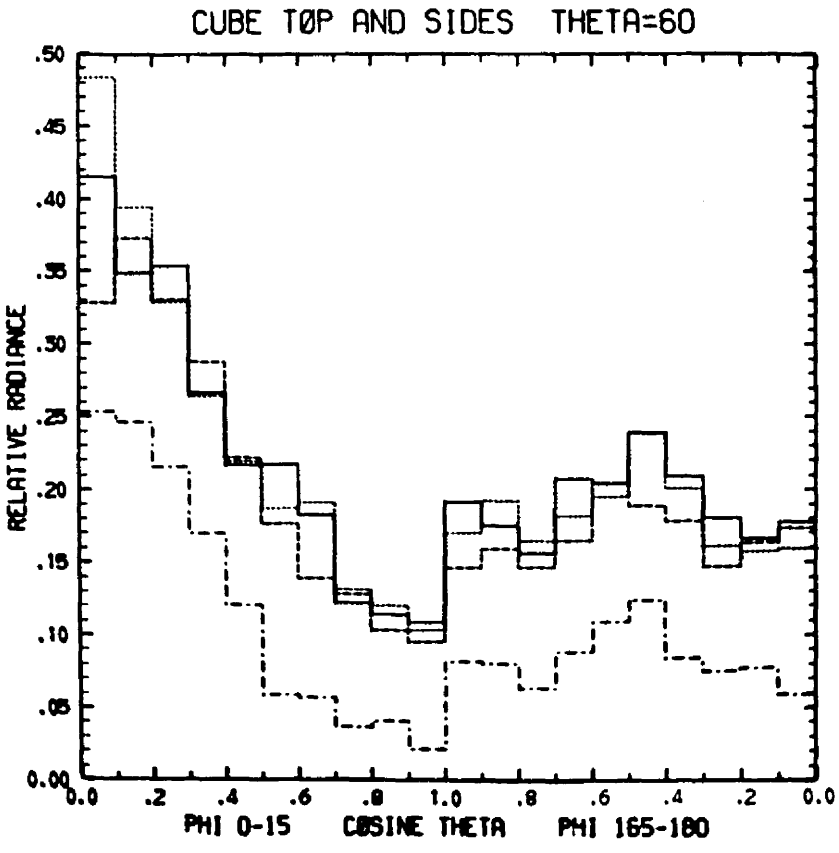

Figure A52. Same as Figure A42 except for finite cloud $\theta_o = 60^o$.

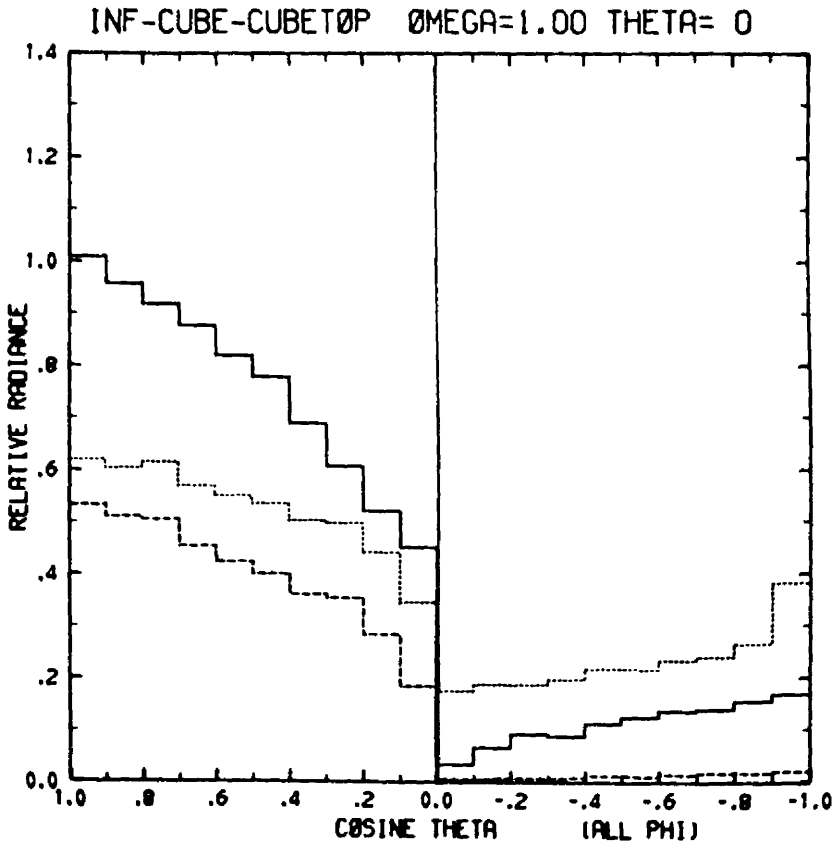

Figure A53. Same as Figure A1 but for τ = 60 (same as Figure 34).

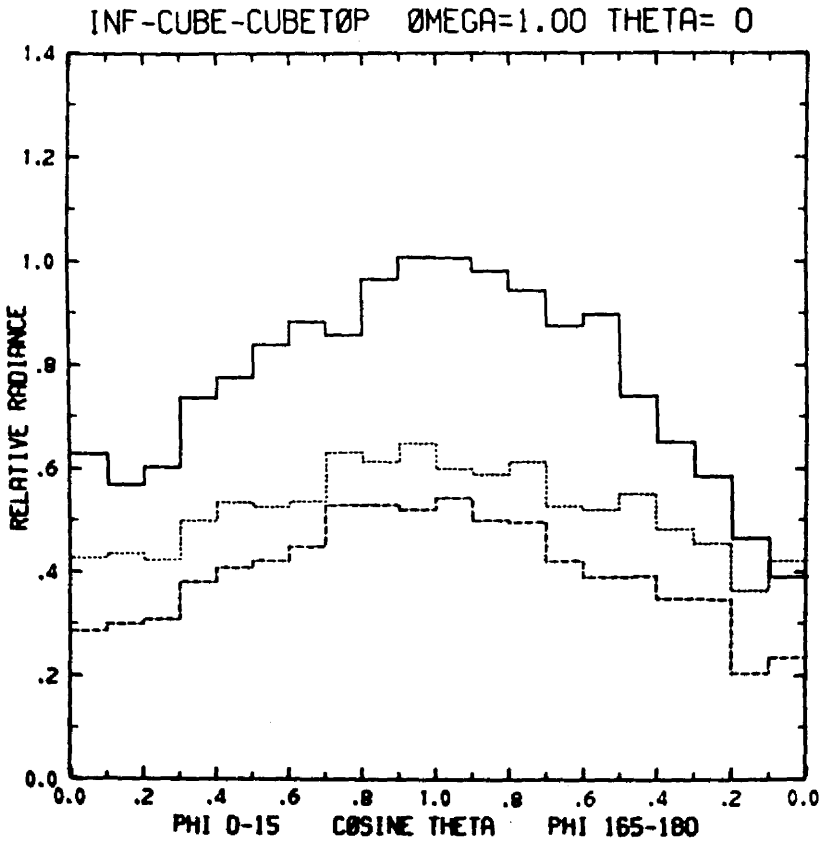

Figure A54. Same as Figure A2 but for τ = 60 (same as Figure 40).

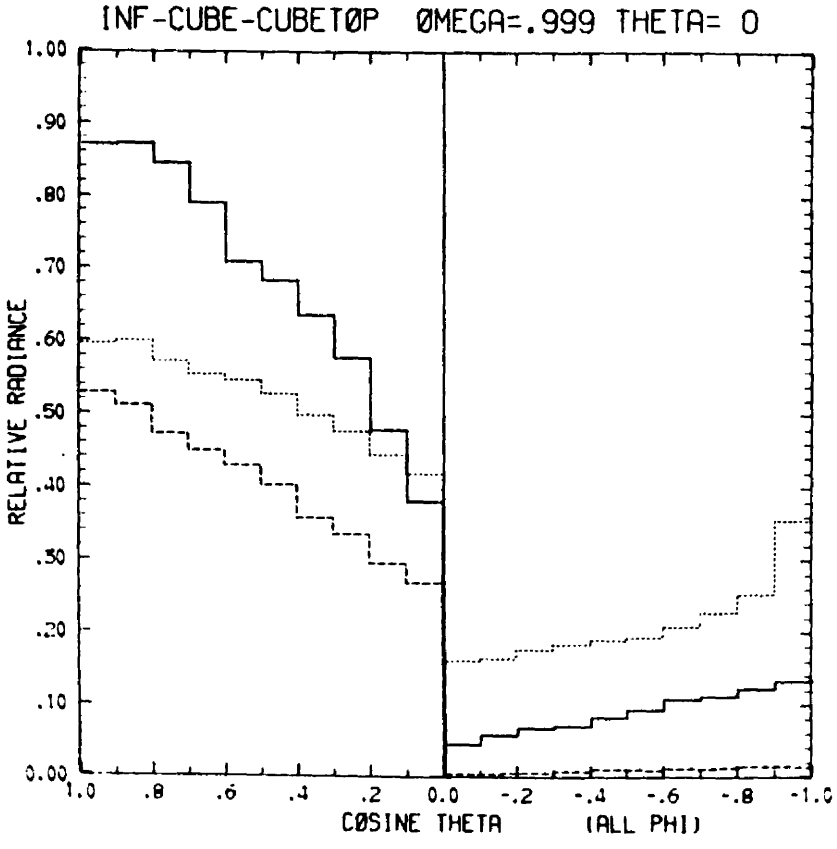

Figure A55. Same as Figure A1 but for $\bar{\omega}_0$ = 0.999, τ = 60 (same as Figure 41).

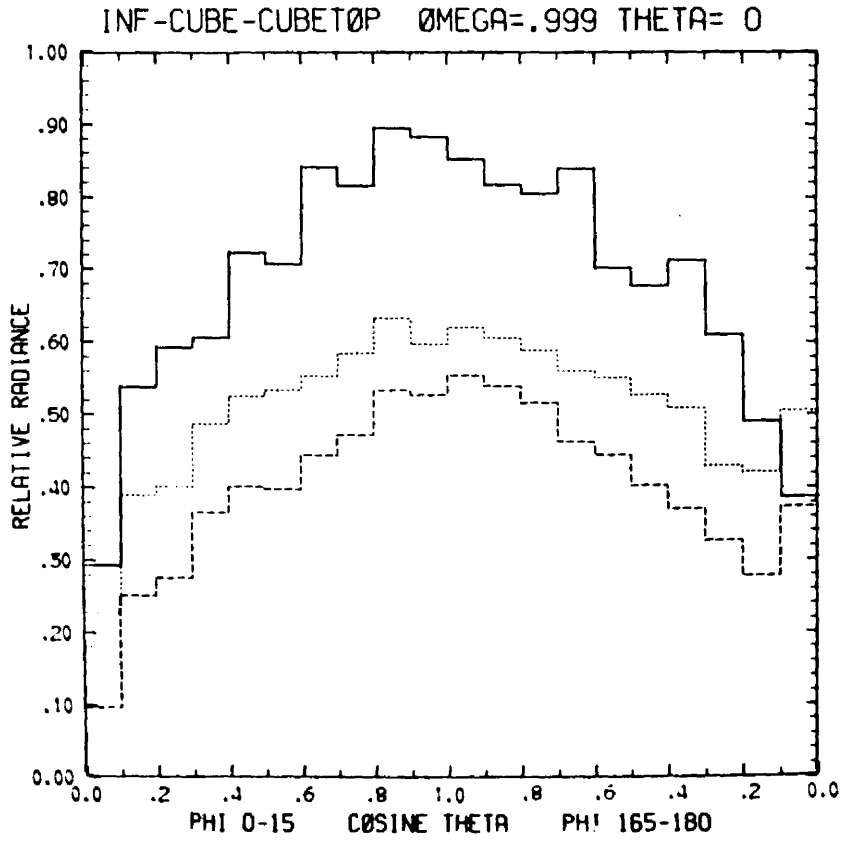

Figure A56. Same as Figure A2 but for $\bar{\omega}_0$ = 0.999, τ = 60 (same as Figure 42).

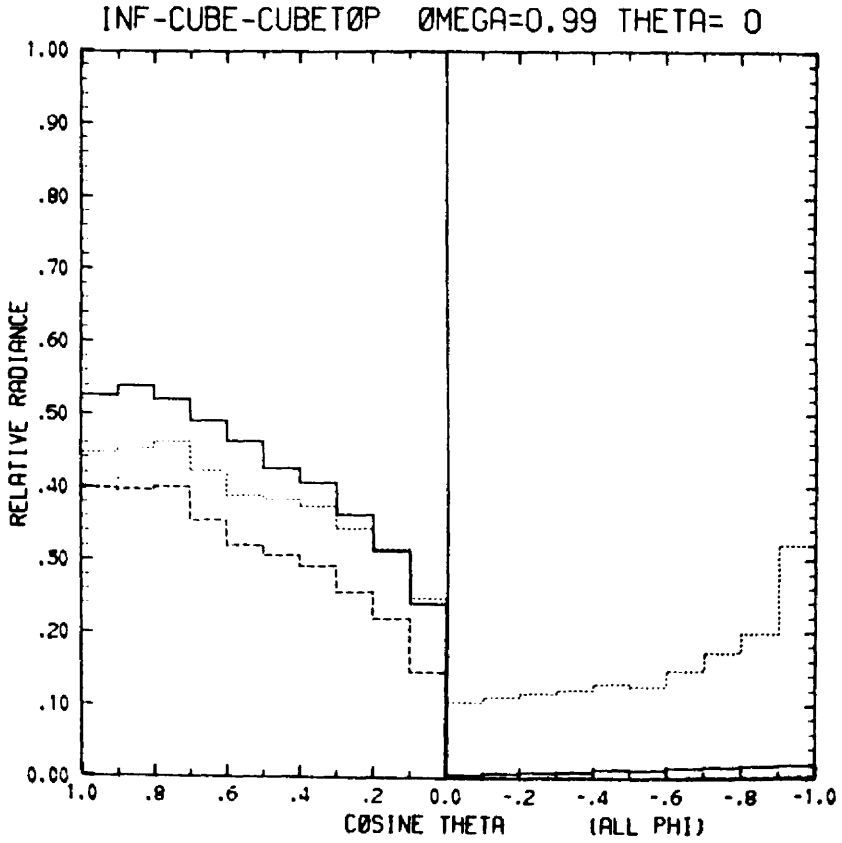

Figure A57. Same as Figure A1 but for $\bar{\omega}_0$ = 0.99, τ = 60 (same as Figure 43).

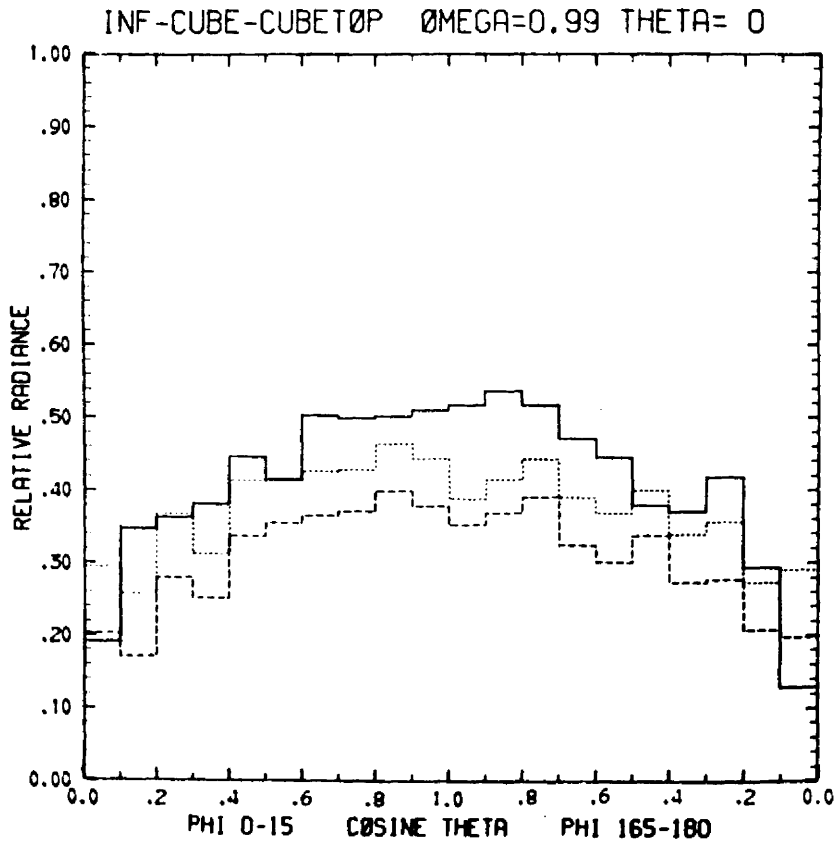

Figure A58. Same as Figure A2 but for $\bar{\omega}_0$ = 0.99, τ = 60 (same as Figure 44).

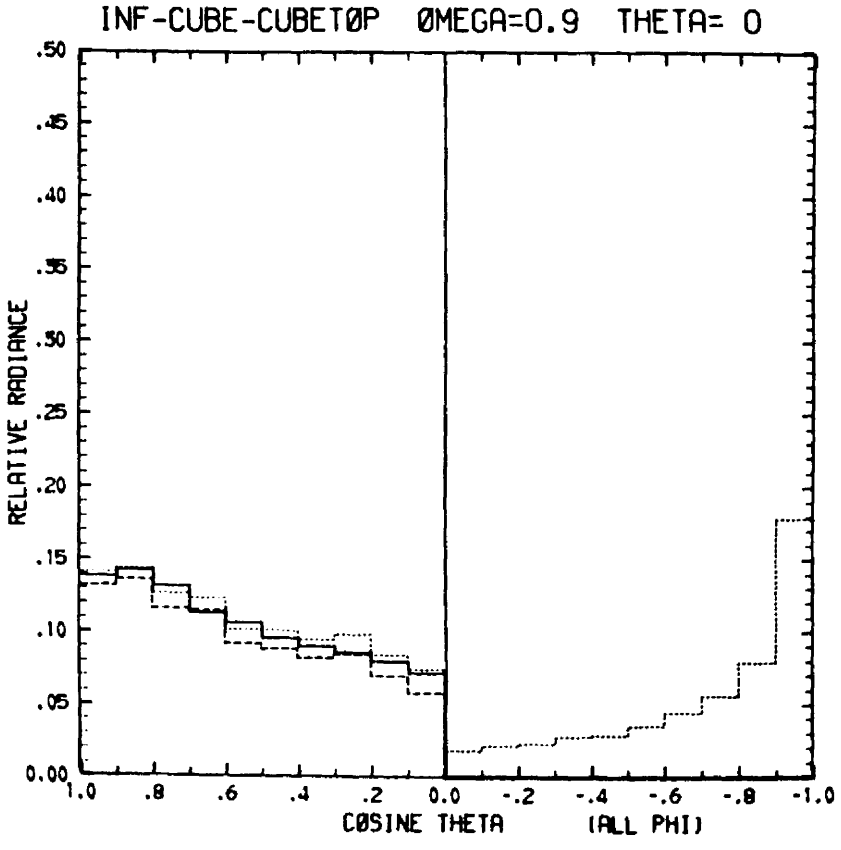

Figure A59. Same as Figure A1 but for $\bar{\omega}_0$ = 0.9, τ = 60 (same as Figure 45).

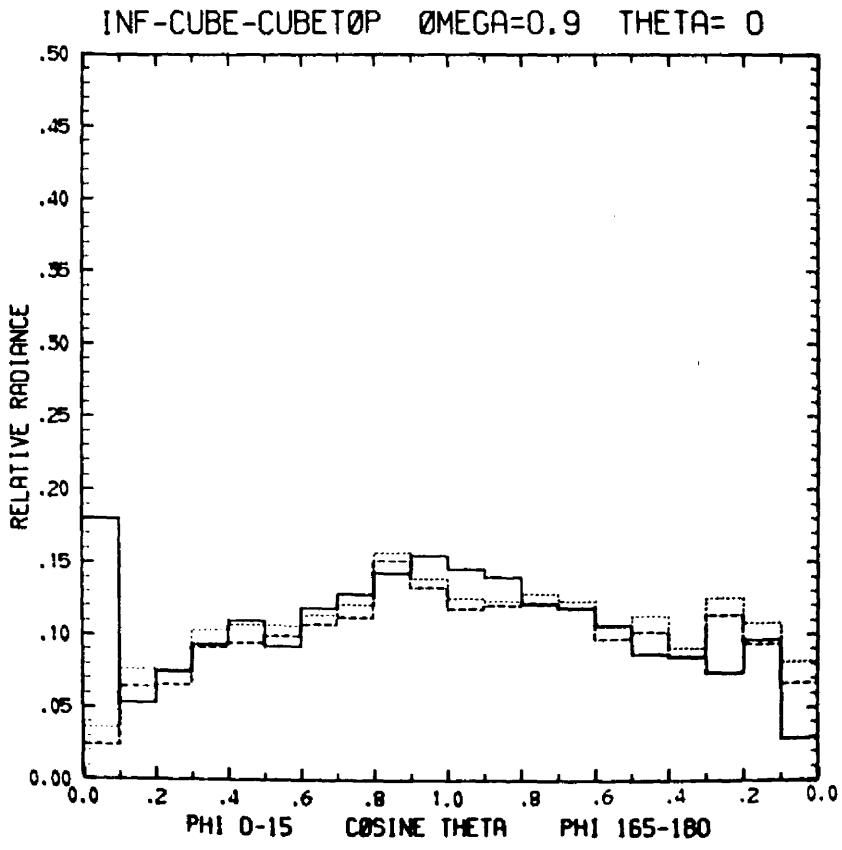

Figure A60. Same as Figure A2 but for $\bar{\omega}_0$ = 0.9, τ = 60 (same as Figure 46).

BIBLIOGRAPHIC DATA SHEET	1. Report No. ATS Paper No. 285	2.	3. Recipient's Accession No.

4. Title and Subtitle

Simulated Radiance Patterns for Mie Absorbing Finite Clouds

5. Report Date: March 1978

6.

7. Author(s): John T. Klehr and Thomas B. McKee

8. Performing Organization Rept. No. 285

9. Performing Organization Name and Address

Dept. of Atmospheric Science
Colorado State University
Fort Collins, CO 80523

10. Project/Task/Work Unit No.

11. Contract/Grant No. ATM 76-80568

12. Sponsoring Organization Name and Address

National Science Foundation

13. Type of Report & Period Covered

14.

15. Supplementary Notes

16. Abstracts

Results of Mie absorption upon shortwave irradiance values and radiance patterns of finite (cubic) and infinite (layer) clouds are presented over a range of single scattering albedoes ($\bar{\omega}_0$) and solar zenith angles. A finite cloud is shown to absorb a smaller fraction of incident light than an infinite cloud at all sun angles and values of single scattering albedo. As the solar zenith angle is increased the absorption in an infinite cloud decreases in the lower layers of the cloud, while in the finite cloud the lower layers increase in absorption.

Radiance patterns are shown to be primarily determined by cloud and solar geometries with absorption tending to reduce the radiance values and only slightly flatten the radiance patterns. If the optical depth is increased from 20 to 60 with the sun vertical the finite cloud shows a larger increase in fractional absorption than the infinite, but even at large optical depths (60) and large absorption values ($\bar{\omega}_0 = 0.9$) the finite cloud still allows a significant fraction of light to escape downward from its sides.

17. Key Words and Document Analysis. 17a. Descriptors

Finite cloud
Radiative transfer
Mie shortwave absorption
Directional reflectance
Radiance patterns

17b. Identifiers/Open-Ended Terms

17c. COSATI Field/Group

18. Availability Statement	19. Security Class (This Report) UNCLASSIFIED	21. No. of Pages 104
	20. Security Class (This Page) UNCLASSIFIED	22. Price